國 立 交 通 大 學
電 信 工 程 學 系

博 士 論 文

合成波導之設計與應用

Design and Applications of Synthetic Waveguides

研 究 生 ：吳憲順 (Hsien-Shun Wu)
指導教授：莊晴光 博士 (Dr. Ching-Kuang C. Tzuang)

中 華 民 國 九 十 四 年 七 月

合成波導之設計與應用

Design and Applications of Synthetic Waveguides

研 究 生：吳憲順　　Student: Hsien-Shun Wu

指導教授: 莊晴光 博士　　Advisor: Dr. Ching-Kuang C. Tzuang

國 立 交 通 大 學

電 信 工 程 研 究 所

博 士 論 文

A Dissertation

Submitted to Institute of Communication Engineering

College of Engineering

National Chiao Tung University

In Partial Fulfillment of the Requirements

for the Degree of

Doctor of Philosophy

in

Communication Engineering

July 2005

Hsinchu, Taiwan, Republic of China

中 華 民 國 九 十 四 年 七 月

合成波導之設計與應用

研究生：吳憲順　　　　　　　　　　　　指導教授：莊晴光 博士

國立交通大學 電信工程學系

摘 要

本篇論文係研究立體式(Three-dimensional)與平面式(Two-dimensional)合成波導以多層印刷電路板(Multi-layer Printed Circuit Board)製程與矽(Silicon)半導體製程之實現並提出相關應用。傳統立體式矩形波導(Rectangular Waveguide)可藉由微小化週期結構 (Periodical Structure)重新合成，並透過成熟之矩形波導轉換器(Rectangular Waveguide Transition)，設計出合成矩形波導(Synthetic Rectangular Waveguide, SRW)。經由實驗與理論相互驗証，該立體傳輸線具備慢波效應(Slow-Wave Effects)可突破傳統矩形波導之理論限制，有效縮小面積達 60%以上。該微小化特性應用到 5GHz 積體化近全向性矩形波導天線 (Omni-directional Rectangular Waveguide Antenna)。更進一步，由於週期結構在能階止帶 (Energy Bandgap) 呈現出完美磁性金屬 (Perfect Magnetic Conductor) 特性，使該立體合成波導可傳播傳統金屬矩形波導無法存在之第一階橫向磁場模(TM_{10} mode) 而本論文亦針對該模態提出其模態轉換器 (Mode Converter)。

除外，本論文研究互補式金屬(Complementary-Conducting Strip, CCS)合成波導在多層結構 (Multi-layer Structure) 之特性與提出相關應用。透過實驗與理論驗証，互補式金屬在多層結構實現下，除保有原多樣化特徵阻抗合成之特性，亦突破傳統夾心線 (Stripline)之理論限制，具備更高之慢波因子 (Slow-Wave Factor)。該平面式合成波導以多層印刷電路板技術，應用在以傳輸線為主(Transmission-Line based) 之 WLAN 2.4GHz 微小化帶通濾波器設計。而設計出之濾波器尺寸為 5.0 mm X 5.0 mm X 0.18 mm，甚接近傳統以低溫陶瓷共燒 (Low Temperature Cofired Ceramic)之濾波器體積。

本論文最後一部份提出平面式合成波導應用於改進傳統晶片繞線電感(On-chip Spiral Inductor) 之設計困難。該設計同時以印刷電路板與標準多層 CMOS 製程驗証其可行性。

Design and Applications of Synthetic Waveguides

Student：**Hsien-Shun Wu** Advisor：**Dr. Ching-Kuang C. Tzuang**

Institute of Communication Engineering
National Chiao Tung University

ABSTRACT

This dissertation presents a new class of the transmission lines so-called synthetic waveguide, which can be realized by mass-producible technologies, such as multi-layer print-circuit-board (PCB), and silicon-based monolithic integrated circuit foundry. Meanwhile, the novel design methodologies incorporating the proposed synthetic waveguide are reported to demonstrate the impacts on the designs either in component-level or system-level for meeting the trends of modern portable devices. A new synthetic waveguide, which is the composite structure including the rectangular waveguide transitions and rectangular waveguide synthesized by the periodical electromagnetic bandgap (EBG) structures at top and bottom surfaces of the rectangular waveguide, is theoretically and experimentally verified, showing the following characteristics. First, the slow-wave factor of the synthesized rectangular waveguide (SRW) exceeds the theoretical limit of the conventional metallic rectangular waveguide in the TE_{10} mode, significantly increasing the size-reduction more than 60%. One example employing the TE_{10} mode of the proposed SRW was the design of integrated waveguide antenna in the 5 GHz ISM band, demonstrating its potential on circuit miniaturization. Second, the proposed SRW can support TM_{00} and TM_{10} mode propagation in the same SRW. Notably, no TM_{00} and TM_{10} mode can exist in the conventional rectangular waveguide with an all-metallic enclosure. Additionally, the waveguide transitions for the synthetic TE_{10}, TM_{00} mode, and TM_{10} mode of the SRW are also presented for the further applications.

The second part of the dissertation focuses on the design and application of the synthetic quasi-TEM transmission line so-called complementary conducting strip transmission line (CCS TL) in multi-layer portion. A series of experimental and theoretical verifications conclude that the stacked CCS TL not only provides a wide design solutions for the circuit requirements but also achieve a low-loss slow-wave device whose slow-wave factor (SWF) exceeding the theoretical value of the

conventional stripline. Moreover, a typical multi-layer system, which includes two filters in different signal layers, is realized by the stacked CCS TL, revealing good isolation between two filters during the system design. Furthermore, the proposed two-dimensional synthetic waveguide is applied to design an transmission-line based 2.4GHz ISM-band bandpass filter for demonstrating a new filter design methodology, which can systematically reducing the size of filter based on multi-layer CCS TL. A quick estimate on the prototype filter with the size of 5.0 mm X 5.0 mm X 0.18 mm reveals that the volume of the prototype approaches that of state-of-the-art device, such as multi-layer low temperature cofired ceramic (LTCC) filters.

Finally, the new spiral inductor architecture, named EBG enhanced inductor, incorporating the synthetic waveguide is presented, providing another solution for designing planar inductors on lossy substrate. The two-dimensional EBG array servers as a ground plane beneath the conventional spiral inductor, providing a shielding for inductor on the lossy substrate. The proposed approach is verified through the experiments using the conventional multi-layer PCB technology and standard 0.25um CMOS foundry, showing that the performance of a spiral inductor can be improved in almost aspects.

誌　謝

在新竹交大的求學生涯是一連串交織著驚喜與酸甜的自我成長。在此謹以誌謝表達深深地感激對曾經或永遠在我生命中留下痕跡的長輩與朋友。

謝謝莊晴光教授，從開始到現在，我的碩博士學位指導老師，以及他的家人，師母楊靜蘭女士、小圓、大慶及小萱。教授無私地分享對微波的愛與熱情，精神上與物質上的全心支持使我的求學舞台得以寬廣與多元。無疑地，教授的身教與言教更培養學生在面對困難與挫折時應有的心態與方法。曾一同面對連續五次審稿不過的窘況，也曾享受過一次審稿即過的喜悅。”不輕言放棄，誠實勇敢面對問題”是教授給學生最好的指導。額外地，師母的金玉良言與近乎完美的烹煮手藝、善解人意且笑容滿面的小圓、害羞又充滿音樂氣質的大慶與永遠充滿驚奇的小萱，這些家人們似的溫暖與親情陪我渡過在新竹求學許多週末夜晚。

謝謝楊晃瑞教授，在求學最低潮的時刻成為我的工作夥伴，為人生與工作帶來全新的體驗。爽朗的笑聲、感性的眼神與充滿生活藝術的言談最令人欣賞;工程上的精準、系統化的做事原則與高效率的執行力最令人敬佩。學生感謝有此緣份能與長輩工作、向長輩學習。

謝謝彭勁融工程師，從開始到現在，陪伴我在新竹整整七年時光。雖然各自的專業背景不同，亦所屬在不同的工作崗位;然感受到的是另一股對工作的投入與解決困難時的執著冷靜。有著不同的生活習慣與人生看法，這二仟多個相處日子裡，回味無窮。

謝謝毫米波體積電路實驗室的歷任助理，從開始到現在，李苑佳小姐、楊惠玲小姐、陳郁萍小姐和她們天真無邪、活力無窮的小朋友們。與專業秘書共事，從日常做人處事的小細節、面對決策時的多方思考與評估、對上司、同僚與下屬的聯絡與溝通都使晚輩見識到事情的推動不全然僅有技術或學理，協調與管理更是最後的關鍵。

懷念毫米波體積電路實驗室的所有成員。從開始到現在，國丞學長、正南學長、學達學長、經國學長、宣仲學長、耀德學長、國峰學長、毓喬學長、多柏學

長、嘉振學長、佐政學長、才弼、韶正、振榮、昌毅、慈惠、文翌、博議、文袒、鶴中、美蒨、竟谷、佳民、嘉良、智閔、書豪、揚裕、俊甫、繼禾與憲宏。曾一起相處的時光，有笑有淚、有甘有苦，希望有機會能再相聚。

謝謝全家人無止盡的關懷與支持。謝謝體諒我求學時少回家、少聯絡與晚歸。點點滴滴的付出雖不易察覺但意義與影響卻最深遠。謝謝未曾間斷且無所求的栽培，從最開始到現在，讓我無顧慮地完成所有學業並在最重要的時刻見證我的成長。謝謝永不變的贊美與叮嚀，使我面對挫敗時快快站起、面對成功時更能精益求精。

謝謝好朋友的幫助與溫暖的照顧。俊麟即時的線上咨詢與偶爾的探望、秀宜淡淡的問候與來信、涵秦小姐親切的叮嚀與協助、玉琇家姐般的照顧與驚奇的小禮物、珍儀逗趣的照片、貼心的手工皂與自製的護唇膏。讓我這一路走來，不曾孤單。

謝謝潛力無限的台大伙伴。孟儒、王珅、安錫、思賢、瑞琦、啟揚、昆宏、致嘉與彥翔。在求學的最後階段相互的交流與幫助，讓我在不同的環境下學習與成長，體驗到不同的學風與團體生活。

我繼續認真的學習，在台北、新竹與世界各地,

你投射過來關注的眼神, 詫異也好, 欣賞也罷,

或許引起我的目光

希望使你注意的　不是那稚嫩的臉龐,

而是我追求卓越的心

順子

TABLE OF CONTENTS

LIST OF TABLES

LIST OF FIGURES

CHAPTER 1
Introduction

1.1 *Background*

Portable wireless devices have evolved into the convergence realm, integrating multi-frequency and multi-standard protocols. One key factor for such success of wide acceptance is the miniaturization of wireless apparatus. The continuing improvement of semiconductor processes, shrinking photolithography, and multi-layer integration technologies such as the low temperature cofired ceramics (LTCCs) and printed circuit boards (PCBs) lead the continuing technological development in system-on-chip (SOC) and system-in-package (SIP) [1-7]. Although as many as possible wireless building blocks have been integrated into SOC, the radio frequency (RF) front-end module (FEM) and other devices are mostly in discrete forms or embedded into the SIP. A complete solution for making a wireless device with a very small form factor is becoming a reality by combining advanced techniques of SOC and SIP.

On the other hand, closely examining the integration scheme of the FEM, the functional blocks, including antenna, filter, balun, etc., and various transmission lines which are designed based on different circuit principle and realized by different technologies, may require additional transitions to establish the smooth interfaces between the adjacent building blocks. Additionally, two kinds of transmission lines, which are connected, require the mode converter for the energy transformation. Those transitions and mode converters also become an important part during the components design and seriously dominate the performance and appearances of the FEM.

In the Year 2000, a new design methodology so-called the advanced coplanar strips system (ACSS) was proposed for in millimeter-wave module and RFIC designs [8]. The ACSS is a system of guiding structures embedded in a multilayered printed-circuit environment such as print circuit board (PCB) and low temperature cofired ceramics (LTCC) for RF system-on-chip (SOC) design. The ACSS millimeter-wave transceiver module, which incorporates typical PCB process for making all-in-one module, has demonstrated all aspects of planar realizations of antennas, antenna arrays, resonators, filters, mixers, oscillators and packages [9]. The ACSS exploits the multi-layered guiding system into the unprecedented domain, which creates new approaches for RFIC design and module integration. The unprecedented domain is best described by the concepts of the synthetic waveguides in which most popularly known guiding modes such as planar (microstrip), quasi planar (CB-CPW), non-planar (rectangular waveguide) structures propagate freely in the multi-layered ACSS system with a little increasing of propagation losses or transition losses.

In the 2005 international microwave conference (IMS2005), the transmission line community organized a section titled "***Synthetic Transmission Lines and Their Applications***", revealing the trends of the researches on synthetic waveguides [10-14]. This special section demonstrated a single processing technology, achieving unprecendted guiding characteristics such as high slow-wave factor, wide solutions of characteristic impedance syntheses, and build-in transitions for the system integrations. The efforts organized by IMS2005 sub-community faithfully reflected the contributions of this dissertation undertaken in the past six years. Perhaps on e best notion on the synthetic waveguide could be quoted from an invited speech at City University of Hong-Kong in July 2004, when Professor Ching-Kuang C. Tzuang gave a seminar on the synthetic waveguide and its applications to the RF SOC and SIP designs. This dissertation covers all aspects of the synthetic waveguide as quoted above.

Incompatible guiding structures, which are conventionally made by different technologies, are blended into a mass-producible technology or new waveguide structures that exhibit extraordinary characteristics, behaviors, and merits using the same mass-producible technology belong to the domain of synthetic waveguide.

1.2 *Review of Synthetic Waveguides*

Fig. 1 shows the developing trends of the synthetic waveguide in the past ten years. An amount design of the synthetic waveguides is involved with the periodical structures, which can be classified by photonic bandgap (PBG), electromagnetic bandgap (EBG), Metamaterials, and etc.. One example of designing synthetic waveguide with periodical structure is proposed by Itoh et al. in 1998 [15].

The microstrip line incorporating the uniplanar compact photonic bandgap (UC-PBG) ground plane become a new slow-wave device. Additionally, this new slow-wave transmission line, which differs from the thin-film transmission lines reported from 1970 to 1993, can achieve small attenuation constant less than one dB per guiding wavelength [16]. Such synthetic waveguide is realized by the conventional print circuit board (PCB) technology and had been demonstrated its wide applications on the microwave active and passive circuits, including improvement of power amplifier efficiency, and bandpass filter design with wide-band rejection [17].

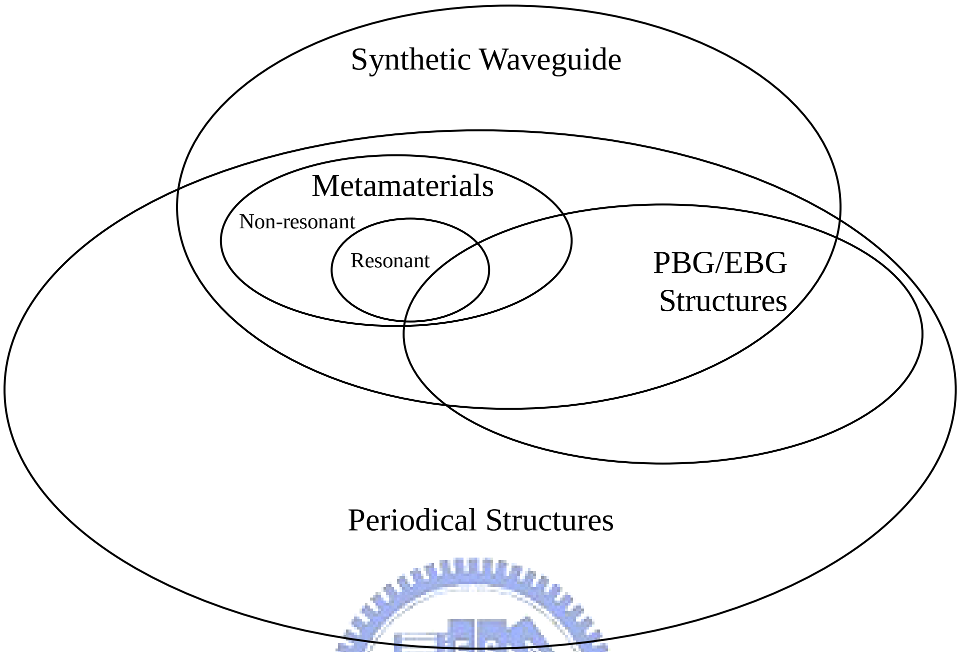

Fig. 1.1 Development trends of Synthetic Waveguide.

Another example of synthetic waveguide incorporating with periodical structure is reported by Tzuang et al. in 2001 [18]. The signal trace of the conventional microstrip consists of the coil-coupled electromagnetic bandgap (EBG) cells, revealing electric, magnetic and electric properties along the transverse plane of the microstrip line [16]. The modal behavior of the electric-magnetic-electric (EME) microstrip line had been carefully investigated, revealing the first high-order mode of EME microstrip line can be controlled and synthesized in different frequencies. Such new modal behavior is also applied to design a dual-band leaky wave antenna [19].

On the other hand, the synthetic waveguides, which can be synthesized to exhibit the negative permittivity and permeability, are classified as the metamaterials. Metamaterials are commonly referred to as left-handed (LH) transmission lines because of their unique guiding characteristics such as the reversal of Snell's Law, the Doppler effect, and the VavilovCerenkov effect, which is the radiation produced by a fast-moving particle as it travels through a medium [20].

The idea of left-handed (LH) transmission line was first presented by the Russian physicist Veselago in 1967. Veselago theoretically showed that the electric field, magnetic field, and wavevector of an electromagnetic wave in an LH transmission line form a left-handed triad. Therefore, LH transmission lines support energy propagation with group and phase velocities that are antiparallel, a phenomenon which is associated with negative index of refraction [21]. The experimental verifications of metamaterials were performed by the Smith et. al in 2001 [22]. During the experiments, the metamaterial was realized by a wedge-shaped two-dimensional periodical array consisting of the magnetic resonator so-called split-ring resonators (SRRs) and thin conducting wires. The periodical array was excited by the plane wave and the wavefront of the transmission wave traveled backward toward the incident wave, confirming the existing of negative index of refraction [22]. Parallel to the findings of Smith, the planar LH transmission line based on SRRs is also reported in the very recently [23-24].

On the other hand, the composite right/left hand (CRLH) transmission line (TL) realized by the non-resonant elements is also reported by Itoh et al. [25]. The characteristics of CRLH TL have been investigated by the transmission line theory and its guiding properties are modeled by a lossless LC network. Furthermore, the development of equivalent LC network, which consists of shorted shunt stubs and series inter-digital capacitors, is also presented [26]. Both theoretical and experimental results show that the CRLH TL can propagate the electromagnetic wave with the right-handed and left-handed triads alternatively [27]. Many applications based on CRLH TL are also reported for demonstrating the capability of such new planar synthetic waveguide [28-32].

This dissertation focus on the development of synthetic waveguides which have three main features: 1) Compact circuit design is compared to those based on popularly known guiding structures, 2) High Q-value of the guiding structure is maintained or much better than the conventional guides, and 3) practical realization is based on the existing technologies without any modifications.

1.3 *Organization*

The first kind of synthetic waveguide, presented in Chapter 2, is named synthetic rectangular waveguide (SRW). The SRW, which is consist of two electrical sidewalls and two parallel periodical structures placed at top and bottom surfaces of the waveguide, is made by multi-layered integrated circuit processes with large ratios of SRW lateral dimensions to substrate thickness. The two-dimensional periodical structures comprise unit cells made of coupled coils; show a slow-wave region for the lowest band and a stopband region above the slow-wave region. Chapter 2 reports both theoretically and experimentally that combining the two distinct regions of propagation of two-dimensional periodical structures leads to the design of a SRW that simultaneously exhibits the following unique characteristics. First, the slow-wave factor of the particular SRW significantly exceeds the theoretical limit of $\sqrt{\varepsilon_r}$ for the conventional metallic rectangular waveguide in the TE_{10} mode. Second, SRW can support the propagations of TM_{00} and TM_{10} modes in the same SRW. Notably, no

TM_{00} and TM_{10} mode can exist in the conventional rectangular waveguide with an all-metallic enclosure. Third, the *Q*-factor of the SRW is high in TE_{10} mode, TM_{00} mode, and TM_{10} mode for the particular case study. Fourth, the waveguide transitions, including the tapered microstrip, the finline, and tapered coplanar waveguide (CPW), are integrated with the SRW in the same polymer substrate for the synthetic TE_{10}, TM_{00} mode, and TM_{10} mode converters, respectively. One example employing the TE_{10} mode of the proposed SRW was the design of miniaturized four-slot antenna array in the 5 GHz ISM band to demonstrate the compact appearance, high antenna gain using a conventional FR4 substrate.

Chapter 3 presents the second kind of synthesized waveguide named stacked complementary conducting strips (CCS) transmission line (TL). Notably, CCS TL was reported recently to be an effective means of miniaturizing microwave circuits [33]. However, in this dissertation, the stacked CCS TLs, which are separated by a meshed ground plane in a multi-layer print-circuit-board (PCB) structure, are introduced for the first time. A practical example is employed to verify the isolation, showing a high level of satisfactory with negligible effects on desired circuit performances. Furthermore, the proposed artificial transmission line is applied to the design of a 2.4 GHz ISM-band bandpass filter prototype of a size that approaches that of state-of-the-art device. The application of the stacked CCS TL results in the filtering of almost nearly the same volume as the number of substrates is increased. A designer can therefore optimize the area and thickness required for product integration. A quick estimate of the miniaturized filter design based on stacked CCS TL shows that the particular filter prototype approaches the process limit.

Chapter 4 explores the application of synthetic waveguide to the design of PCB and monolithic spiral inductor. The microstrip on the electromagnetic bandgap (EBG) ground plane has been experimentally verified, showing that the increasing characteristic impedance and reducing propagating loss of the synthetic waveguide can be established simultaneously for the operation frequency below the first stopband, leading to the design of a new inductor configuration or the so-called EBG enhanced inductor. The EBG enhanced inductor consists of a two-dimensional electromagnetic bandgap (EBG) periodical array beneath the conventional spiral inductor. A physical model is presented to investigate both characteristics and physical insights of the proposed inductor architecture. Both laminated and monolithic spiral inductors are designed and tested to demonstrate that the performance of the spiral inductor can be improved in almost aspects by placing the EBG ground plane beneath the spiral inductor.

Chapter 5 summarizes the contributions of the dissertation and identifies the future works.

CHAPTER 2

Integrated Synthetic Rectangular Waveguide

In this chapter, the first find of synthetic waveguide, named synthetic rectangular waveguide (SRW), is presented. An SRW, which is made of two laminated two-dimensional (2D) periodical structures and a substrate sandwiched between the 2D structures. The SRW is made by multi-layered integrated circuit processes, which typically have large ratios of SRW lateral dimensions to substrate thickness. Theoretical investigations of the periodical structures show that the corresponding Brillouin diagram have the lowest band of normalized propagation constant much higher than the square root of the relative dielectric constant ε_r of the substrates. Application of the dispersion characteristics of the two-dimensional periodical structures coupled with appropriate mode converter designs leads to results in SRW designs supporting TE_{10}, TM_{00} and TM_{10} modes.

Section 2.1 shows the slow-wave and high-impedance-surface behaviors of the two-dimensional periodical structures. Additionally, a simplified behavior model for the SRW is also presented for predicting the various modal behaviors in the SRW. Section 2.2 describes the de-embedding procedures to remove the effects of the mode converters necessary to interface the SRW to external measurement ports for TE_{10},

TM_{00} and TM_{10} modes. The de-embedded data are applied to validate the results obtained by the finite element method (FEM). Section 2.3 reports the newly TE_{10} mode SRW with a cutoff frequency that is much lower than that of the all-metallic rectangular waveguide based on the same structural and material constants; the slow-wave factor of the TE_{10} mode SRW is also significantly greater than $\sqrt{\varepsilon_r}$, which is the theoretical limit of a conventional rectangular waveguide. ε_r is the relative dielectric constant of the PCB substrate. Section 2.4 investigates the propagations of TM_{00} and TM_{10} modes of the same SRW. Notably, no TM_{00} and TM_{10} mode can exist in the conventional rectangular waveguide with an all-metallic enclosure. Finally, one example, which employs the TE_{10} mode of the proposed SRW for designing a four-slot waveguide antenna in the 5 GHz ISM band, is presented in Section 2.5. The antenna is built and tested, showing the gain of 4.28 dBi, 60 percent area reduction in waveguide cross-section, measuring 71.0 mm x 10.5 mm x 0.9 mm (including the microstrip-to-waveguide transition) on a conventional FR4 (ε_r=4.1) substrate.

2.1 *Synthetic Rectangular Waveguide: Design and Operational Principles*

Figure 2.1(a) illustrates the conventional rectangular waveguide made using four smooth metal plates. If the top and bottom metal plates are replaced by perfect magnetic conductors (PMC) as shown in Fig. 2.1(b), the guiding characteristics of the conventional rectangular waveguide are drastically changed. This paper presents a new approach for designing integrated rectangular waveguides. As illustrated in Fig. 2.1(c), the integrated synthetic rectangular waveguide (SRW) consists of two vertical plated sidewalls and two EBG surfaces replacing the top and bottom plates of Fig. 2.1(a). The proposed SRW can support propagating modes in both rectangular waveguides as shown in Figs. 2.1(a) and (b). The SRW extensively applies the propagation characteristics of periodical structures.

2.1.1 Dispersion Characteristics of Parallel-Coupled Electromagnetic Bandgap (EBG) Surfaces

In the SRW, the two-dimensional periodical array, or the so-called EBG surface, constitutes both top and bottom metallic surfaces of the conventional rectangular waveguide. Figure 2.1 (d) details the unit cell design of the EBG surface. The unit cell consists of a pair of connected spiral coils; one is located at the top surface and the other at the bottom surface. The connected spiral coils are DC-connected by a through-hole at the center. The spiral coils form coupled inductors, and the overlapped area between the spirals creates additional capacitances. Furthermore, inductive and capacitive couplings also exist between adjacent cells. Thus the propagation characteristics of the periodical structure are highly dispersive. The full-wave finite-element-based simulation package HFSS^{TM} is applied to obtain the dispersion characteristics of the multi-layered two-dimensional periodical structure of Fig. 2.1(d). In the numerical investigation, two pairs of master-slave boundaries of assumed phase differences were placed at four edges of the unit cell to compute a corresponding complex frequency of the eigenvalue, from which the phase and attenuation constants (γ=β-$j\alpha$) of the two-dimensional periodical structure were obtained [33].

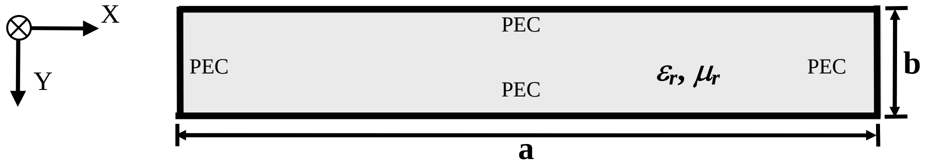

(a)

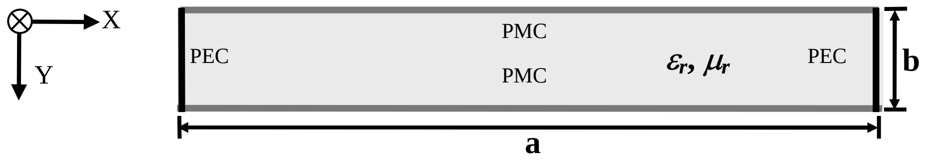

(b)

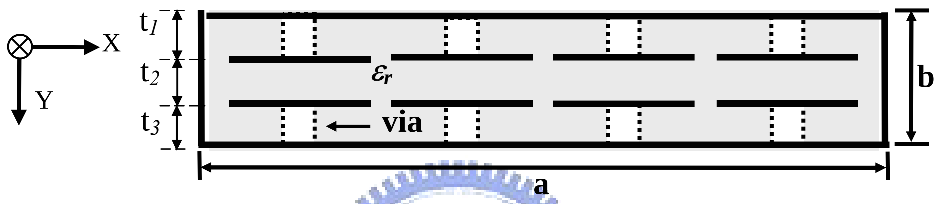

(c)

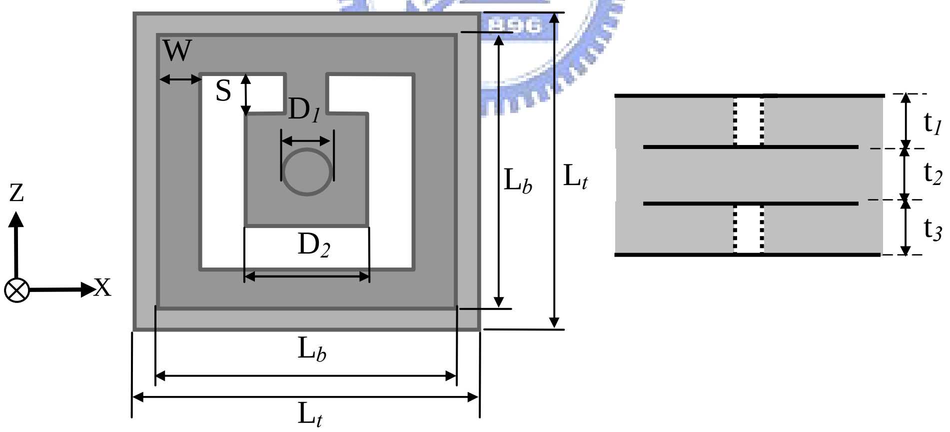

(d)

Fig. 2.1 Rectangular waveguide structures (a) using all-metallic enclosure: a = 7.0 mm, b = 0.609 mm, ε_r = 3.38, tanδ = 0.0035, (b) top and bottom surfaces incorporating perfect magnetic conductor (PMC) (c) proposed SRW: t_1 = t_2 = t_3 = 0.203 mm (d) EBG unit cell applied in SRW: W = 0.2 mm, S = 0.2 mm, D_1 = 0.25 mm, D_2 = 0.55 mm, L_t = 1.55 mm, L_b = 1.35 mm.

Perfect matching layers (PMLs) were placed adjacent to the top and bottom surfaces of the unit cell with to absorb the radiated waves. Figure 2.2 plots the corresponding Brillouin diagram of the EBG cell. The straight solid (dashed) lines represent the propagation of the transverse electromagnetic (TEM) mode in free-space (dielectric medium with relative permittivity of ε_r). These straight lines form two triangles, as shown in Fig. 2.2. The region outside the solid triangle belongs to the radiation zone. Inside the solid triangle, however, is the bound mode region. In this case study, predominant TEM solutions were observed inside the triangle formed by the dashed lines for operating frequencies below 9.85 GHz, manifesting the slow-wave factor greater than $\sqrt{\varepsilon_r}$, which is the upper ceiling for most conventional guided-wave structures. The electric (magnetic) fields are mostly perpendicular (parallel) to the spiral coils and negligible field components are observed along the direction of propagation. Near zero operating frequency, the phase constant asymptotically approaches that of the TEM mode in the dielectric medium with ε_r. Near 9.85 GHz, the group velocity approaches zero. The magnitude of the modal currents near cutoff becomes much smaller than that of the predominant TEM mode at 5.0 GHz. Above 15 GHz, predominant TE mode solutions were observed, since, electric fields exist only in the plane transverse to the direction of propagation. Thus the TE mode is designated as the first high-order mode of the periodical structure shown in Fig. 2.1 (d). Below 9.85 GHz, the EBG periodical structure is a slow-wave guiding structure, establishing the core operational principle for designing miniaturized integrated SRW.

Equally importantly that the Brillouin diagram shows a broad spectrum of forbidden band between 9.85 and 15.0 GHz. Such stopband connected to the high impedance surface, or the so-called magnetic surface, had been extensively studied [34-35]. Thus the SRW of Fig. 2.1(c) seems to exhibit guiding properties closely resembling those of Fig. 2.1(b) in the forbidden band. In the passband below 9.85 GHz, however, the SRW is more like the conventional rectangular waveguide shown in Fig. 2.1(a).

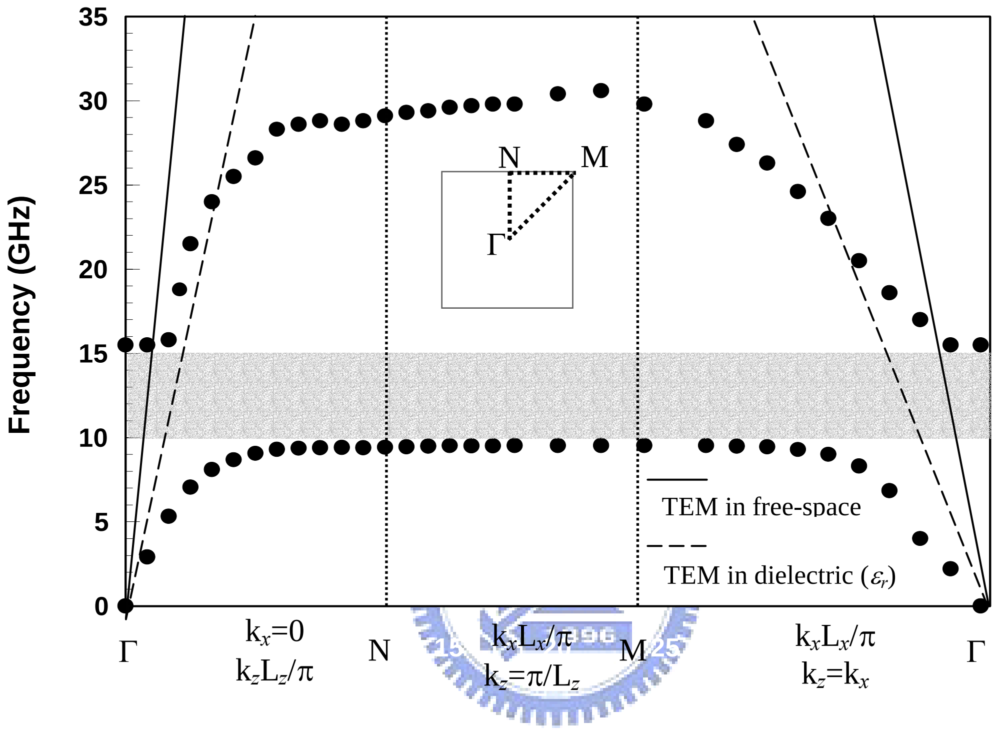

Fig. 2.2 Brillouin diagram of the two-dimensional periodical array made of unit cell of Fig. 2.1 (d).

2.1.2 Simplified Rectangular Waveguide Models for SRW

As mentioned above, electromagnetic bandgap (EBG) surfaces, which form both top and bottom layers of the synthetic rectangular waveguide (SRW), behave like magnetic walls (electrical walls) in the stopband (passband). Therefore, Figs 2.1 (a) and (b) represent simplified rectangular waveguide models of the SRW. Since the proposed SRW is realizable by multi-layered integrated circuit processes, the lateral dimensions (along the *x*-axis) of the SRW are typically much larger than the thickness of the substrate along the *y*-axis. Consequently, the lowest order TE modes of Fig. 2.1(a) are TE_{10}, and TE_{20}, etc., whereas the lowest TM modes of Fig. 2.1(b) are TM_{00}, and TM_{10}, etc. TM_{00} mode is essentially a TEM mode with uniform transverse E_x and H_y fields in the waveguide cross-section, which manifests the TEM mode waveguide as reported by D. Sievenpiper et. al [36], T. Itoh et. al [35], and Per-Simon Kildal et. al [37], respectively. The procedures for deriving the solutions of TE_{n0} modes are well-documented [38]. The same procedures are also applied to investigating the TM_{m0} modes of idealized SRW.

For TE_{n0} modes:

$$k = \frac{\omega}{c}\sqrt{\varepsilon_r \mu_r} \quad (1),$$

where k is the wave number of the dielectric medium with relative permittivity ε_r and relative permeability μ_r.

$$\beta_n = \sqrt{k^2 - (\frac{n\pi}{a})^2}, n = 1,2,3,... \quad (2),$$

where n represents order of the TE mode and a is the lateral dimension of SRW in x-direction. The lowest order mode is the TE_{10}. Only three field components exist for the TE_{n0} mode, namely,

$$E_y = -j\omega\mu_0\mu_r aH_0 \sin(\frac{n\pi}{a}x)e^{-j\beta_n z} , \quad (3)$$

$$H_x = j\beta aH_0 \sin(\frac{n\pi}{a}x)e^{-j\beta_n z} , \quad \text{and} \quad (4)$$

$$H_z = H_0 n\pi \cos(\frac{n\pi}{a}x)e^{-j\beta_n z} . \quad (5)$$

The TE_{n0} mode has a cutoff frequency strictly related to lateral dimension a, order n, and material constants, i.e.,

$$f_{cutoff,\mathrm{TE}_{n0}} = \frac{nc}{2a\sqrt{\varepsilon_r\mu_r}} \quad (6)$$

For TM_{m0} modes:

$$\beta_m = \sqrt{k^2 - (\frac{m\pi}{a})^2}, m = 0,1,2,... \quad (7),$$

where m represents order of the TM mode and a is the lateral dimension of SRW in x-direction. The lowest order mode is the TM_{00}, which is the zero-cutoff limit of TM $_{m0}$ modes. Only three field components exist for the TM_{m0} mode, namely,

$$H_y = -j\omega\varepsilon_0\varepsilon_r aE_0\cos(\frac{m\pi}{a}x)e^{-j\beta_m z} \quad (8)$$

$$E_x = -j\beta_m aE_0\cos(\frac{m\pi}{a}x)e^{-j\beta_m z} \quad (9)$$

$$E_z = E_0 m\pi \sin(\frac{m\pi}{a}x)e^{-j\beta_m z} \quad (10)$$

The TM_{m0} mode has a cutoff frequency strictly related to lateral dimension a, order m, and material constants, i.e.,

$$f_{cutoff,TM_{m0}} = \frac{mc}{2a\sqrt{\varepsilon_r\mu_r}} \quad (11)$$

It is interesting to notice that the interchange of E and H, sine and cosine leads to the interchange of TE_{n0} and TM_{m0} modes. Additionally, the SRW shows different dispersion characteristics from those of idealized TE_{n0} and TM_{m0} modes. In the later sections, we will show that the TM_{00} mode of the SRW has a cutoff frequency and that both TE_{10} and TM_{10} modes have different cutoff frequencies, not dictated by (6) and (11).

2.2 *Synthetic Rectangular Waveguide: Waveguide Transitions to Planar Transmission Lines, and De-embedding Studies*

2.2.1 Integrated Synthetic Rectangular Waveguide (SRW)

As shown in Fig. 2.1 (c), the synthetic rectangular waveguide (SRW), was formed on a RO4003^{TM} printed circuit board (PCB) with a relative dielectric constant of 3.38 and a tanδ of 0.0035. The metal printed on the substrate was copper with a thickness of 17 μm. Notably, the electromagnetic bandgap (EBG) surface comprised four unit cells in the transverse direction of the SRW. Similar design had been reported and applied in designing the dual-band leaky-mode antenna [39], indicating that the design of the EBG surface shown in Fig. 2.1(c) has stopband characteristics similar to those two-dimensional arrays of infinite number of cells.

The propagating energy of the synthetic rectangular waveguide (SRW) must be interfaced to planar guiding structures to become a useful integrated guiding device. This section describes various designs to interface SRW supporting TE_{10}, TM_{00}, and TM_{10} modes. A streamline mode converter made of a tapered microstrip has been successfully demonstrated as a good waveguide transition device to interface a microstrip line and a rectangular waveguide supporting TE_{10} mode [40-44]. The *E*-field of this tapered microstrip mode resides mostly in the transverse *y*-direction in the same way the TE_{10} mode does, thus ensuring smooth field transition in the mode converter. Parts (a), (b), and (c) of Fig. 2.3 show top, front, and side views of a back-to-back connected SRW supporting TE_{10} mode with interfaces to two external microstrip ports.

Resorting to (9) the TM_{00} mode exhibits a constant *E*-field polarization in the *x*-direction, suggesting a symmetric perfect electric conductor (PEC) plane at $x = a/2$. Therefore, a tapered finline inserted on the horizontal plane of $y = b/2$ is proposed for the TM_{00} SRW waveguide transition as illustrated in parts (a), (b), and (c) of Fig. 2.4. Likewise a tapered finline is the waveguide transition for TM_{00} mode SRW. Figure 2.5 illustrates how a tapered CPW, which is symmetrical about a perfect magnetic conductor (PMC) surface at $x = a/2$, works as a TM_{10} mode converter.

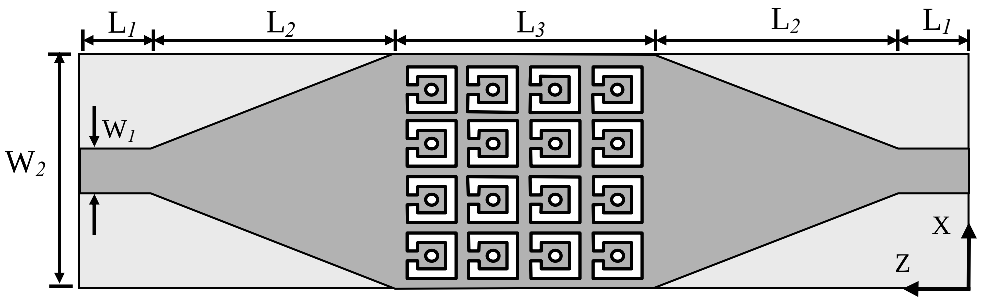

(a)

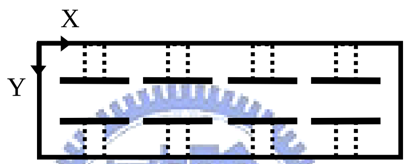

(b)

(c)

Fig. 2.3 TE_{10} mode SRW including microstrip-to-waveguide transitions (a) top view: L_1=3 mm, L_2=8 mm, L_3=7.2 mm, W_1=0.8 mm, W_2=7 mm, (b) front view: waveguide thickness (y-axis) = 0.609 mm, (c) side view.

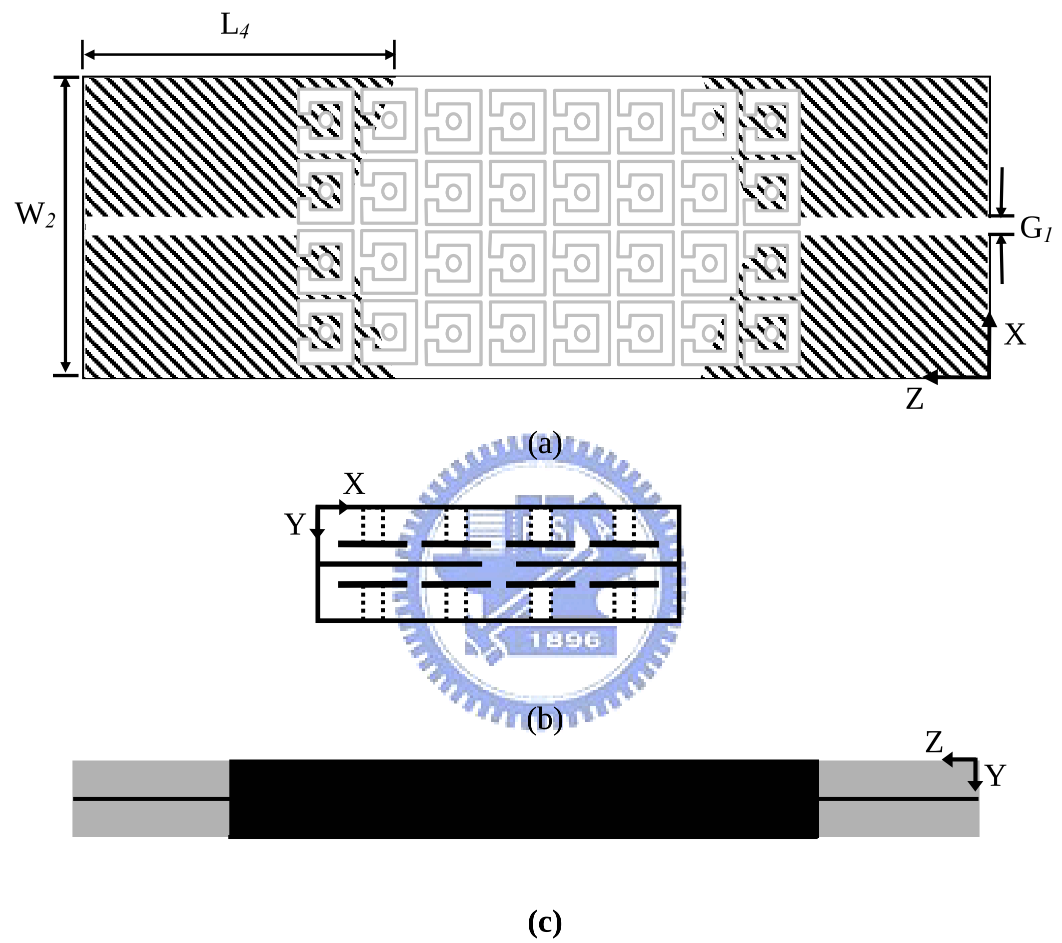

Fig. 2.4 TM_{00} mode SRW including slotline-to-waveguide transitions (a) top view: G_1 = 0.15 mm, L_4 = 13.05 mm, (b) front view: waveguide thickness (y-axis) = 0.609 mm, (c) side view.

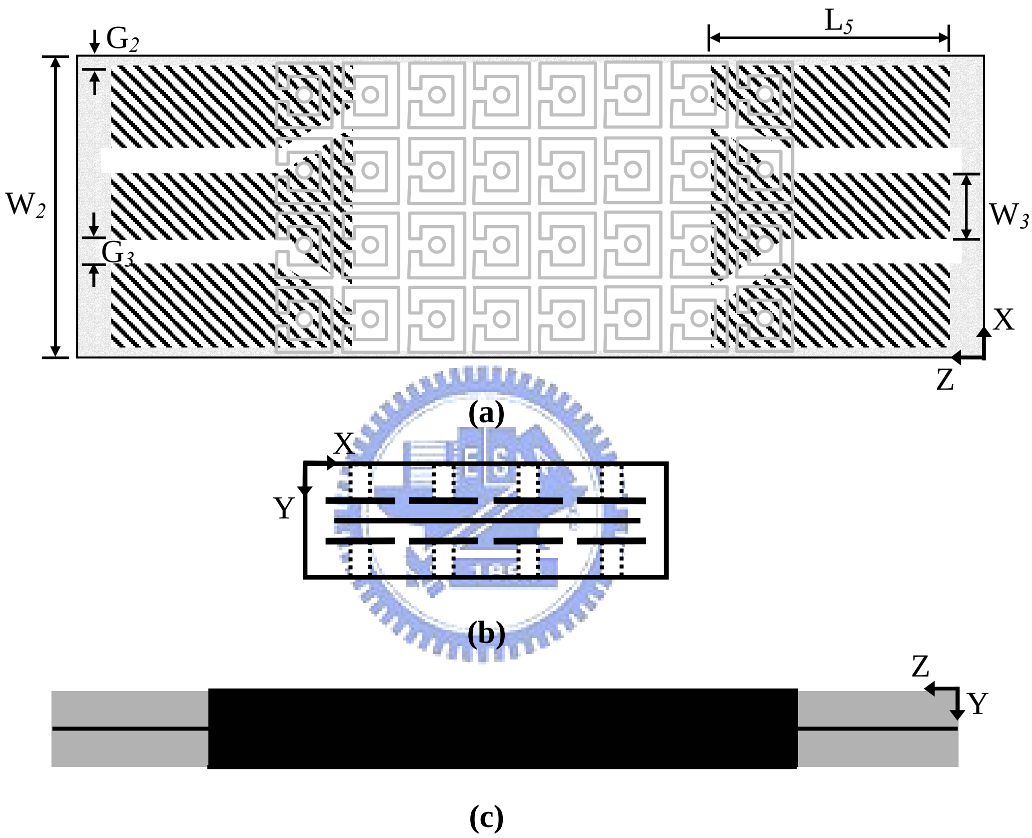

Fig. 2.5 TM_{10} mode SRW including CPW-to-waveguide transitions (a) top view: G_2 = 0.425 mm, G_3 = 0.7 mm, L_5 = 12.85 mm, W_3 = 0.75 mm, (b) front view: waveguide thickness (y-axis) = 0.609 mm, (c) side view.

2.2.2 Single-Mode Approximate Algorithm for De-embedding Integrated Synthetic Rectangular Waveguides (SRW)

As mentioned above, the integrated synthetic rectangular waveguide (SRW) consists of the SRW and additional waveguide transitions. The effects of mode converters must be de-embedded to obtain the propagation characteristics of the SRW out of two-port scattering analyses or measurements. Herein a single-mode approximation as depicted in Figure 2.6 is presented. The overall measured/theoretical transmission matrix $[T]_{total}$ of the integrated SRW, including two mode converters and the SRW, was obtained by converting the measured/theoretical S-parameters to T-parameters [45]. The measurement was conducted after the SOLT (short-open-load-through) calibration procedures that had been performed by the HP8510C^{TM} vector network analyzer. The theoretical analysis of the test device, however, was based on HFSS^{TM} full-wave scattering simulation. Next, the $[T]_{tran}$ of the mode converter was obtained theoretically by HFSS^{TM} based on the single-mode approximation by assuming microstrip, finline, and coplanar waveguide mode of propagation for TE_{10}, TM_{00}, and TM_{10}, respectively. Then the $[T]_{SRW}$ was obtained by pre- and post-multiplying $[T]_{total}$ by the inverse of $[T]_{tran}$. Finally, $[S]_{SRW}$ was obtained by simply converting the corresponding $[T]_{SRW}$ into the $[S]_{SRW}$.

To validate the de-embedding procedure of Fig. 2.6, conventional TE_{10} mode rectangular waveguide with the structural and material constants shown in Fig. 2.1(a) and tapered microstrip mode converter shown in Fig. 2.3 were investigated. Initially, the two-port scattering parameters of the end-to-end integrated rectangular waveguide obtained by measurement and by HFSS^{TM} simulation were compared. Figure 2.7 shows the comparisons. Both data show excellent agreement in magnitude and phase. Then, the measured overall two-port scattering parameters were de-embedded to obtain the complex propagation constant of the conventional rectangular waveguide.

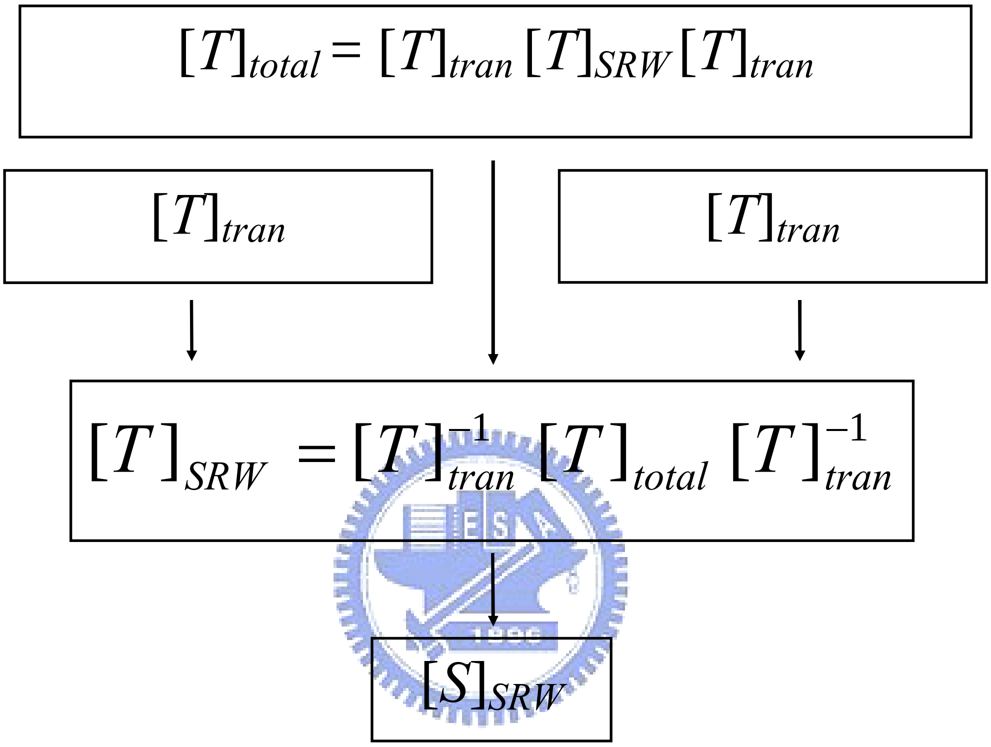

Fig. 2.6 Proposed de-embedding procedures for extracting guiding characteristics of the planar rectangular waveguide.

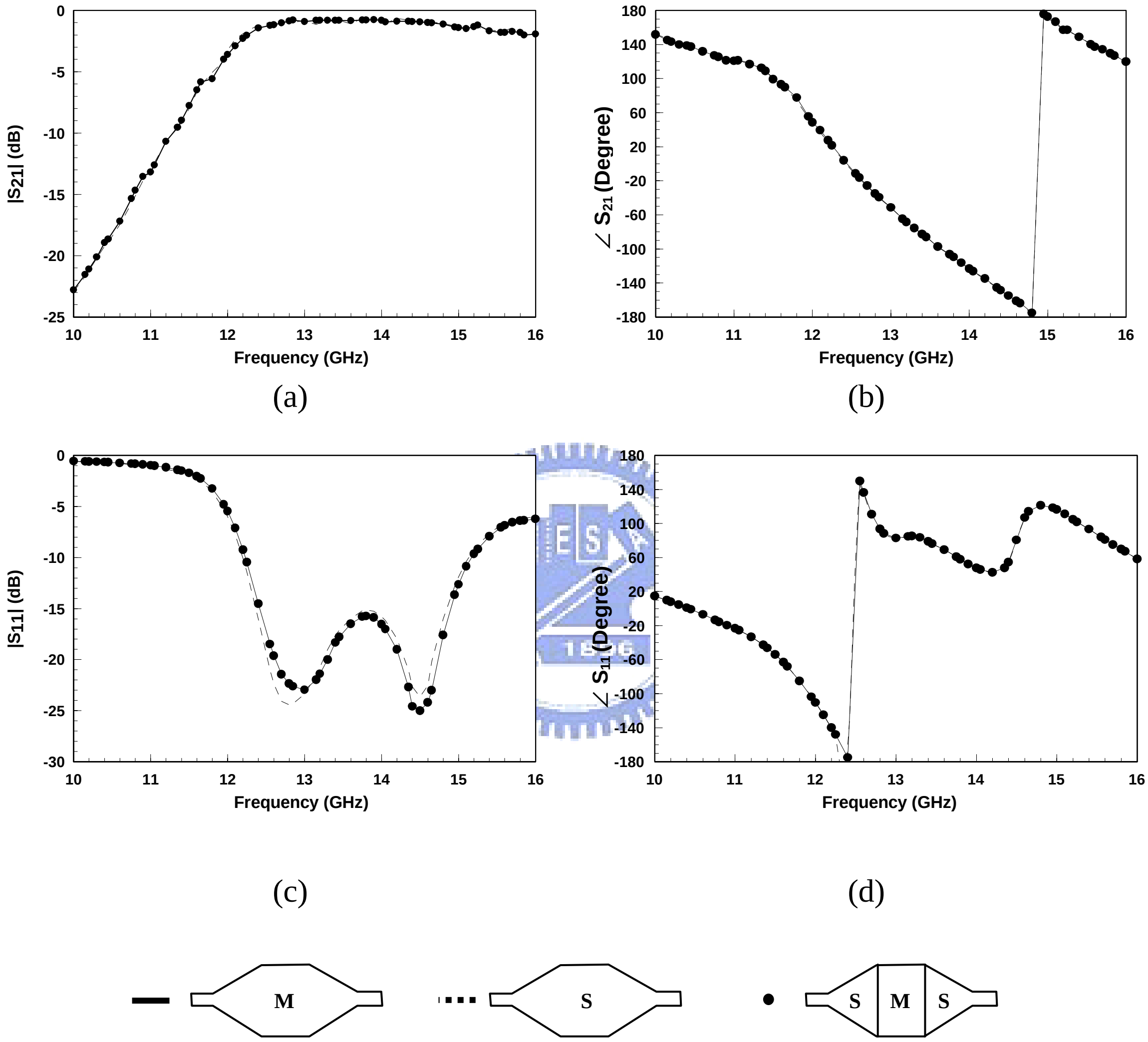

Fig. 2.7 Validity check of the proposed de-embedding method for extracting rectangular waveguide parameters: (a) $|S_{21}|$ (b) $\angle S_{21}$ (c) $|S_{11}|$ (d) $\angle S_{11}$

Figure 2.8 compares the extracted results with those obtained (2), showing excellent agreement between the two data sets. Therefore we conclude that the single-mode approximation assumed in the de-embedding procedure of Fig. 2.6 is a good approximation for de-embedding the integrated TE_{10} mode SRW as shown in Fig. 2.3. In Sections 2.3 and 2.4, the single-mode approximate de-embedding procedure was applied to recover the complex propagation constant of the integrated SRW supporting TE_{10}, TM_{00}, and TM_{10} modes. The Q-factor of the conventional rectangular waveguide was also investigated using the basic theory of a rectangular waveguide cavity [45]. The total Q-factor of the conventional rectangular waveguide is the inverse of the summation of $1/Q_d$ and $1/Q_c$ where Q_d and Q_c are the Q-factors of the rectangular waveguide with dielectric loss and conductor loss, respectively. The conducting walls, having high conductivity and a thickness of 17 μm, more than five times the skin depths above the cutoff frequency, were applied to realize a conventional rectangular waveguide, whose Q_c is about 9650, between 12 and 20 GHz. However, Q_d, which is proportional to the inverse of the tanδ value of the substrate in the rectangular waveguide, is about 285.7, dominating the power dissipation in the rectangular waveguide. Therefore, the theoretical Q-factor of the conventional rectangular is about 277. However, the measured Q-factor, extracted from the de-embedded propagation constant of the conventional rectangular waveguide, without the effects of the mode converters, is about 275 between 12 and 20 GHz, indicating close agreement between the measured results and the theoretical predictions.

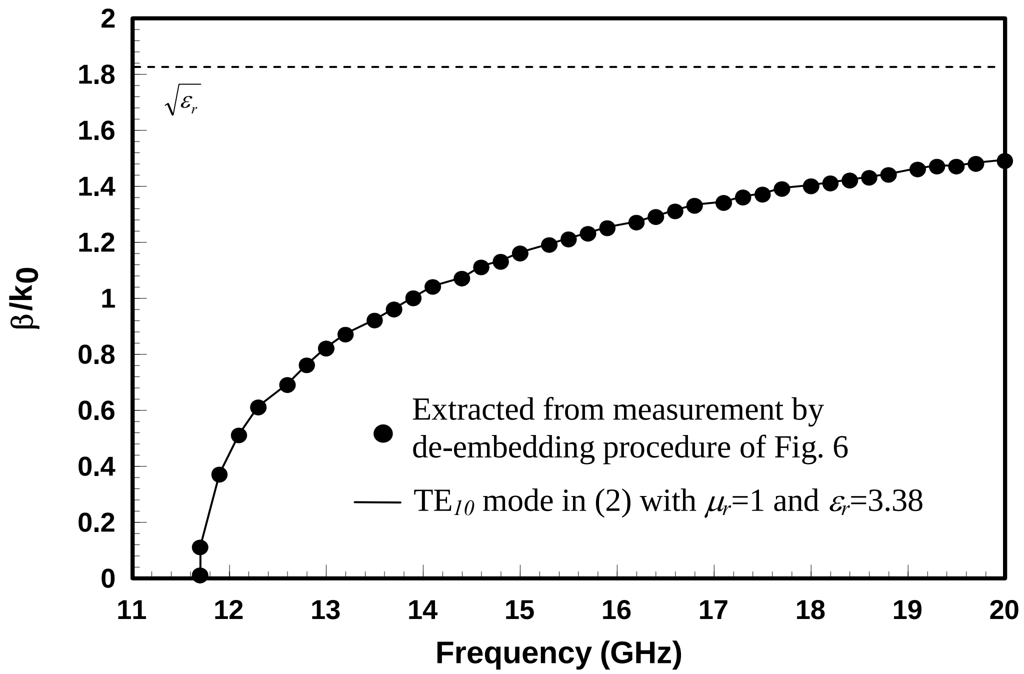

(a)

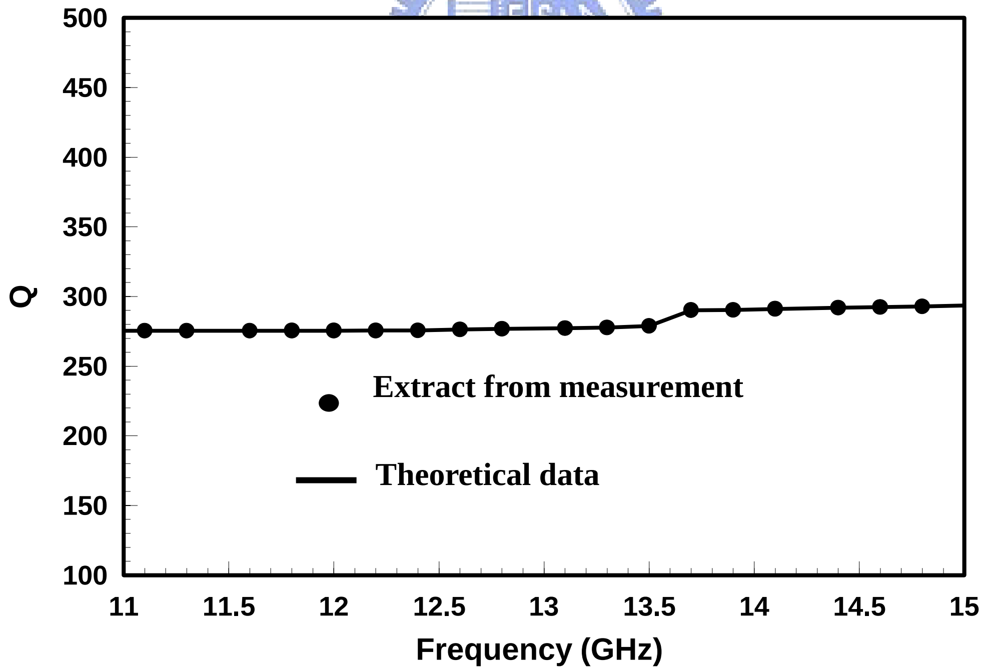

(b)

Fig. 2.8 Comparison of the extracted normalized phase constants of the conventional rectangular waveguide with those obtained by exact equation: (a) phase constant, (b) Q-factor.

2.3 *TE_{10} Mode Synthetic Rectangular Waveguide (SRW)*

Parallel to obtaining the dispersion diagram of two-dimensional periodical structure made of unit cells shown in Fig. 2.1(d), the master-slave boundaries along the z-direction (longitudinal axis) of Fig. 2.1(c) were applied to solve the complex propagation constant for the SRW. Measured two-port scattering parameters of the integrated TE_{10} mode SRW shown in Fig. 2.3 were also obtained, then the de-embedding procedure of Fig. 2.6 was invoked. Figure 2.9 shows measured and theoretical two-port S-parameters of TE_{10} mode SRW. Both data show excellent agreement in magnitude and phase.

Fig. 2.10 compares the normalized phase constants (slow-wave factors) obtained by two approaches, showing excellent agreement between the extracted measured data and theoretical results. The cutoff frequency of the TE_{10} mode SRW was almost 4.10 GHz, which is 0.348 times the cutoff frequency of 11.7 GHz of the conventional waveguide with the same outer dimensions and material constant. The slow-wave factor of the TE_{10} mode SRW rises quickly to the theoretical limit $\sqrt{\varepsilon_r}$ at 4.38 GHz from the cutoff frequency. Then the slow-wave factor ascends almost linearly to 4.35 at approximately 5.78 GHz. Then it levels off to 4.9 at 6.85 GHz. Meanwhile, the de-embedded Q-factor is about 260, representing only 5.8% degradation in Q-factor as compared to the conventional waveguide although it operates at much higher frequency. Notably, a conventional rectangular waveguide with the same cutoff frequency using the same dielectric material and thickness as the SRW would have, the lateral dimension of 19.9 mm against 7.0 mm in the SRW design. If the conventional rectangular waveguide has slow-wave factor of $\sqrt{\varepsilon_r}$, approaching the theoretical limit, immediately produces an estimated area reduction of 6.7 (85%) (at 5.78 GHz) using the particular SRW design. The results clearly demonstrate that the proposed SRW is ideal for miniaturized microwave integrated circuit (MIC) design, which requires a high-Q transmission line.

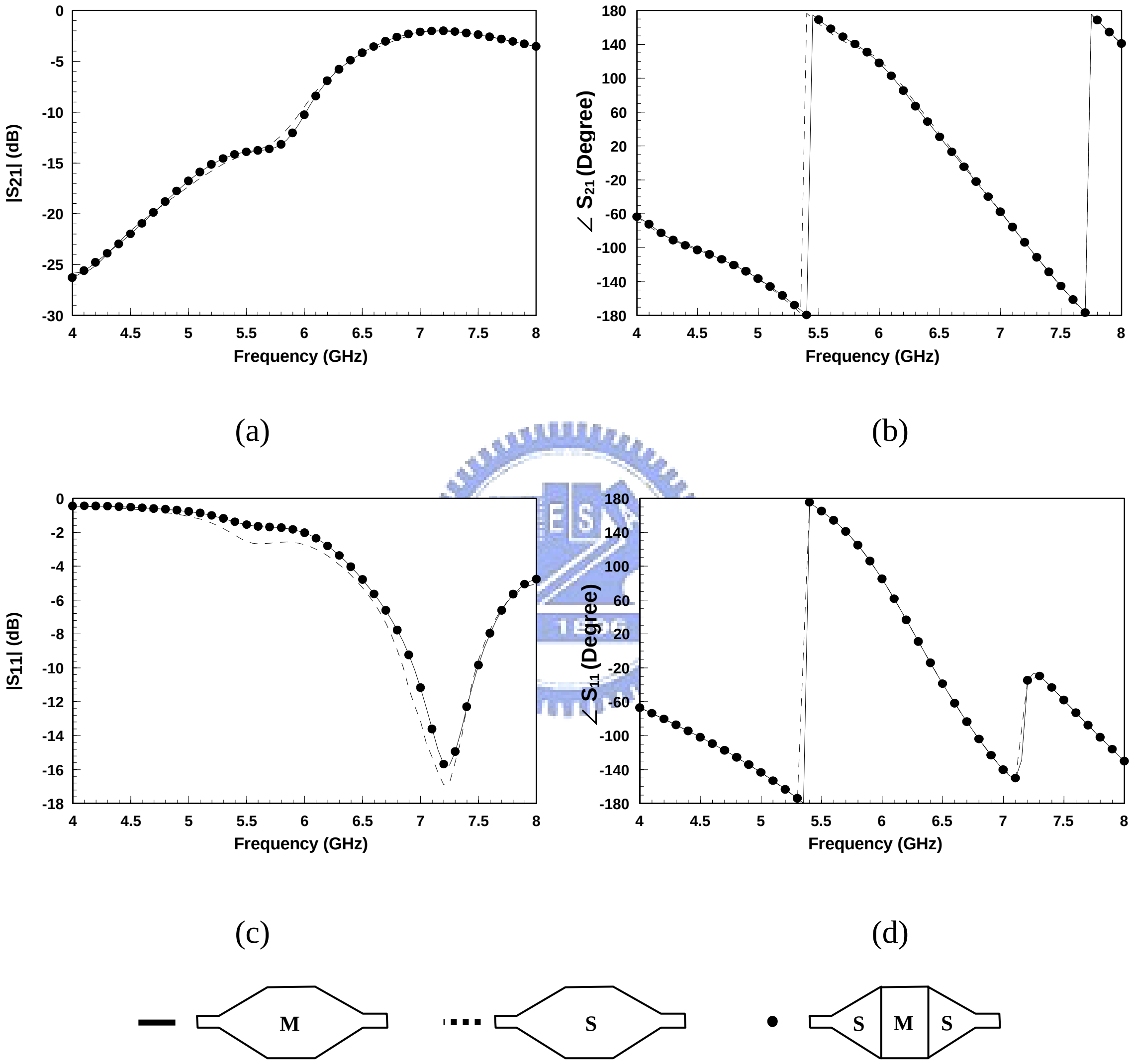

Fig. 2.9 Measured/Simulated two-port S-parameters of TE_{10} mode synthetic rectangular waveguide (SRW) parameters (a) $|S_{21}|$ (b) $\angle S_{21}$ (c) $|S_{11}|$ (d) $\angle S_{11}$

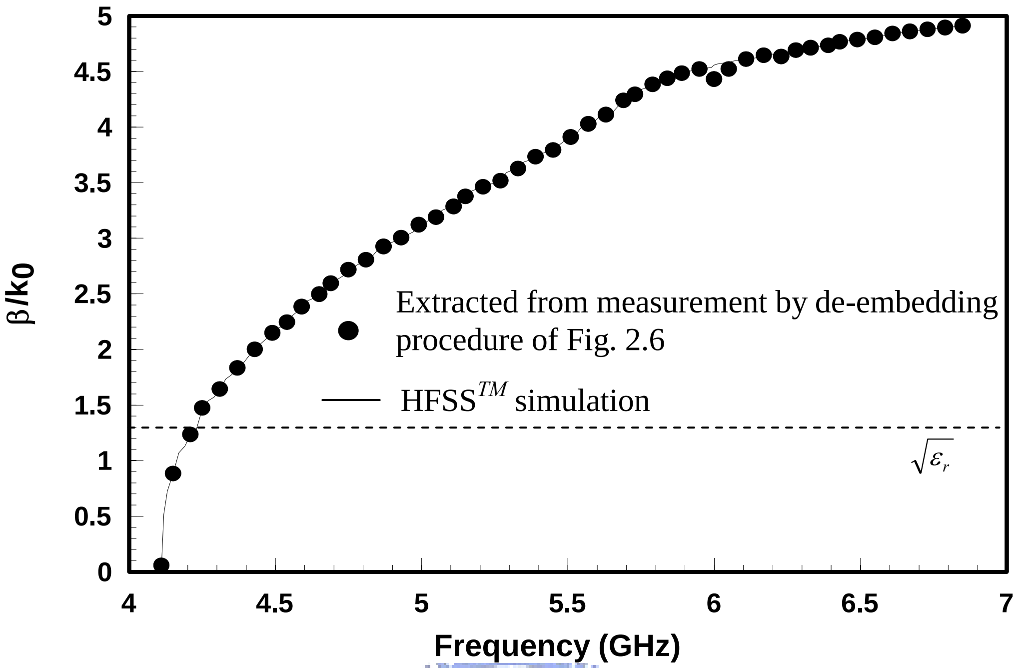

(a)

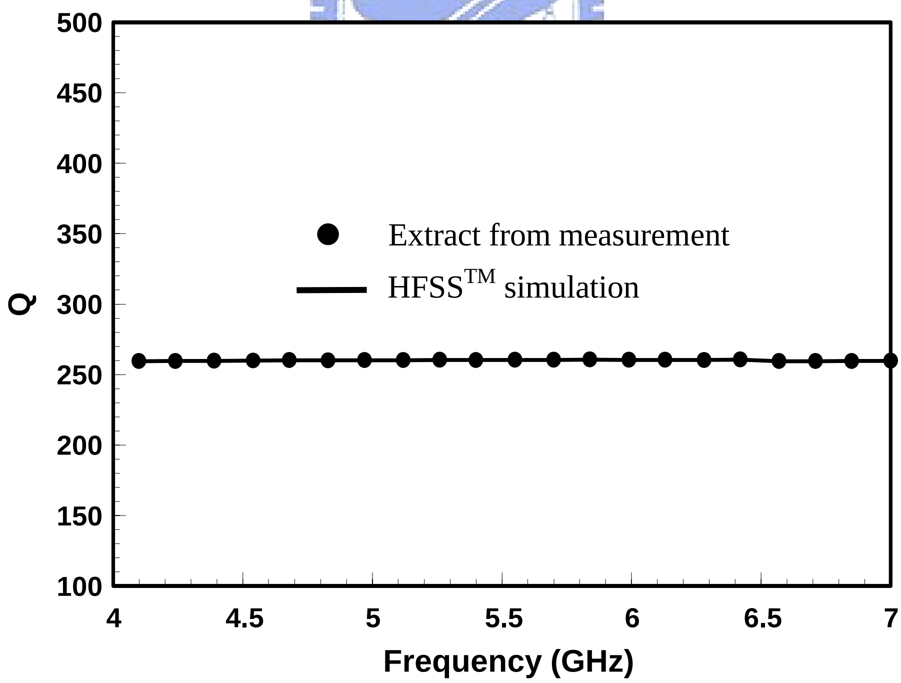

(b)

Fig. 2.10 Comparison of the extracted normalized phase constants of the TE_{10} mode SRW with those obtained by HFSS^{TM} simulation: (a) phase constant, (b) Q-factor.

In obtaining the complex propagation constant of the TE_{10} mode SRW using $HFSS^{TM}$ simulation, only three field components in the SRW were observed. Figures 2.11 (a), (b) and (c) plot the transverse E_y, transverse H_x, and longitudinal H_z field components at 6 GHz, respectively. The value E_y and H_x (Fig. 2.11 (a) and Fig. 2.11 (b)) approximately follow the sine distribution and H_z (Fig. 2.11 (c)) the cosine distribution. Such observations agree well with the field distributions of an ideal TE_{10} mode waveguide governed by (3), (4), and (5). Thus the results shown in Fig. 2.10 validate the propagation of the TE_{10} mode in the SRW as shown in Fig. 2.3.

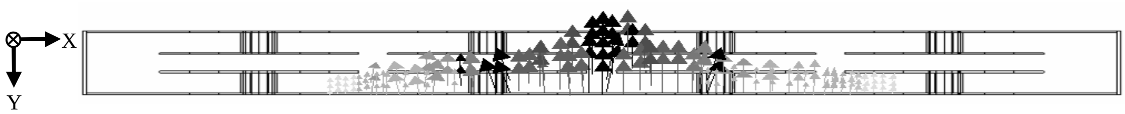

(a)

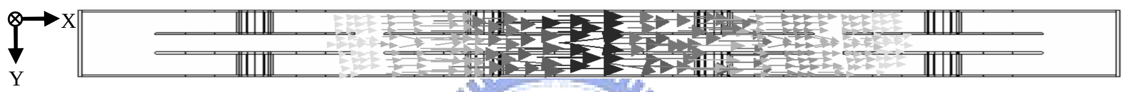

(b)

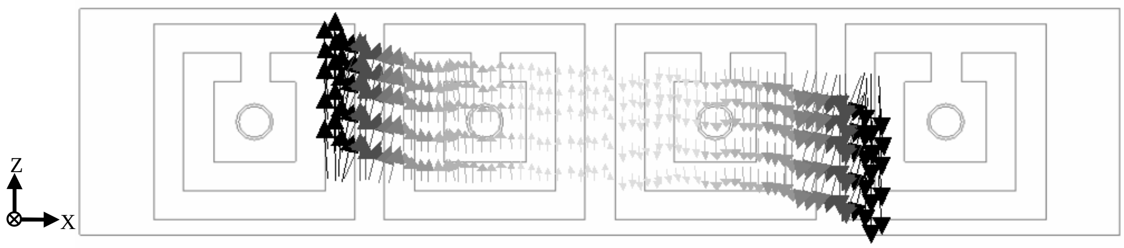

(c)

Fig. 2.11 Field distribution of the synthetic TE_{10} mode rectangular waveguide at 6.0 GHz (a) 2D E_y-field (b) 2D H_x-field (c) 2D H_z-field.

2.4 *TM_{00} and TM_{10} Mode Synthetic Rectangular Waveguides (SRW)*

The making of TM_{00} and TM_{10} synthetic rectangular waveguide (SRW) as illustrated in Figs. 2.4 and 2.5 is beyond our current capability. Thus two theoretical methods were applied to confirm that the TM_{00} mode and TM_{10} mode exist in the proposed SRW. These methods are the de-embedding procedure of Fig. 2.6, and finite element method (FEM) using HFSS^{TM}.

Figures 2.12 (a) and (b) investigate the through characteristics of the back-to-back connected SRW supporting TM_{00} and TM_{10} modes, respectively. The 3dB bandwidth is between 10.83 GHz and 11.8 GHz (11.1 GHz and 12.2 GHz) for the integrated TM_{00} mode (TM_{10} mode) SRW as shown in Figs. 2.4 and 2.5. Both transmission regions mentioned above, however, fall into the stopband region of Fig. 2.2, implying that the electromagnetic bandgap (EBG) surfaces behave like magnetic surfaces. Since the transmission losses are relatively high and the bandwidths are relatively narrow, the single-mode approximate de-embedding procedure may not be accurate. Nevertheless, the de-embedding method can generate an estimate of the SRW phase constant.

Figure 2.13 shows the superimposed plots of the normalized phase constants obtained by the de-embedding procedure and HFSS^{TM} simulation, respectively. The curves with solid and hollow square symbols represent the TM_{00} mode solutions obtained by de-embedding and HFSS^{TM}. Data below 10.4 GHz and above 12.3 GHz are not shown for the de-embedding case, since the de-embedding phase constant changed drastically. Between 10.8 GHz and 11.8 GHz, the de-embedding phase constant was about 6.2% lower than that obtained by HFSS^{TM}. It is interesting to notice that the de-embedded phase constant is very close to the HFSS^{TM} data between 10.5 GHz and 10.6 GHz.

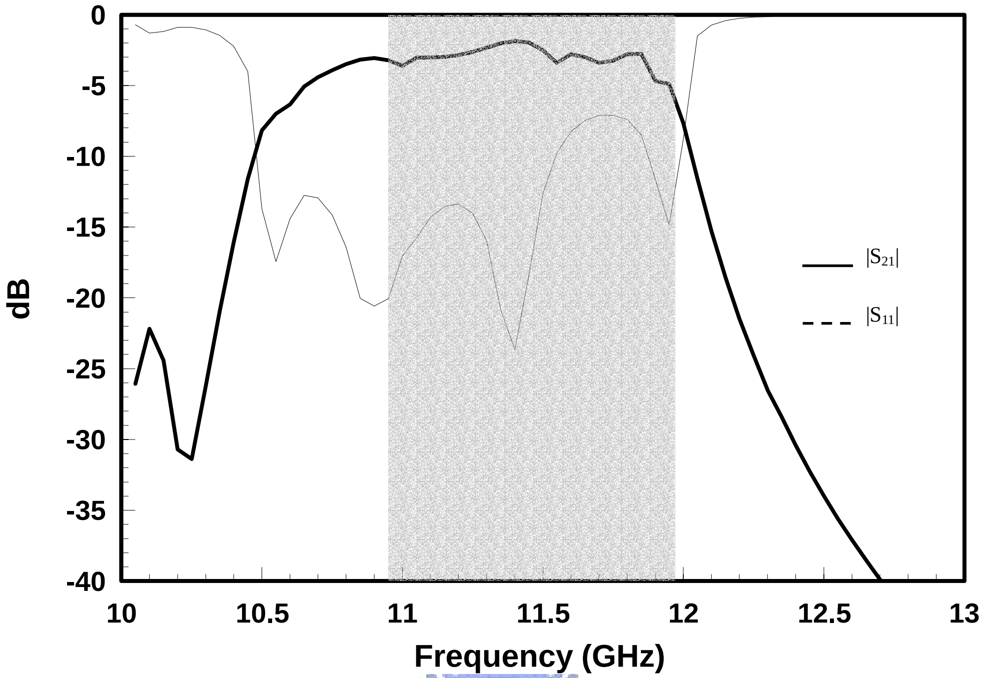

(a)

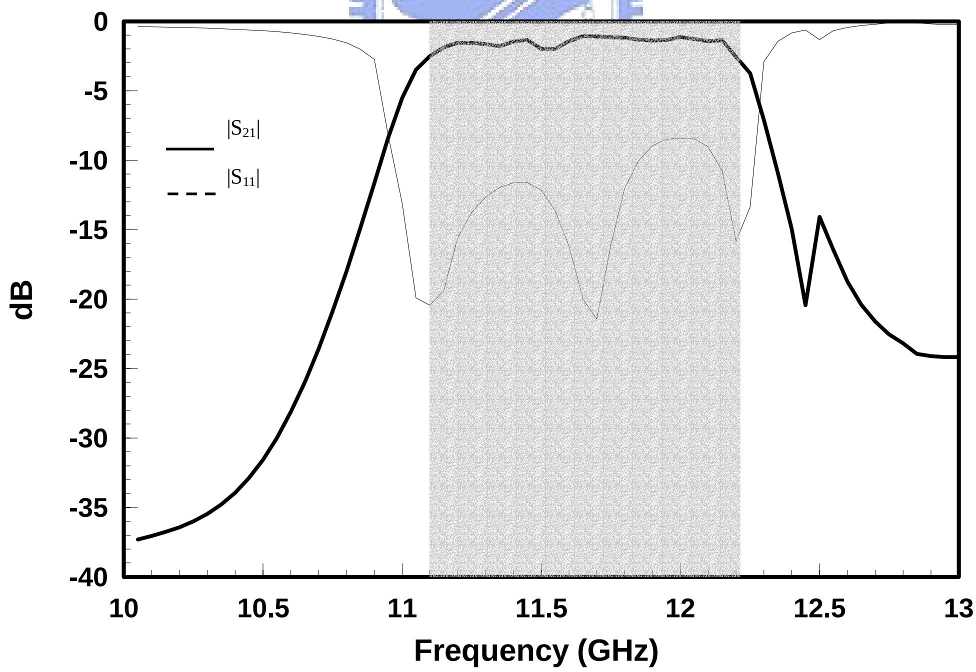

(b)

Fig. 2.12 Scattering analyses of the integrated SRW with various waveguide transitions (a) TM_{00} mode converter (b) TM_{10} mode converter.

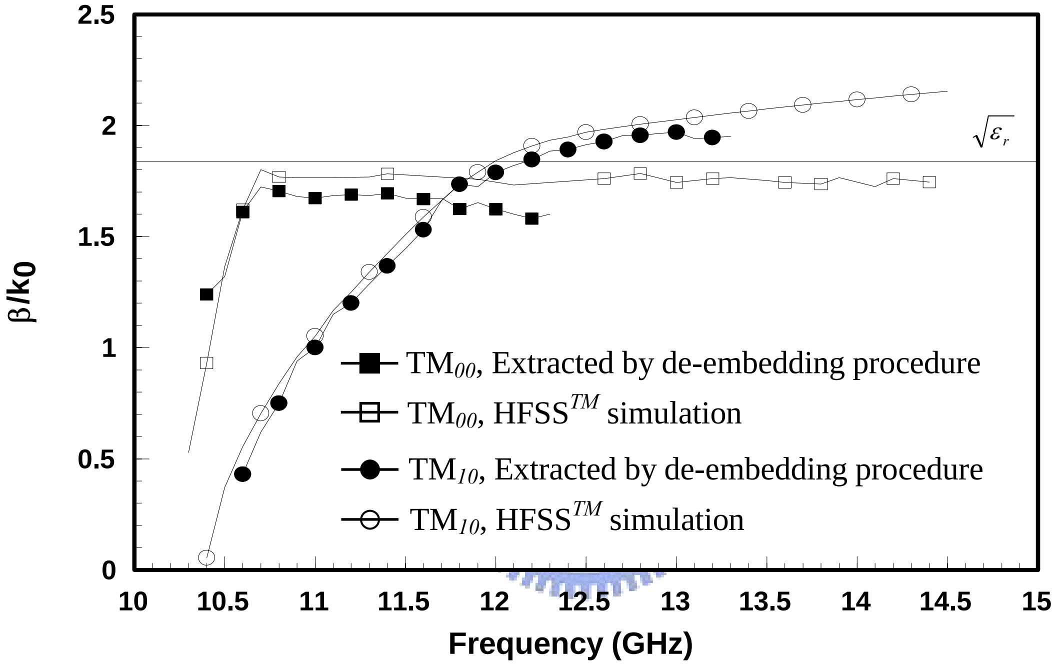

Fig. 2.13 Normalized phase constants of the proposed synthetic TM_{00} and TM_{10} mode rectangular waveguides.

The slow-wave factor of TM_{00} mode also rises sharply from the cutoff frequency near 10.2 GHz and approaches but never exceeds the theoretical limit $\sqrt{\varepsilon_r}$. After reaching $\sqrt{\varepsilon_r}$ at 10.6 GHz, the slow-wave factor flattens and approaches to 14.5 GHz, beyond which HFSS^{TM} fails to produce stable data. When preparing the TM_{00} mode data obtained by HFSS^{TM} up to 14.5 GHz, the modal field distributions were plotted and confirmed to be governed by (8), (9), and (10) for m=0. Figure 2.14 shows the field distribution at 11.0 GHz. Only two field components E_x and H_y, were observed, and field distributions, which exist only in region between two inner EBG surfaces, were keep uniform along the x-axis. Also, the transverse magnetic field (H_y) shown in Fig. 2.14 (b) was observed to be perpendicular to the EBG surfaces, and meanwhile the transverse electric field (E_x) as shown in Fig. 2.14 (a) is parallel to the EBG surfaces. Such observations, which reveal the field distributions of pseudo-TEM mode in the SRW, agree with the ideal TM_{00} waveguide model shown in Fig. 2.1(b), confirming that the EBG surfaces behave like the perfect magnetic conductor (PMC).

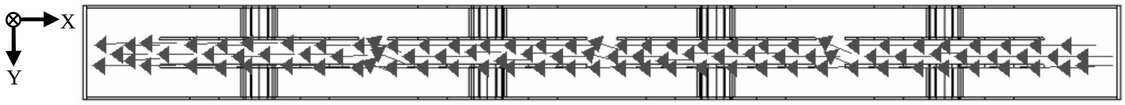

(a)

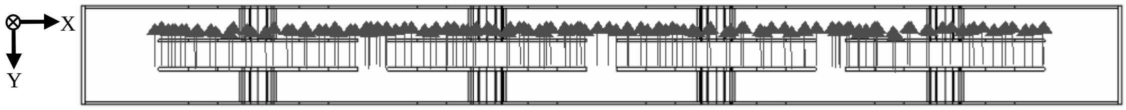

(b)

Fig. 2.14 Field distribution of the synthetic TM_{00} mode SRW at 11.0 GHz (a) 2D E_x-field (b) 2D H_y-field.

The same investigation and precautions were exercised when plotting the TM_{10} mode data. The curves with solid and hollow dots represent the TM_{10} mode solutions obtained by de-embedding and $HFSS^{TM}$, respectively. The de-embedding phase constant was about 4.3% lower than that obtained by the $HFSS^{TM}$ data between 10.5 GHz and 10.6 GHz. The slow-wave factor of TM_{10} mode approaches zero from the cutoff frequency near 10.4 GHz and exceeds the $\sqrt{\varepsilon_r}$ at 11.98 GHz. Then it levels off to 2.2 at 14.5 GHz. Figure 2.15 shows FEM modal field distribution at 11.4 GHz. Only three field components E_x, H_y and E_z were observed. Notably, Figs 2.15 (a) and (b) reveal that the transverse field components E_x and H_y follow $\cos(\pi x/a)$ distributions. In the longitudinal direction, only the E_z component exists, following $\sin(\pi x/a)$ distribution, thus verifying the TM_{10} mode solution.

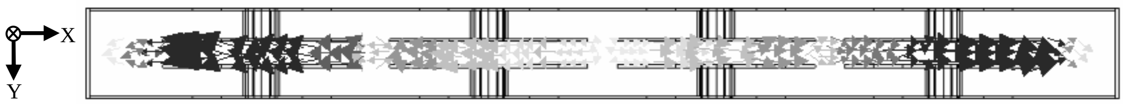

(a)

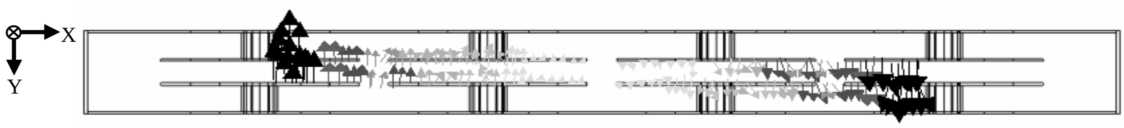

(b)

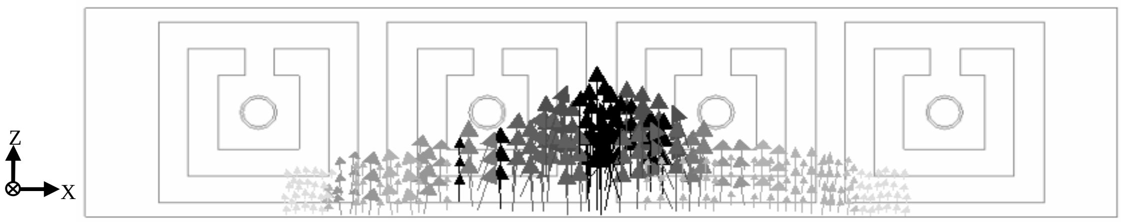

(c)

Fig. 2.15 Field distribution of the synthetic TM_{10} mode rectangular waveguide at 11.4 GHz (a) 2D E_x-field (b) 2D H_y-field (c) 2D E_z-field.

The extracted Q-factors of the TM_{00} and TM_{10} mode SRWs were evaluated using HFSS^{TM}. A series of numerical analyses were performed with different material constant values, including conductivity and loss tangent, to investigate the loss of SRW during the TM_{00} mode and TM_{10} mode operations. The Q-factor of the SRW without conductor loss and dielectric loss is about 664 (673) for TM_{00} mode (TM_{10} mode), yielding the intrinsic loss of the SRW. Additionally, Q-factors with either conductor loss or dielectric loss are approximately 548 and 199 for TM_{00} mode and 555 and 192 for TM_{10} mode, respectively. The total Q-factors of TM_{00} mode and TM_{10} mode are approximately 187 and 188, respectively. Notably, the total Q-factors of the TM_{00} mode and TM_{10} mode SRW are higher than that of a microstrip line on the same substrate, indicating that the synthetic integrated TM_{00} and TM_{10} mode waveguides have useful applications in microwave integrated circuit (MIC) and antenna designs.

Table 2.1 Theoretical Q-factor of the TM_{00} mode SRW at 11.0 GHz.

	$\tan\delta$	σ	Q-factor
1	0.0	PEC	673
2	0.0035	PEC	192
3	0.0	5.813×10^7	555
4	0.0035	5.813×10^7	188
σ: conductivity, $\tan\delta$: loss tangent			

Table 2.2 Theoretical Q-factor of the TM_{10} mode SRW at 11.4 GHz.

	tanδ	σ	Q-factor
1	0.0	PEC	673
2	0.0035	PEC	192
3	0.0	5.813×10^7	555
4	0.0035	5.813×10^7	188
σ: conductivity, tanδ: loss tangent			

2.5 *TE_{10} Mode Miniaturized Integrated Rectangular Waveguide Antenna*

The concept of synthetic rectangular waveguide (SRW) and its modal behaviors are reported in the previous sections. The two-dimensional (2D) photonic bandgap (PBG) arrays substitute both top and bottom metallic surfaces of the conventional rectangular waveguide. Each PBG cell is formed by two spiral coils, which are DC-connected by a through hole at center. When the TE_{10} mode propagates in the SRW, which supports the vertical transverse *E*-fields and horizontal *H*-fields, the modal fields are perturbed by the PBG arrays at the top and bottom surfaces of the SRW. Such perturbation results in the slow-wave effects, and consequently the SRW has much higher normalized phase constant and lower cutoff frequency than those of the conventional rectangular waveguide surrounded by the all-metallic walls [46], achieving miniaturizations. Figure 2.16 shows the proposed integrated rectangular waveguide antenna. The 2D PBG array is made on a two-sided printed FR4 circuit board of thickness (h_1,h_3) 0.2 mm and relative permittivity (ε_{r1},ε_{r3}) 4.1 to form the top and bottom surfaces of the SRW. The size of the PBG cell is 1.75 mm by 1.75 mm. Another FR4 dielectric substrate, forming a prepreg layer (ε_{r2}=4.1, h_2=0.5 mm), is sandwiched between the top and bottom PBG surfaces. The vertical walls of the SRW, as shown in part (b) of Fig. 2.16, are made by plated-through technology followed by thick copper plating of 35 μm to complete the SRW design.

The three-dimensional, finite element-based high-frequency structure simulator ($HFSS^{TM}$) is employed to analyze the dispersion characteristics of the SRW. In the numerical investigation, the PBG array comprises six unit cells in the transverse direction of the SRW. Similar PBG cell had been reported and used in designing the dual-band leaky-mode antenna and compact bandpass filter [47-48], indicating that the present PBG design shown in Fig. 2.1 (a) has stopband characteristics similar to those of 2D array of infinite number of cells. Fig. 2.17 shows the full-wave simulation result of the SRW based on TE_{10} mode. The cutoff frequency is almost 4.5 GHz, and the normalized slow-wave factor is about 2.5 at 6.76 GHz.

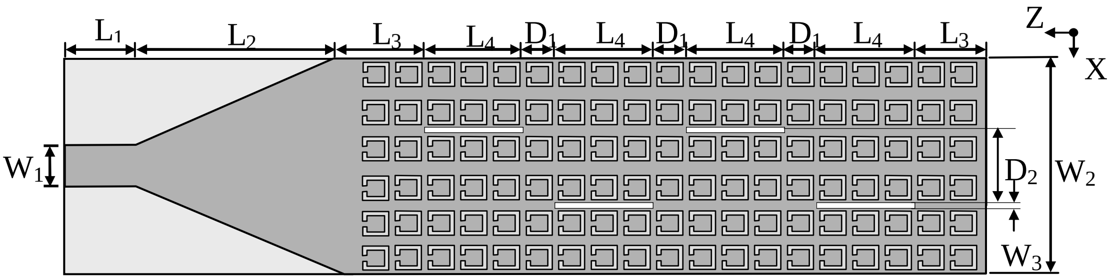

(a)

(b)

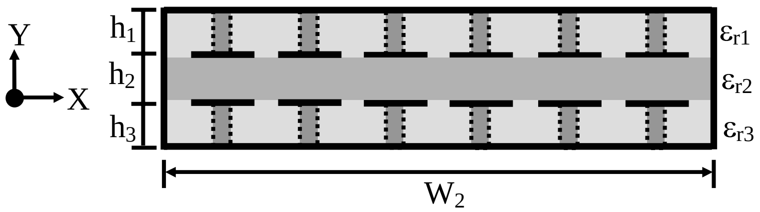

(c)

Fig. 2.16 Miniaturized synthetic rectangular waveguide (SRW) antenna (a) top-view. (b) side-view. (c) front-view.

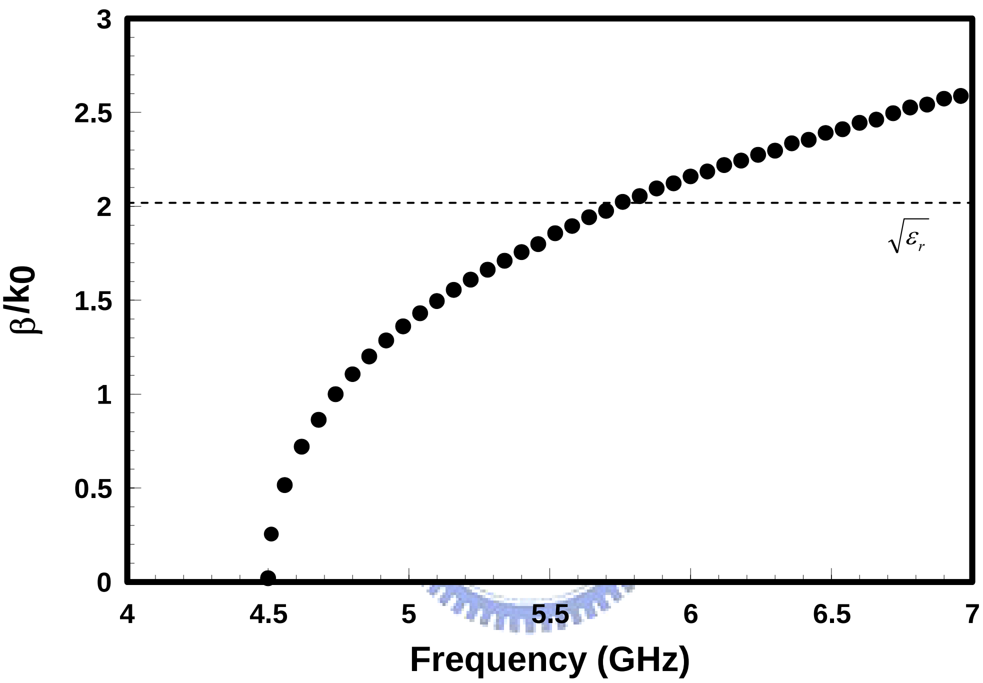

Fig. 2.17 Normalized phase constant of the proposed TE_{10} mode synthetic rectangular waveguide (SRW).

Additionally, the Table 2.3 lists the dimensions of various conventional all-metallic rectangular waveguide with different cutoff frequencies. The structural parameters are calculated using (2) based on the TE_{10} mode operation and the dielectric material with the permittivity as same as those filled in the proposed integrated rectangular waveguide antenna. A conventional metallic rectangular waveguide with cut-off frequency of 4.5 GHz is 16.45 mm wide and 8.225 mm height in the cross-section, against the 10.5 mm wide and 0.9 mm height of the proposed synthetic rectangular waveguide (SRW). On the other words, the proposed SRW can achieve least 60% size reduction for the rectangular waveguide design in two-dimensional directions.

On the other hand, the waveguide components need external waveguide transitions for connecting with other planar circuits or instruments. In present waveguide design, as shown in Fig. 2.16(a), the tapered microstrip, which can be integrated with SRW in the same polymer substrate, is adopted for the mode converter, transforming the microstrip-mode to the TE_{10} mode supported by the SRW [49-50].

Table 2.3 All-metallic rectangular waveguide with different cutoff frequencies

Cutoff Frequency	a (mm)	b (mm)
1.0 GHz	74.083	37.04
4.0 GHz	18.506	9.253
4.5 GHz	16.450	8.225
5.0 GHz	14.805	7.402

2.5.1 Radiation Characteristics of Miniaturized Synthetic Rectangular Waveguide (SRW) Antenna

The conventional all-metallic rectangular waveguide with slots in the waveguide walls, forming the so-called leaky-wave or slotted antenna, had been widely applied in phase array or detective radar applications. The slots on the top metal wall of the rectangular waveguide can leak energy naturally. A. A. Oliner showed that the radiation characteristics associated with the slotted leaky-wave rectangular waveguide antenna are functions of physical parameters, which included length (L_4), width (W_3), spacing (D_1, D_2), orientations, and number of slots on the waveguide [51]. Consequently the slotted synthetic rectangular waveguide (SRW), differing from the planar antenna operated at fundamental or higher orders, provides more degrees of freedom for designing high-performance antenna.

Fig. 2.18 shows the photograph of the miniaturized SRW antenna. The antenna size is 71.0 mm by 10.5 mm (W_2), containing 39 X 6 photonic bandgap (PBG) cells. The length of the integrated mode converter is 12.0 mm (L_1= 3.0 mm, L_2= 9.0 mm) and the width is 1.0 mm (W_1). The 4 slots are in the top wall of the SRW. The size of each slot is 7.0 mm (L_4) by 0.4 mm (W_3). The distances between each slot are 3.0 mm (D_1) and 5.0 mm (D_2), respectively. The shorting plane is added at 11.0 mm (L_3) distances from the slot as the termination for the SRW antenna. The input reflection coefficient of the waveguide antenna was measured by the HP8510C^{TM} vector network analyzer (VNA) using the one-port SOL (short-open-load) calibration procedure.

During the measurements, the commercial microwave-grade 3.5-mm SMA connector facilitated the coaxial-to-microstrip interface for connecting the vector network analyzer (VNA) and the antenna under test. Fig. 2.19 shows the measured results of the synthetic rectangular waveguide (SRW) antenna including connector and transitions effects based on 50Ω systems. Between 4.78 GHz and 5.65 GHz, the reflection coefficient is kept below 10dB, revealing that the wave propagate into the antenna with low reflections. Fig. 2.20 shows the far-field radiation patterns of the proposed synthetic rectangular waveguide antenna at 5.25 GHz.

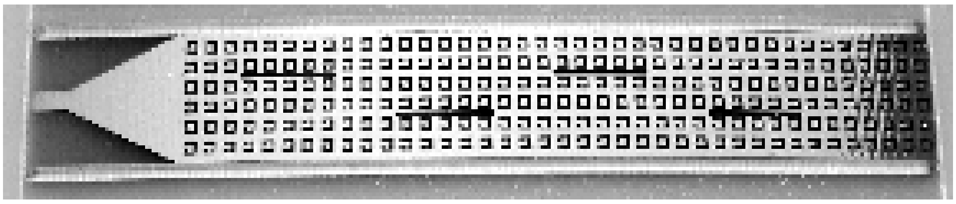

(a)

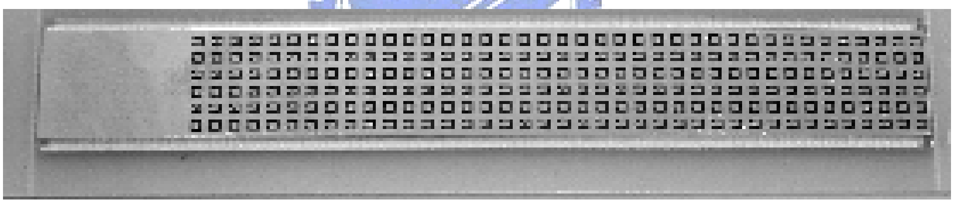

(b)

Fig. 2.18 Photograph of the miniaturized synthetic rectangular waveguide (SRW) antenna. (a) top-view. (b) bottom-view.

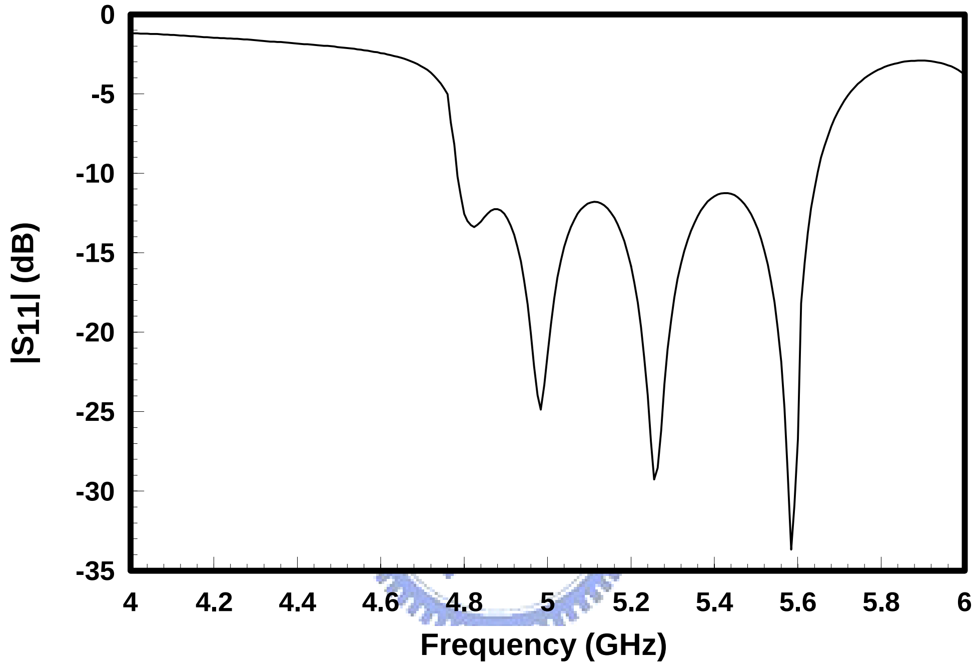

Fig. 2.19 The measured result of the input reflection coefficient for the miniaturized synthetic rectangular waveguide (SRW) antenna.

Before commencing the measurements for the radiation patterns of the SRW antenna, the test system was calibrated by two identical standard gain horns. Part (a) and part (b) of Fig. 2.20 show the co-polarization and cross-polarization of the proposed SRW antenna, respectively. The test system defines that the elevation angle is zero degree measured from the board-side of the antenna under test. The main lobe of the antenna appeared at 9.5^{o} from the broadside with gain of 4.28dBi, and 3dB beamwidth is 130^{o} at ϕ-direction (-65^{o} – 65^{o}). The gain-difference between the co-polarization and cross-polarization is more than 20dB, showing the polarization of the SRW antenna is linear. It should be noticed that the radiation pattern of the proposed miniaturized SRW antenna is near omnidirectional, showing the potential for designing roof-mount wireless communication devices.

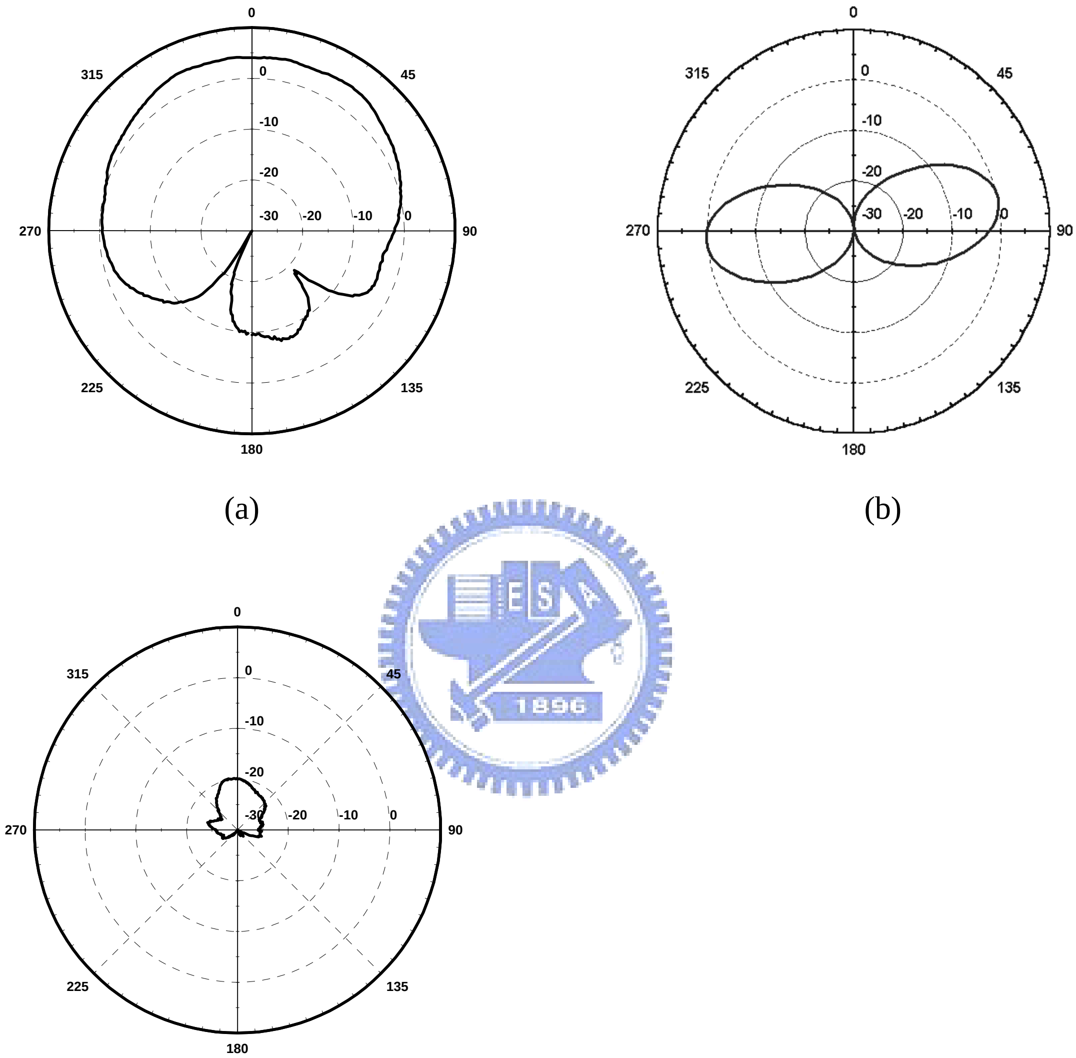

(a)

(b)

(c)

Fig. 2.20 Far-field radiation patterns of the proposed synthetic rectangular waveguide antenna at 5.25GHz: (a) E-plane, (b) H-plane, (c) cross-polarization.

CHAPTER 3
Multi-layer Synthetic Quasi-TEM Transmission Line

Chapter 3 presents the second kind of synthetic waveguide, named multi-layered complementary conducting strips (CCS) transmission line (TL). In the multi-layered CCS TL, two CCS signal layers are realized in a stack substrate system and signal layers are separated by a meshed ground plane. The guiding characteristics of the multi-layered CCS TLs, and the coupling effect between different signal layers are reported in Section 3.1. Furthermore, the proposed multi-layered CCS TLs is applied to design a transmission-line (TL)-based bandpass filter (BPF). Section 3.2 briefly reviews the design procedures of the transmission-line based bandpass filter, and Section 3.3 presents a way to map such an idealized BPF reported in Section 3.2 to the prototype made of the multi-layered synthetic CCS TLs introduced in Section 3.1. Excellent agreement between the experimental and theoretical filter frequency responses, shows a 2.46 dB insertion loss, a -16.8 dB return loss with less than 5% offset of low-side transmission zeros, and a 2% offset of center frequency. Finally, Section 3.4 presents a quick estimate of the proposed miniaturized filter design based on multi-layered CCS TL shows that the particular filter prototype approaches to the process limit.

3.1 *Multi-layered Complementary Conducting Strip Transmission Line (CCS TL)*

Recently, a new artificially engineered synthetic transmission line – the so-called complementary conducting strip transmission line (CCS TL) – was reported to be an effective means of miniaturizing microwave circuits [52]. The CCS TL has the following characteristics. It firstly provides wide design choices for making characteristic impedance of the transmission line, without changing the process parameters and material constants. Second, the meandered CCS TL exhibits less bending and adjacent coupling effects, as indicated by the slower change in characteristic impedance against the width variation in the TL than the conventional meandered microstrip used in the same fashion (See Fig. 5 in [52]). Therefore, a compact microwave circuit can be established using the meandered CCS TL, finally achieving miniaturization.

The CCS TL is made from a unit cell, which has dimensions that are much smaller than the operating wavelength. As shown in Fig. 3.1, a unit cell contains a mesh ground plane and a central patch with at least two series arms for cells in series (Fig. 3.1 (a)) and bent (Fig. 3.1 (b)) connection to the adjacent cells. The etched portion of the meshed ground plane complements to the central patch of the signal layer, forming a CCS TL.

Additionally, Fig. 3.2 shows a new multi-layer complementary conducting strips (CCS) transmission line (TL) configuration made of the meandered CCS TL realized by two metal-layers (Fig. 3.2 (a)), whose guiding characteristics have been well documented [52], and will not be repeated here.

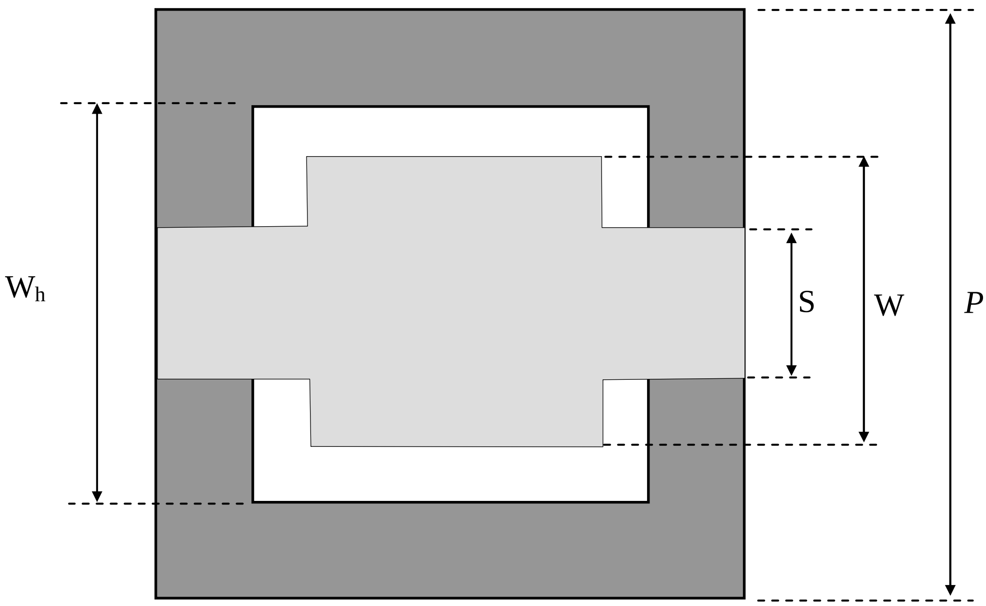

(a)

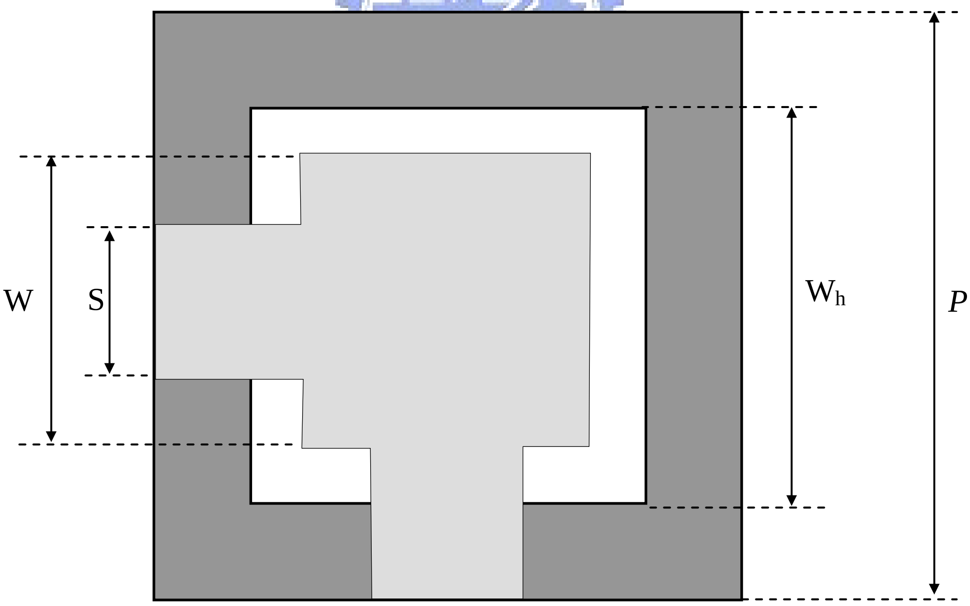

(b)

Fig. 3.1 Unit cells of complementary conducting strip transmission line (CCS TL): (a) For series connection. (b) For bent connection.

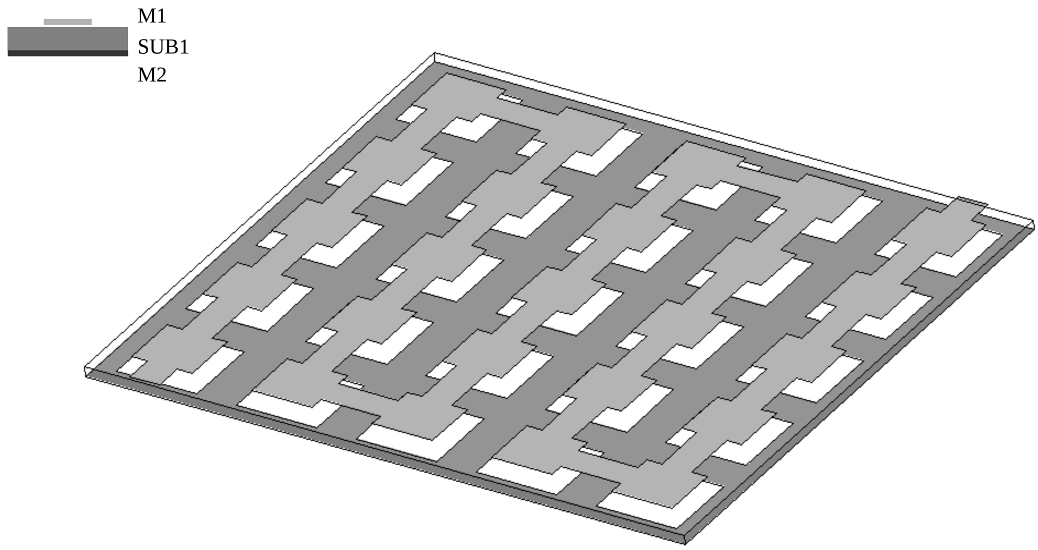

(a)

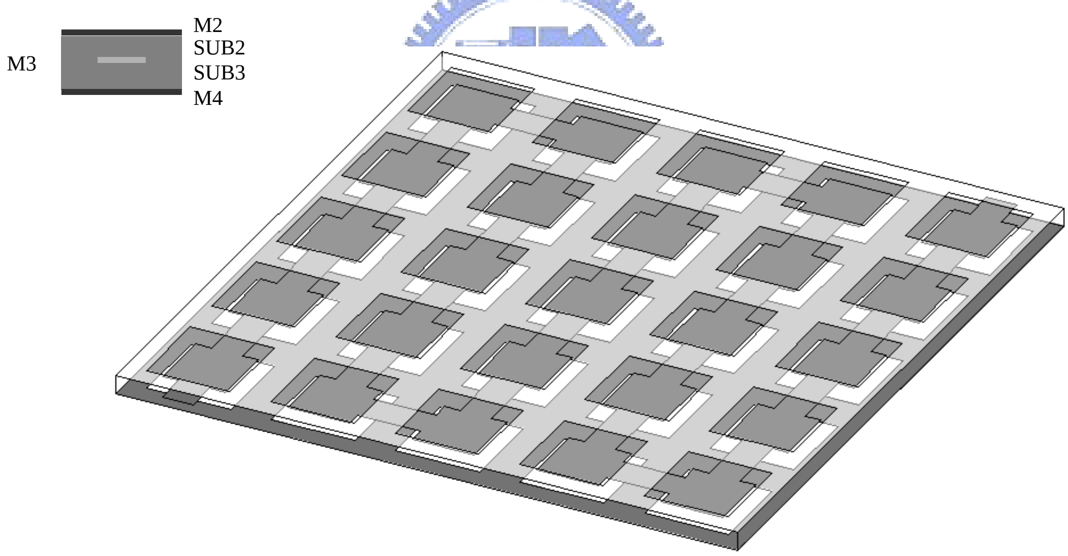

(b)

Fig. 3.2 Synthetic complementary conducting strip transmission line (CCS TL): (a) Meandered CCS TL. (b) Sandwiched meandered CCS TL.

On the other hand, the sandwiched CCS TL, which is realized by two meshed ground planes on the top and bottom surfaces (Fig. 3.2 (b)), is first time reported. All the meshed ground planes are connected by plated through-vias. The procedure for designing sandwiched CCS TL is similar to the meandered CCS TL reported in [52]. By applying various structural parameters, including period of CCS unit cell (*P*), the width of the central path (W), the width of the connecting arm (S), and the etch area of the mesh ground plane (W_h X W_h), the sandwiched CCS TL also provides wide design choices for making characteristic impedance of the transmission line, without changing the process parameters and material constants. Fig. 3.3 shows experimental results for comparing the guiding characteristics between the sandwiched CCS TL and conventional stripline in the identical laminated substrates. Clearly, the sandwiched CCS TL can provide wider impedance range than conventional meander CCS TL based on the same width of the signal line. Further more, the variation of propagation constant of the meandered CCS TL by changing the width of the signal is relatively smaller than that of the conventional meandered stripline. Notably, the slow-wave factor of the sandwiched CCS TL in the meander form is 2.188, exceeding the physical limit of the conventional stripline about 8%, revealing the potential of CCS TL for miniaturizing the planar circuits.

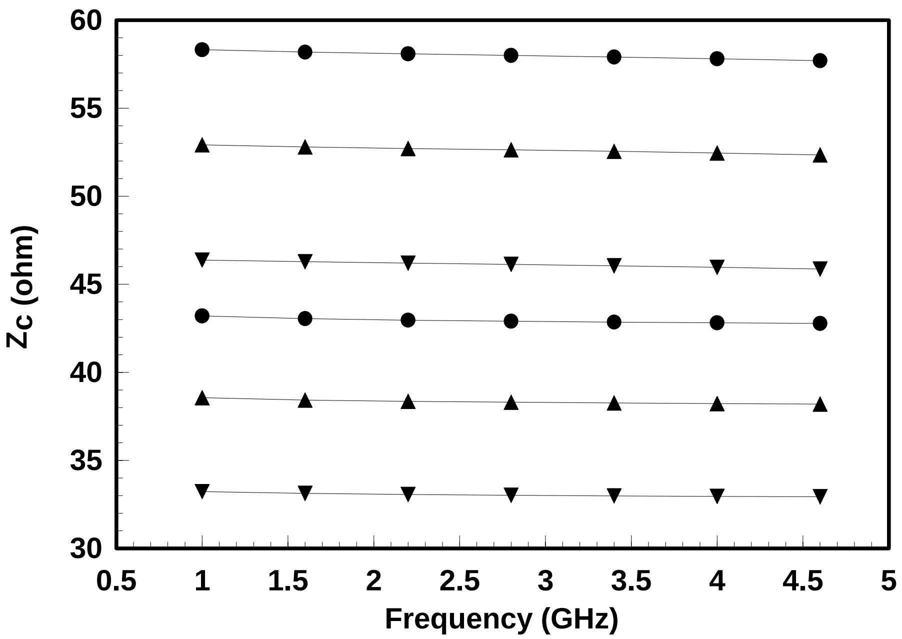

(a)

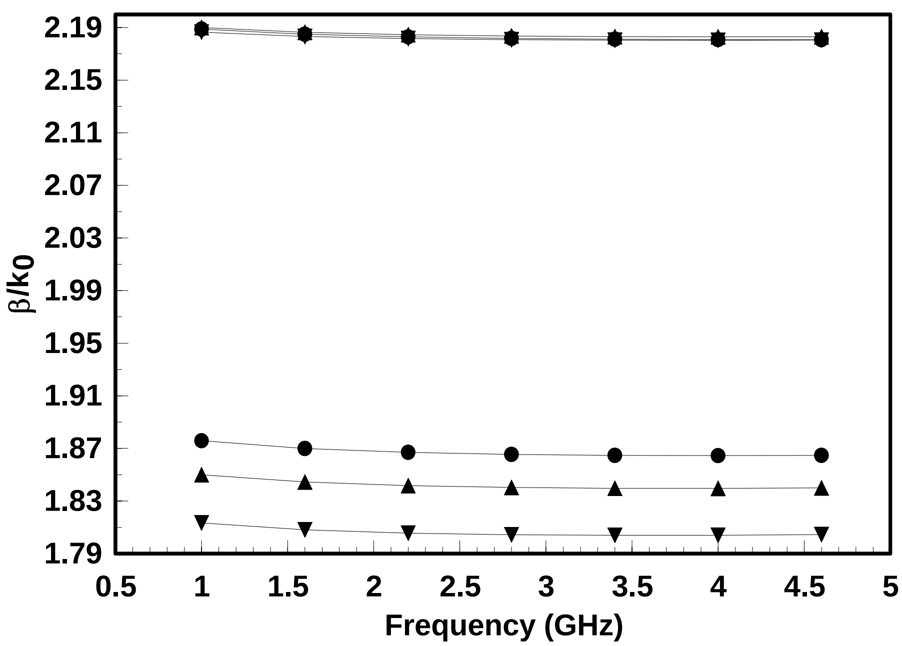

(b)

Fig. 3.3 The guiding characteristics of the sandwiched CCS TL and the conventional stripline: (a) real part of characteristic impedances, (b) normalized phase constants.

Notably, a four-layer substrate configuration was adopted throughout this chapter. In such a configuration, Figs. 3.2 (a) and 3.2 (b) share a common meshed ground plane M2. Based on this integration scheme, the CCS TLs in different layers can be independently controlled for various circuit designs. However, attention must be paid to the isolation of the stacked CCS TLs in different layers. The perfect solid ground plane provides the highest shielding capability of any mesh ground plane. An investigation on the shielding capability of two isolated circuits using meandered CCS TLs in different layers follows.

Two filters with independent functions are designed using CCS TLs and integrated in the same four-layer substrate configuration. The first is the lowpass filter (LPF), which occupies M1 and M2 layers (Fig. 3.2 (a)). The second is the bandpass filter (BPF), which utilizes the M2, M3 and M4 layers (Fig. 3.2 (b)). These symmetrical filters are designed following the similar procedure to be reported in the next section. In Fig. 3.2, every substrate has an equal thickness of 0.06 mm (SUB1-through-SUB3). The area of overlapping of the two filters is approximately 95 % of the total area. Figures 3.4 (a) and (b) show the intrinsic frequency responses of two stand-alone filters based on the measured and simulated results.

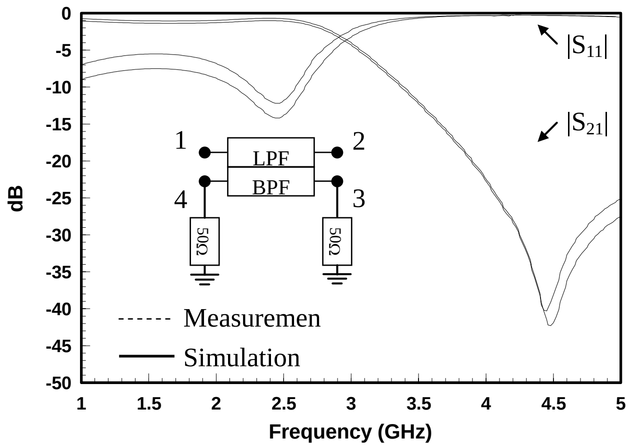

(a)

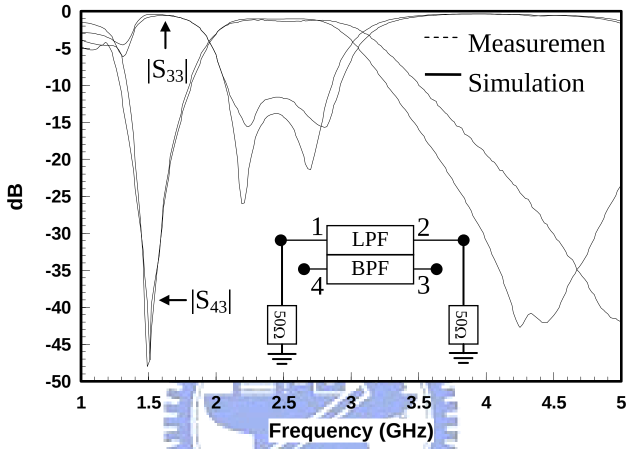

(b)

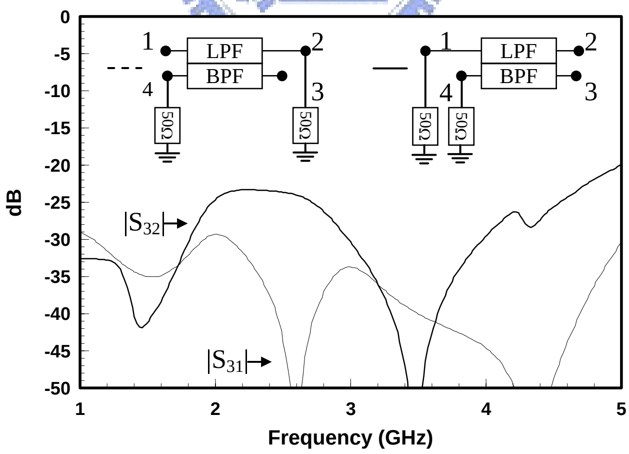

(c)

Fig. 3.4 Multi-function module incorporating four-layer meandered CCS TLs. (a) Frequency responses of 2.4 GHz LPF in M1 and M2 metal-layers. (b) Frequency responses of 2.4 GHz BPF in M2, M3 and M4 metal-layers. (c) Measured transmission coefficient between LPF and BPF in four-layer CCS TLs configuration.

In the experiments, one filter is measured using the two-port vector network analyzer (VNA) and the other is terminated by two chip 50Ω resistors. The full-wave simulations using Zeland™ IE3D follows the same procedure. The cutoff frequency of the LPF is 2.75 GHz, and the out-band rejection is below 30 dB from 4.25 GHz to 4.7 GHz. The insertion-loss is approximately 0.92 dB, a little higher than the simulated value of 0.45 dB. The return-loss is below –10 dB from 2.38 GHz to 2.51 GHz. On the other hand, in Fig. 3.4 (b) the center frequency of the BPF is 2.51 GHz, and the return-loss is below –11.5 dB from 2.11 GHz to 2.91 GHz. The measured insertion-loss is about 1.48 dB, which is 0.39 dB higher than the simulated value. Good agreement between the measurements and simulations for the two filters, show that the structural parameters and material constants are very close to the design values, as will be reported in the next section. Additionally, the transmission between port 3 and either port 1 or 2 is measured to evaluate the cross coupling between LPF and BPF. Figure 3.4 (c) shows the measured transmission coefficient across two filters. Based on the measured results presented in Figs. 3.4 (a) and (b), the BPF passes the energy above 2.11 GHz with low reflection and the LPF rejects signals above 2.75 GHz. The electromagnetic energy can be distributed in a four-layer configuration between 2.11 GHz and 2.75 GHz. Figure 3.4 (c) plots the measurements for the adjacent-port coupling ($|S_{32}|$) and cross-port coupling ($|S_{31}|$). The filter is symmetrical, so only port 3 is applied when port 4 is terminated. Although Fig. 3.4 (c) reveals the relatively high electromagnetic energy transmission between the two filters in different layers from 2.11 GHz to 2.75 GHz, the adjacent-coupling is maintained below -23 dB and the cross coupling is below -29 dB. Therefore, Fig. 3.4 (c) verifies that passive circuits in different layers of the stacked meandered CCS TLs can be well isolated from each other. In the case study, an isolation of more than 23 dB is achieved.

3.2 *Experimental Filter Design Procedure*

3.2.1 Transmission Line Filter: General Description

The filter in Fig. 3.5 (a), which uses open-circuited $\lambda_g/2$ stubs spaced $\lambda_g/4$ apart, is the origin of the transmission line filters presented herein (Sec. 10.04 of [53]). λ_g is the guiding wavelength of the center frequency f_0 in the passband. The computed response of a 13% bandwidth bandpass filter (BPF) with equal-ripple of 0.05dB is plotted in Fig. 3.5 (b). The filter is simulated by the ideal transmission line models without junction effects, and the numerical results are calculated based on the two-port 50 Ω system. In the sense, all the shunt stubs with the same characteristic impedance act the short circuit, forming the transmission zeros at the frequencies of $Nf_0/2$ where the N is the odd integers. Therefore, the passband can be constructed at the frequencies of the Nf_0 periodically.

More generally, the un-limited transmission zeros may be put in the desired frequency points through adding the shunt quarter-wavelength stubs in the BPF. The filter in Fig. 3.6 (a) demonstrates this concept. Eight shunt stubs with electric lengths of $\lambda_g/4$ in the 1.78, 1.88, 3.19 and 3.95 GHz are added. The shunt stubs at each cross-junction are identical, and both act the inductive or capacitive load in the passband. Each series transmission line, connecting two pairs of open stubs, forms the parallel resonator, and the coupling coefficient between two adjacent resonators depends on the slop parameters of two resonators. On the other words, 2N open stubs construct N-1 order BPF with N pre-selective transmission zeros simultaneously. The filter shown in Fig. 3.6 (a) was designed following the same passband characteristics and numerical results are plotted in the Fig. 3.6 (b) based on the 50Ω system. Although the impedance range shown in Fig. 3.6 is too wide to be realized using typical planar transmission line, the frequency responses shown in Fig. 3.6 (b) reveal wideband rejection, keeping -35 dB below from 3 GHz to 5.5 GHz.

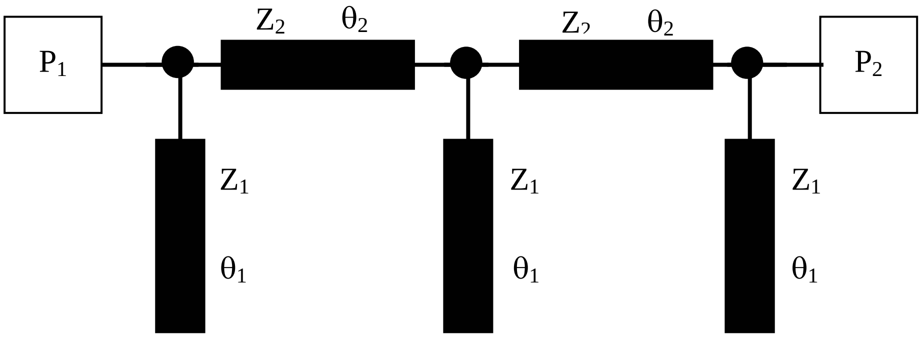

Z_1=14.3Ω, θ_1=180° @ 2.5 GHz Z_2=53.3Ω, θ_2=90° @ 2.5 GHz

(a)

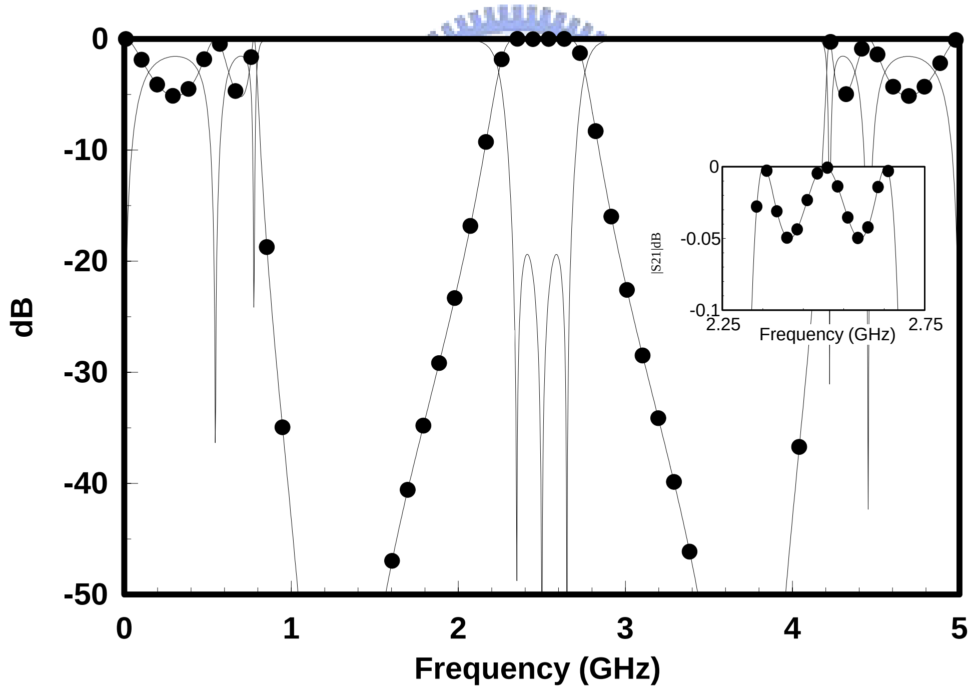

(b)

Fig. 3.5 Transmission-line TL bandpass filter (BPF) with identical shunt stubs: (a) equivalent circuit model, (b) simulated frequency responses.

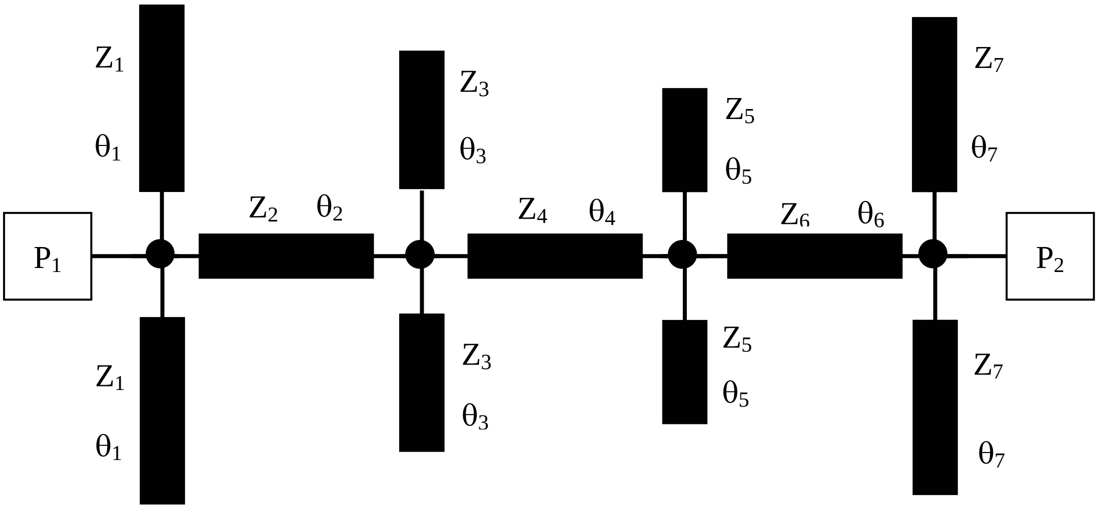

Z_1=104.79Ω, θ_1=90° @ 1.78 GHz Z_2=60.92Ω, θ_2=156.436° @ 2.5 GHz

Z_3=38.61Ω, θ_3=90° @ 3.19 GHz Z_4=60.41Ω, θ_4=10.904° @ 2.5 GHz

Z_5=20.06Ω, θ_5=90° @ 3.95 GHz Z_6=61.32Ω, θ_6=158.766° @ 2.5 GHz

Z_7=138.35Ω, θ_7=90° @ 1.88 GHz

(a)

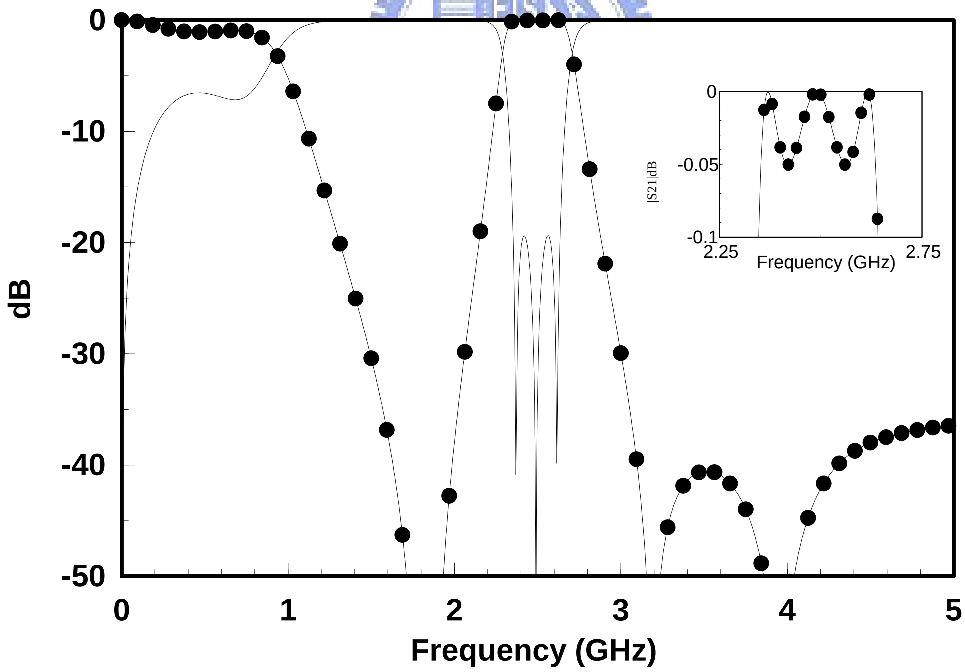

(b)

Fig. 3.6 Transmission-line TL bandpass filter (BPF) with un-symmetrical shunt stubs: (a) equivalent circuit model, (b) simulated frequency responses.

Recently, Quendo *et al.* reported that a transmission-line bandpass filter (BPF), incorporating the so-called dual behavior resonator (DBR), could achieve a Nth-order BPF with 2N pre-selective transmission zeros using 2N open and/or short stubs [54-56]. One DBR, which contains two open/short stubs of different lengths and characteristic impedances, independently controls two transmission zeros. Such filters design and architecture have been well documented [54-56]. The similar filter architecture is applied to demonstrate the filter miniaturization incorporating meandered stacked CCS TLs. However, proposes a larger Nth-order TL BPF with only 2(N-1) pre-selective transmission zeros using 2N open stubs, by adding an additional pair of shunt stubs and a TL connected in series to achieve a symmetrical BPF design with a direct interface to external 50Ω loads. Following the procedures reported in the next section, Fig. 3.7 presents a practical example of a third-order BPF with detailed design parameters. The circuit is also simulated using the ideal transmission line model, neglecting junction effects. Figure 3.7 (b) plots the corresponding frequency responses based on 50Ω reference impedance. Four transmission zeros are set at 1.78, 1.88, 3.19 and 3.95 GHz, forming a passband with a center frequency (f_0) at 2.5 GHz. Therefore, the out-band rejection can be below 35dB from 3.1 GHz to 4.15 GHz. The return-loss is below -19.429 dB from 2.329 GHz to 2.671 GHz, achieving a passband with an equal ripple of 0.05 dB. Notably, the BPF shown in Fig. 3.7 is symmetrical and directly matches the 50Ω system without further impedance transformation.

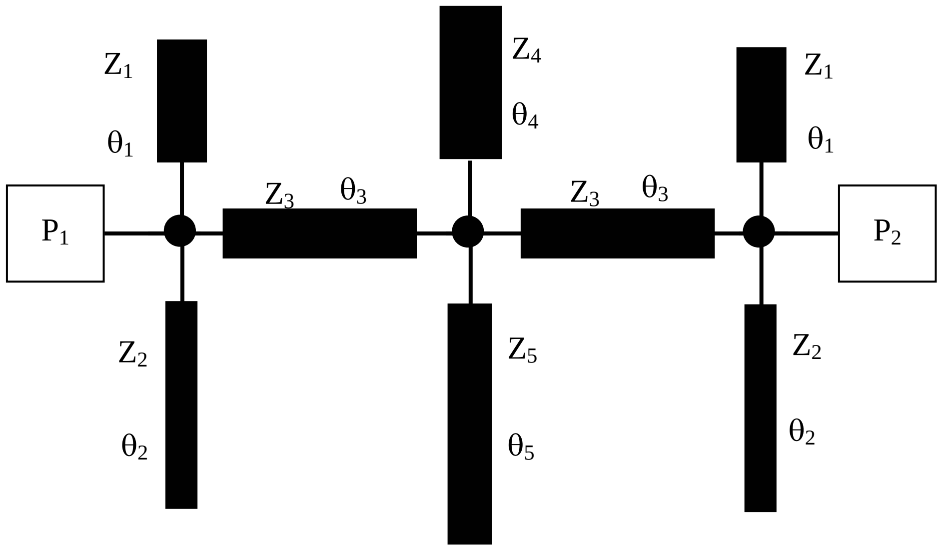

Z_1=41.03Ω, θ_1=90° @ 3.95 GHz　　Z_2=60.88Ω, θ_2=90° @ 1.88 GHz

Z_3=48.67Ω, θ_3=64.428° @ 2.5 GHz　　Z_4=56.85Ω, θ_4=90° @ 3.19 GHz

Z_5=40.34Ω, θ_5=90° @ 1.78 GHz

(a)

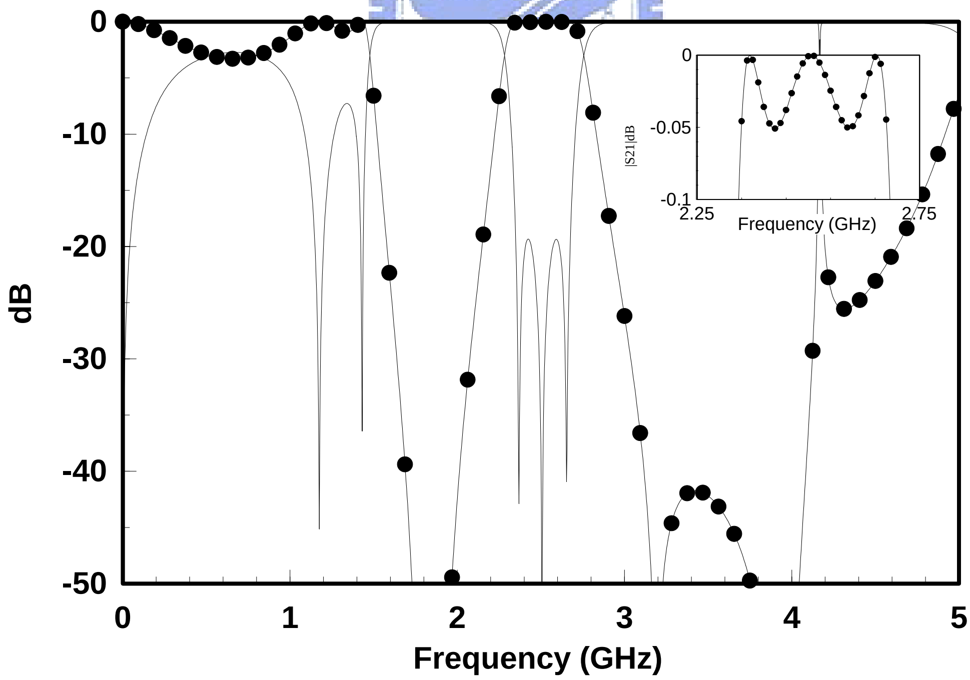

(b)

Fig. 3.7 Transmission-line TL bandpass filter (BPF) with symmetrical shunt stubs: (a) equivalent circuit model, (b) simulated frequency responses.

3.2.2 Design Procedure of Transmission Line Bandpass Filter

The TL BPF design begins with the design of parallel resonators. Figure 3.8 shows the equivalent circuit of the parallel resonator in both lumped (Fig. 3.8 (a)) and distributed (Fig. 3.8 (b)) forms. Z_c and Z_L represent the characteristic impedances of the two transmission lines. F_c and F_L are the quarter-wavelength frequencies of the transmission lines. Assuming that the transmission lines are lossless, the input susceptance of the resonator is given by the following equation.

$$B_{res} = j[Y_c \tan(\theta_c) + Y_L \tan(\theta_L)] \quad (1)$$

Variables θ_c and θ_L are the electric lengths of the two transmission lines at the center frequency (f_0) of the BPF. Y_c and Y_L represent the inverse of the characteristic impedances of the two TLs. If F_L is defined below the f_0 , then F_c must be above f_0. The susceptances of the open stub that is one quarter wavelength frequency below (above) f_0 is negative (positive) near f_0 , as shown in Fig. 3.9. The sum of the two curves indicates a parallel resonance at f_0. Therefore, Z_c, Z_L, F_c and F_L can be chosen to make the input susceptances of the parallel resonator zero at the f_0 of the BPF.

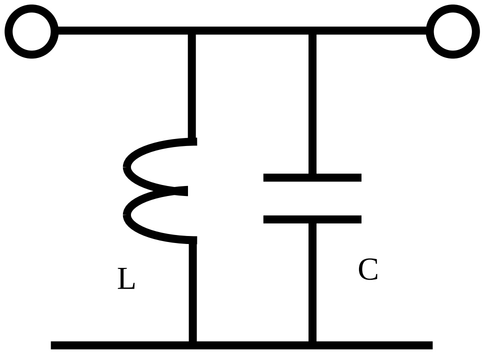

(a)

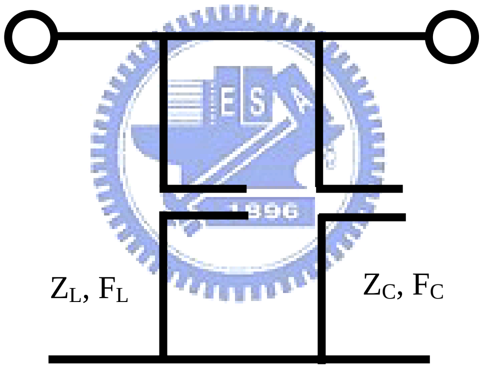

(b)

Fig. 3.8 Parallel resonators: (a) Lumped realization (b) Distributed realization.

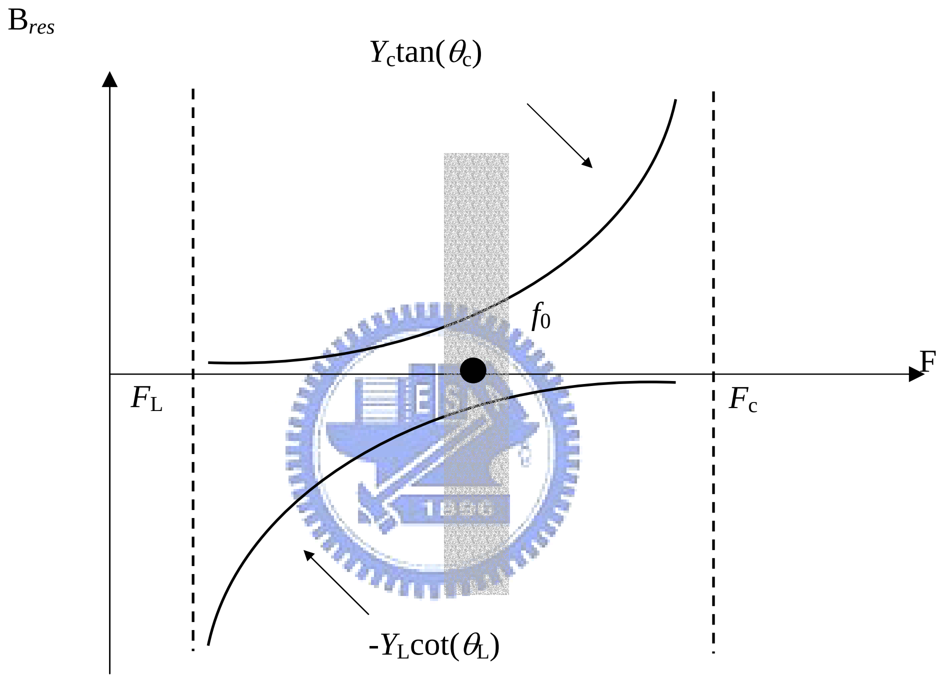

Fig. 3.9 Characteristics of input susceptance of transmission-line parallel resonator.

Next, the conventional lowpass filter synthesis procedures are invoked for the transmission line (TL) bandpass filter (BPF) design for an Nth-order lowpass filter prototype with a specified passband ripple, as shown in Fig. 3.10 (a) [57]. Figure 3.10 (b) transforms the series inductor (g_2) into a T-network of two J-inverters and one shunt capacitor after some algebraic manipulation and conversion [53]. The passband bandwidth and the reference impedance at the input and output ports of the filter are specified during the filter design; then, the lowpass-to-bandpass transformation of Fig. 3.10 (b) leads directly to Fig. 3.10 (c), consisting of the N shunt L-C resonators with N-1 series J inverters [53]. Finally, the TL elements are applied to realize the parallel resonator and J inverters, forming a transmission-line BPF [57]. Notably, Z_{ci}, Z_{Li}, F_{ci} and F_{Li} shown in Fig. 3.10 (d) are the same as those defined in Fig. 3.8 (b).

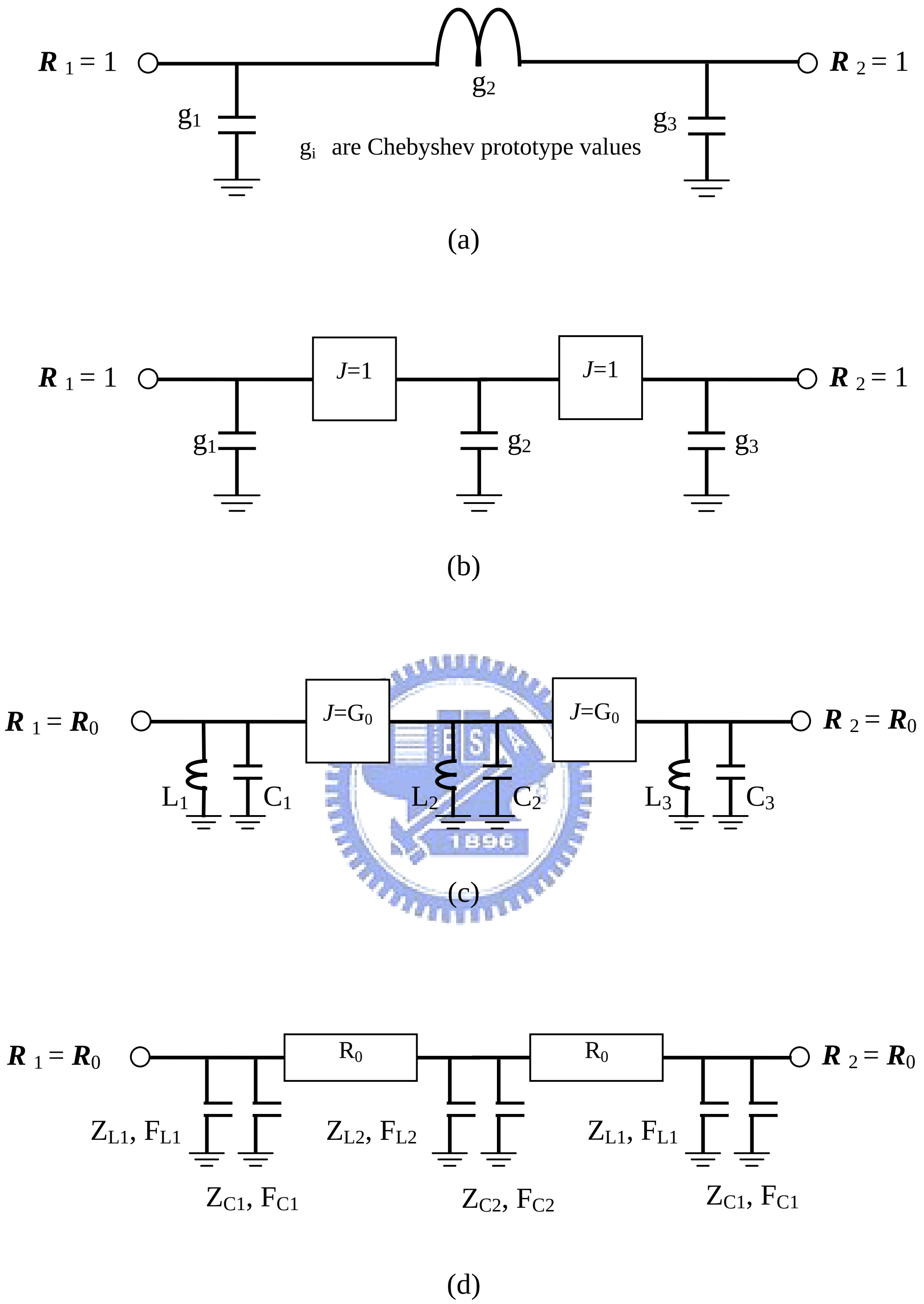

Fig. 3.10 Brief description of the transmission-line bandpass filter design: (a) Lowpass prototype, (b) Conversion of series inductors to shunt capacitors, (c) Lowpass to bandpass transformation, (d) transmission lines approximations of parallel resonators and *J* inverters.

3.3 *Miniaturized Transmission-Line Bandpass Filter: Layout and Measurements*

This section presents the practical implementation of miniaturized banspass filter (BPF) by mapping the idealized BPF shown in Fig. 3.7 to the four-layer stacked CCS TL filter configuration, as presented in Fig. 3.2. Figure 3.11 shows the three-dimensional view of the miniaturized (BPF), incorporating a multi-layer complementary conducting strip transmission line (CCS TL). The CCS TL is realized by a unit cell with a period of 0.35 mm (*P*=0.35 mm), and realized in a multi-layer print circuit board (PCB). The permittivity and thickness of each substrate are 4.7 and 0.06 mm with a loss tangent of 0.013. All metal layers are copper with a thickness of 0.0175 mm. The guiding characteristics of CCS TLs, including the propagation constants and the characteristic impedances, are extracted from the theoretical S-parameters, which are calculated by the full-wave EM-simulator [52]. The extracted data are applied to define the width and the meandered shapes of the CCS TLs in different layers. As shown in Fig. 3.11, five TLs, including two series TLs with an electrical length of 64.428^{o} at 2.5 GHz, two 90^{o} shunt stubs at 1.88 GHz, and one 90^{o} shunt stub at 3.19 GHz are in M1 and M2 metal layers. Additionally, two 90^{o} TLs at 3.95 GHz and one 90^{o} TL at 1.78 GHz are realized using sandwiched CCS TLs in M2, M3 and M4 metal layers. The minimum and maximum linewidths are 0.11 mm and 0.18 mm, respectively. The reference ground planes (M2 and M4) of the four-layer configuration are connected by plated-holes filled with copper for proper grounding. Two external terminals of the BPF are located on the M1 layer, facilitating the interface to the probe tips.

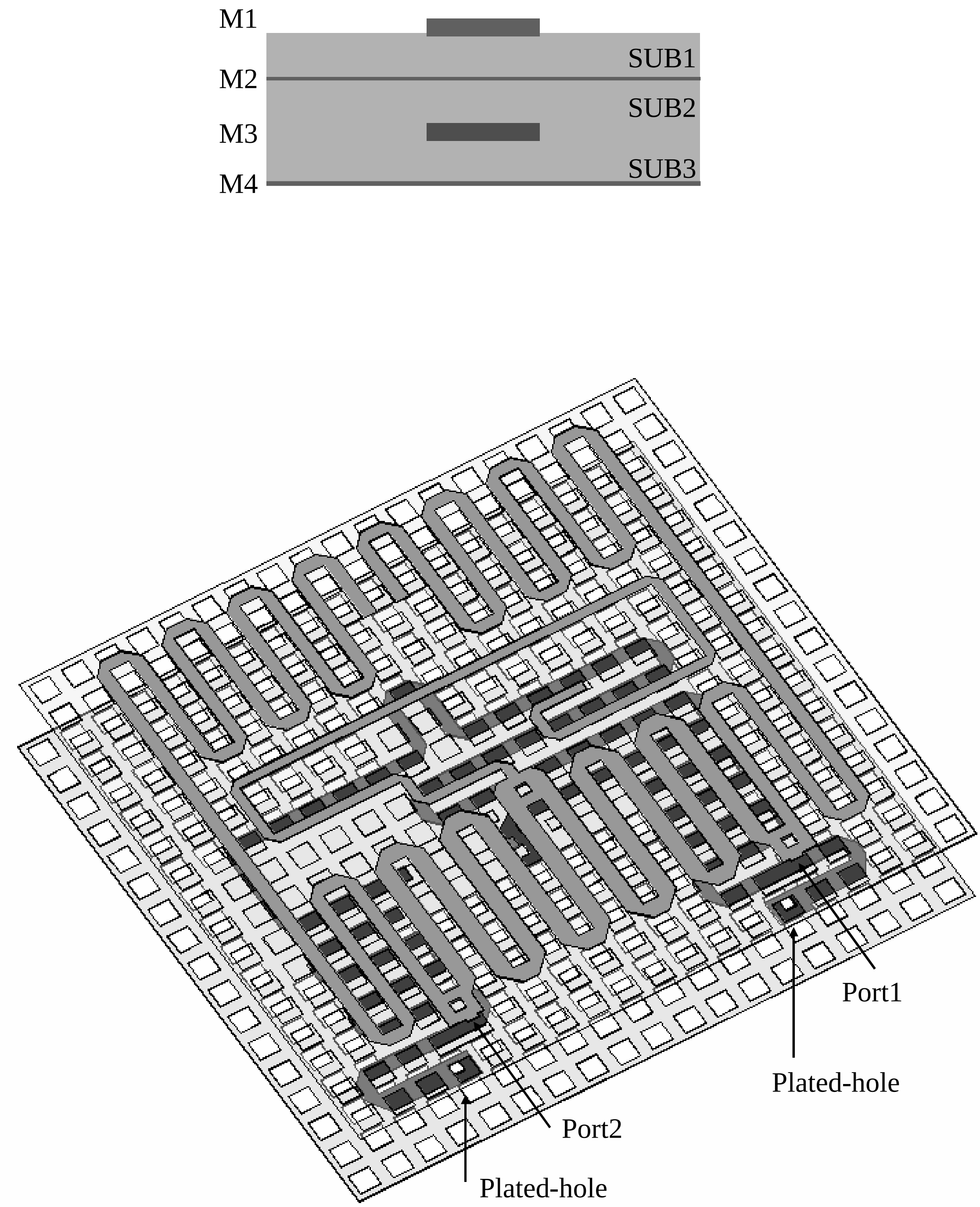

Fig. 3.11 Three-dimensional view of transmission-line bandpass filter realized by multi-layer complementary conducting strip (CCS) transmission line (TL).

The device under test (DUT) is very thin and small, so measurements cannot be easily made using coaxial connectors or cables. Therefore, two 50Ω G-S-G CPW-based microwave probes from Picoprote$^{\text{TM}}$ are applied to make the measurements. The chuck, which is a metal plate for supporting the DUT, is grounded to the instruments. Therefore, a piece of paper with a thickness of 0.05 mm is inserted between the DUT and the chuck for proper isolation. Figure 3.12 shows the experimental setups for measuring the multi-layer miniaturized bandpass filter. Before the measurements are made, the whole system, including an Agilent$^{\text{TM}}$ 8510C vector network analyzer (VNA), cables and probes, is calibrated by performing two-port SOLT (Short-Open-Load-Through) procedures with CS-11 standard substrates from Picoprobe$^{\text{TM}}$. Figure 3.13 compares the measured and theoretical results. The theoretical data include the effects of the junctions, the grounding vias and the plated through-holes, as well as the finite conductivity and dielectric losses.

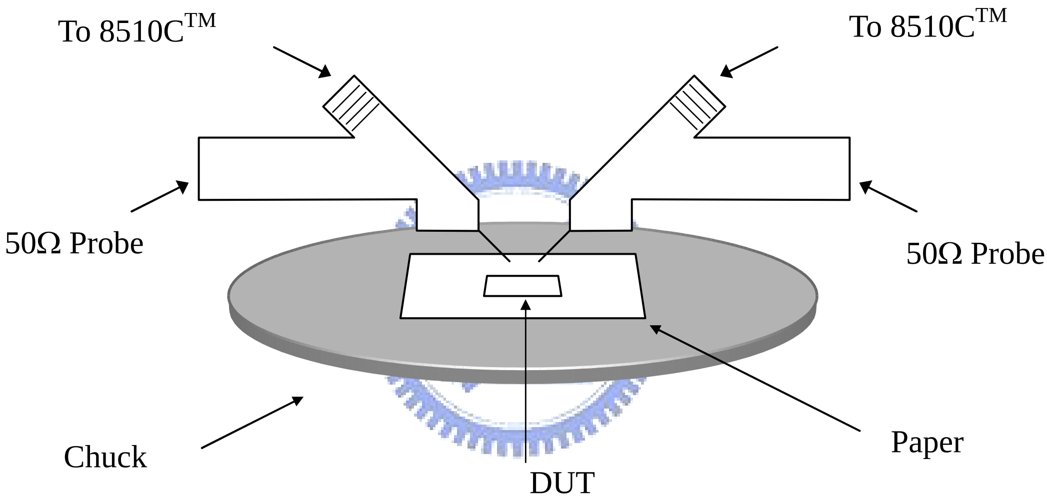

Fig. 3.12 Experimental setups for measuring miniaturized BPF.

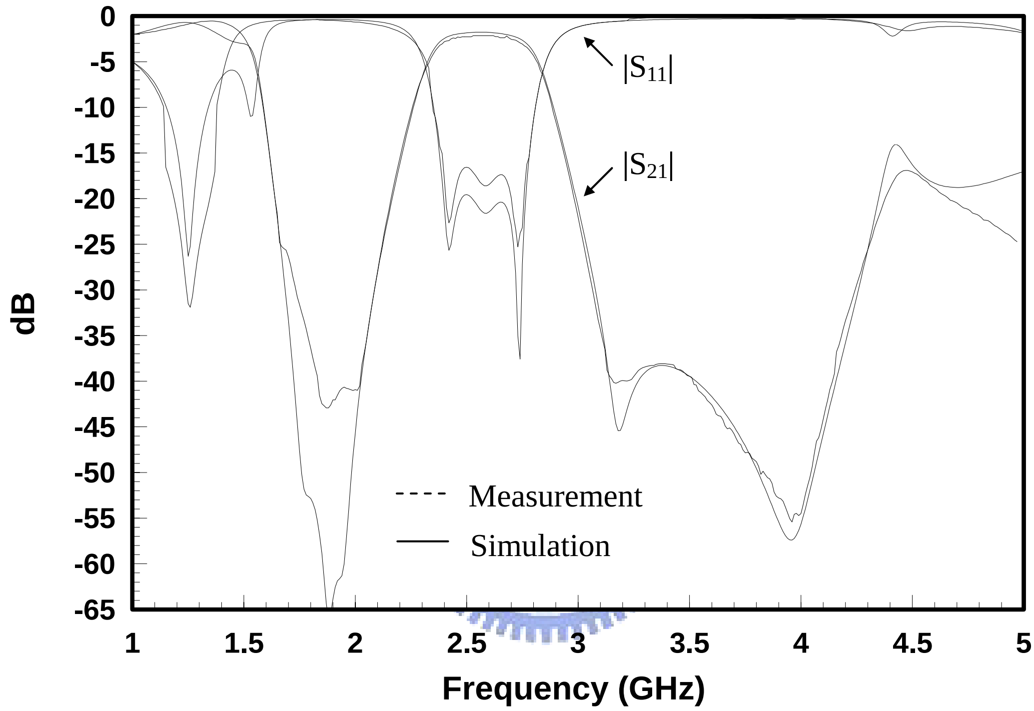

Fig. 3.13 Measured results of miniaturized bandpass filter.

The measured data shows four transmission zeros at 1.85 GHz, 1.98 GHz, 3.19 GHz and 3.95 GHz. Notably, the low-side transmission zeros are shifted by approximately 5% (70 MHz) from ideal data in Fig. 3.7 (b). The center frequency of the BPF is slightly shifted from 2.5 GHz to 2.55 GHz, by approximately about 2%. However, Fig. 3.13 shows that the out-band rejection is highly consistent with the theoretical values predicted by simulation, remaining below 35dB from 3.1 GHz to 4.15 GHz. On the other hand, the measured return-loss, is below -16.8 dB from 2.38 GHz to 2.78 GHz in the passband, exceeds the simulated value by 3.05 dB. Notably, the three reflection zeros are present at approximately 2.42 GHz, 2.58 GHz and 2.74 GHz, offset by only 1% against the idealized design of Fig. 3.7. The measured insertion-loss is approximately 2.46 dB from 2.38 GHz to 2.78 GHz - approximately 0.4 dB above the simulated value. Figure 3.14 shows the photograph of the prototype, whose dimensions are 5.0 X 5.0 X 0.18 mm.

Fig. 3.14 Photograph of 2.4 GHz miniaturized bandpass filter on one Euro (€1).

3.4 *Discussion*

The miniaturized filter is implemented solely using the stacked complementary conducting strip transmission lines (CCS TLs) so the total volume of the filter can be expressed by the following equation:

$$\mathrm{V}_{\mathrm{total}} = L_t \cdot P \cdot (2 - \frac{1}{N}) \cdot h \tag{2}$$

L_t is the total length of the all of the transmission lines in the filter design. P is the period of the unit cell of the CCS TL. N is the number of signal layers in the multi-layer system configuration, and h is the thickness of single-layer substrate. Therefore, the number of substrates is $2N$-1. N_z is the number of transmission zeros with a minimum value of two. In the first-order approximation, L_t is inversely proportional to the square root of the relative dielectric constant ($\sqrt{\varepsilon_r}$). With reference to Fig. 3.7, the total volume of the three-order 2.4 GHz BPF (with four transmission zeros) can be estimated using (2). Table 3.1 presents the results and lists the relevant parameters in detail, showing good agreement between hand calculations and prototype dimensions.

Table 3.1 Variables for Volume Estimation of Proposed Bandpass Filter

Variable	Value
f_0	2.5 GHz
N_z	4 (1.78 GHz, 1.88 GHz, 3.19 GHz, 3.95 GHz)
N	2
h	0.06 mm
ε_r	4.7
P	0.35 mm
L_t	115.1 mm
$V_{estimate}$	3.63 mm^3
$V_{prototype}$	4.5 mm^3

The parameters in Table 3.1 show that P, h, ε_r and N, are process-related. These parameters are typical in the present PCB technology. On the other hand, L_t and N_z are related to electric specifications of the proposed miniaturization that incorporates the meandered CCS TL to reduce systematically the volume of BPF, which approaches the limits of state-of-art technology. The estimated V_{total} is 19% less than that of the prototype, so the approach based on the proposed stacked meandered CCS TL can effectively miniaturize microwave passive circuits, such as the BPF presented here.

On the other hand, the proposed stacked multi-layer complementary conducting strip transmission line (CCS TL) focuses on the miniaturization of the filter to the highest degree of integration density. What follows is the survey of the filters, which include the state-of-the-art discrete filters reported recently in the market [58-62, 64-65, 67-68, 71-72], technical literature [63, 66, 69-70, 73-91], and the filters in advanced SIP [92-97].

Closely examining the statistics shown in Fig. 3.15, supports the following summary. First, the volumes required to realize BPF with three reflection zeros (N_{RZ}=3) are about one half of those of BPF with two reflection zeros. Second, these commercially available LTCC (low temperature co-fire ceramic)-based filters contain approximately ten layers or more, and so are approximately 0.8 mm thick in most designs. Third, transmission-line-based microwave filters [73-76] are normally large with volumes of over 14 mm^3, independent of the number of reflection zeros in the passband. Figure 3.15 also presents the sizes of the proposed filter integration method with various numbers of dielectric layers adopted for BPF designs for two and three reflection zeros, respectively.

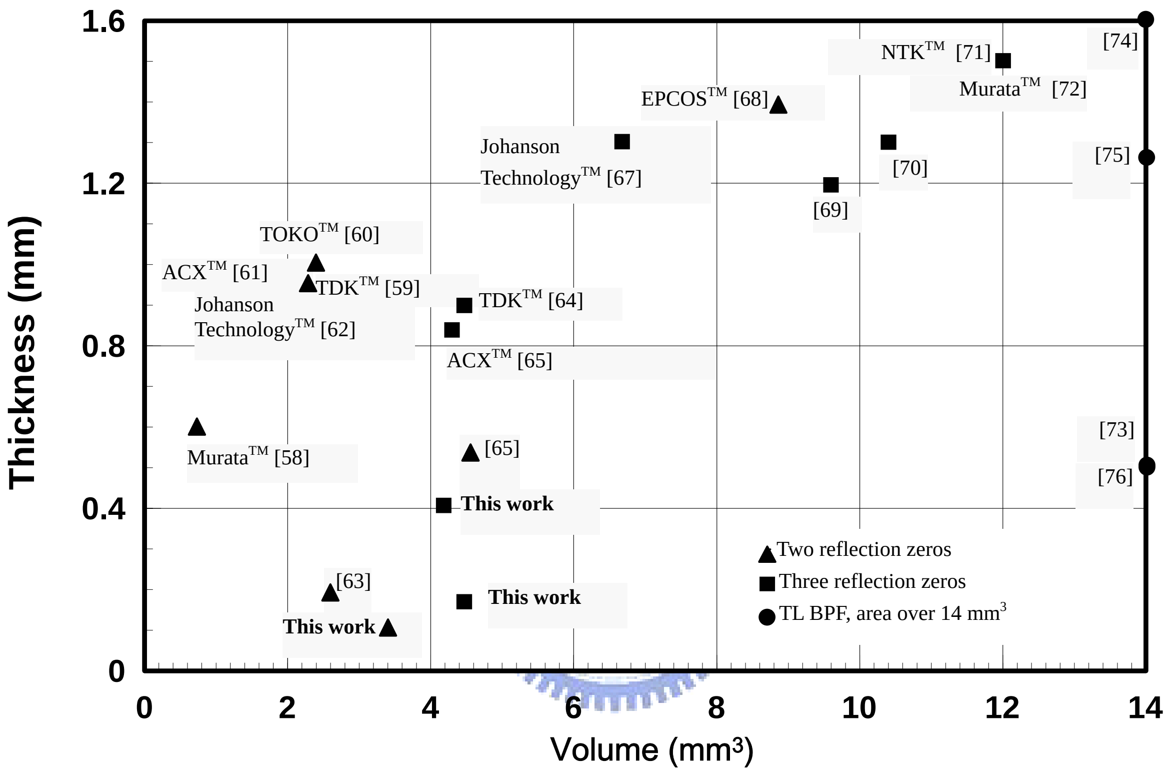

Fig. 3.15 A Survey of 2.4 GHz ISM band bandpass filter in size (volume) and thickness.

With reference to Fig. 3.15, the size of the proposed prototype also approaches that of state-of-art technology – approximately 4.5 mm^3. In the circumstance, when a designer requires that the area is smaller than that achieved using the presented four-layer prototype, N may be increased from two to four. By doing so, the area will be changed from 5 mm X 5 mm to 1.83 mm X 1.83 mm. The thickness will increase be from 0.18 mm to 1.26 mm, and the volume will change from 4.5 mm^3 to 4.23 mm^3. (2) also clearly shows that when P and h are reduced, the total volume is scaled down to an extent proportional to the product of P and h. Also, P stands for the periodicity of the unit cell and is the limit on the line pitch, which is the center-to-center distance between the parallel lines associated with particular processes.

CHAPTER 4
EBG Enhanced PCB / Monolithic Spiral Inductors

In this chapter, the microstrip line on the electromagnetic bandgap (EBG) ground plane is introduced for the third kind of synthetic waveguide. Similar to the uniplanar compact photonic bandgap (UC-PBG) reported by Itoh et al. in 1997, the proposed EBG ground plane changes the guiding characteristics of the microstrip, increasing the slow-wave factor (SWF) for the operation frequency below the first stopband [98-99]. Furthermore, this chapter applies those synthesized guiding characteristics presented in Section 4.1 to develop a new planar inductor configuration, so-called EBG enhanced spiral inductors. The EBG enhanced inductor consists of a two-dimensional EBG periodical array beneath the conventional spiral inductor. Section 4.2 illustrates the physical models of the planar spiral inductor and guiding characteristics of the spiral on EBG ground plane to reconcile the merits offered by the EBG inductor, which results in higher characteristic impedance (Z_c), higher slow-wave factor (SWF), and less attenuation constant (α) of spiral inductor on the EBG ground plane. The experimental verifications have been carried out by employing modern multi-layered printed-circuit-board (PCB) and standard 0.25um 1P5M CMOS technologies without additional processing requirements. Section 4.3 reports the measured results confirm that the Z_c, SWF and α of the EBG inductor can be improved simultaneously. Consequently, the main factors of the spiral inductor including the inductance, series resistance, shunt RC parasitic, and Q-factor are improved using proposed inductor configuration.

4.1 *Guiding Characteristics of the Microstrip line on the EBG Ground Plane*

Electromagnetic Bandgap (EBG) structures are generally the electromagnetic devices made of metal strips, which often conduct DC currents [34, 100-102]. However, such devices can not conduct AC currents within a stopband. Such a structure is occasionally called the "high impedance surface" or a "magnetic conductor". In contrast to plain conductors, the high impedance surface does not support the propagation of surface waves, and it reflects electromagnetic waves without phase reversal within a stopband. To investigate the effects of EBG ground plane on the microstrip line, the experiment is conducted using multi-layer print-circuit-board (PCB) technology to extract the propagation characteristics of a uniform microstrip on EBG ground plane.

Figure 4.1 shows the multi-layer architecture. The microstrip, as shown in Fig 4.1(a), is 5.0 mm long (L) and 1 mm wide (W_1). The EBG ground plane consists of two-dimensional periodical structures that are similar to those reported in the chapter 2. The top coil at $z=h_2$ is comprised of a 0.2mm wide (S_1) rectangular loop with a perimeter of 5.4 mm. Similarly, a 0.2 mm wide bottom coil has a perimeter of 6.2 mm. Notably both the top and the bottom coils are connected to center via by short metal strips of 0.2 mm (C_1) by 0.2mm (C_2). The diameter of all the via-through holes is 0.25mm (d).

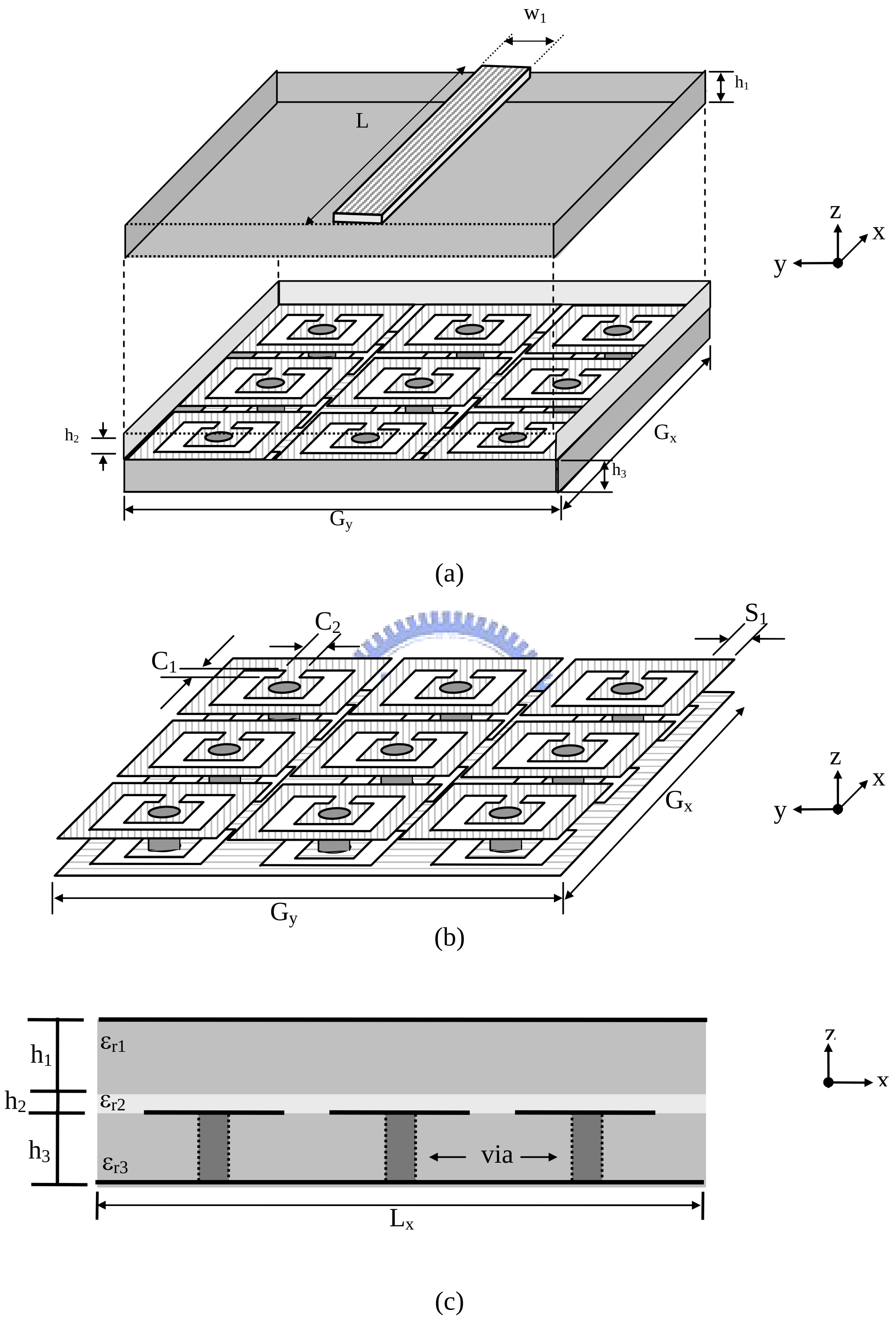

Fig. 4.1 The microstrip line on the EBG ground plane: (a) three-dimensional view, (b) multi-layer EBG ground plane, (c) cross-section view of the multi-layer configuration.

The microstrip line and the PBG cells are made on printed RO4003^{TM} circuit boards of thickness (h_1=h_3) 0.2mm, a relative permittivity (ε_{r1}=ε_{r2}=3.38), and a loss tangent ($\tan\delta_1$=$\tan\delta_2$) of 0.002. The prepreg with thickness of 0.05 mm (h_1), relative permittivity (ε_{r2}) of 4.4, and a loss tangent ($\tan\delta_2$) of 0.01 is sandwiched between the microstrip and EBG ground plane. The thickness of the metal through the Fig. 4.1 is 17um with conductivity of $5.8\text{x}10^7$ S/m. During the measurements, two microstrip lines, which are identical except in ground planes, were built and test. Notably, the effective substrate thickness of the microstrip line on the PBG ground plane, (h_1+h_2=0.25mm), is thinner than the microstrip line on the uniform ground plane, (h_1+h_2+h_3=0.45 mm). The total circuit size is 5.0 mm (G_x) by 5.0 mm (G_y), corresponding to 3 by 3 EBG cells.

The scattering parameters of the microstrip lines are measured using the WILTRON^{TM} 3680K test fixture and HP8510C Vector Network Analyzer after two-port standard calibration procedure so-called short-open-load-through (SOLT). Then, the complex propagation constant (γ) and the characteristic impedance (Z_c) of the microstrip line extracted from the measured scattering parameters (S_{ij}) [52].

Figure 4.2 (a) plots the extracted complex propagation constant. The normalized phase constant, β/k0, which is also called the slow-wave factor (SWF), corresponds to the left-hand side of the vertical axis, and the attenuation constant, α, corresponds to the right-hand side and of the vertical axis. The SWF of the microstrip on the uniform ground plane is 1.7 in the entire frequency band of interest, whereas the microstrip on the EBG ground plane increases the SWF by 17.6% to 2.0. The propagation loss, α, of the microstrip line on the uniform ground plane slightly exceeds that of the microstrip on the EBG ground plane. In this work, the effective substrate thickness of the microstrip on EBG ground plane is reduced by 44% smaller than that of the microstrip on the uniform ground plane. Therefore, the characteristic impedance (Zc) of the microstrip line on the EBG ground plane is decreased by 14%, as shown in Fig. 4.2 (b). In the following section, the same PCB fabrication process and the EBG magnetic surface as shown in Fig. 4.1 are applied to the design of EBG-inductor.

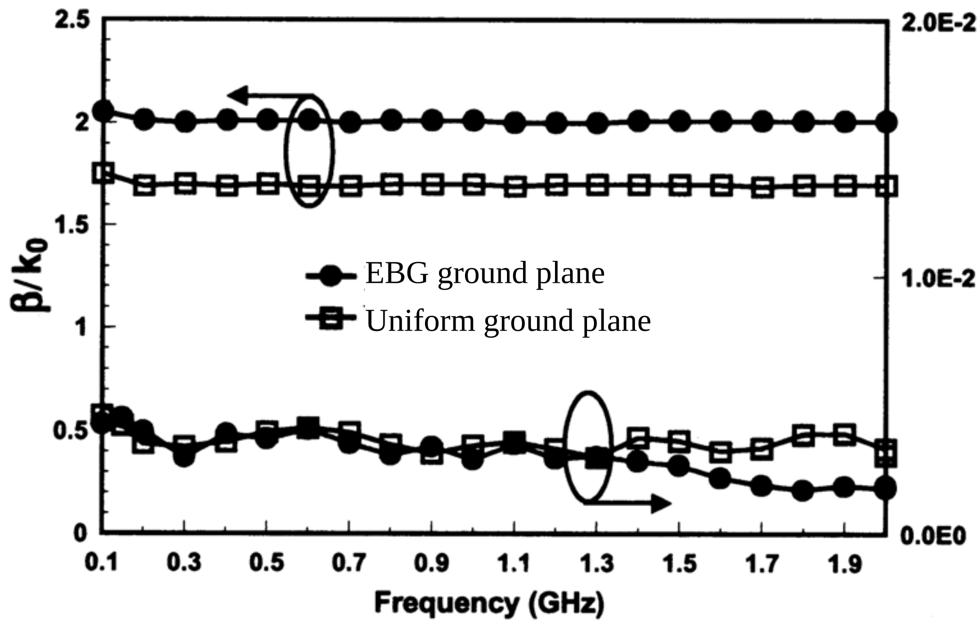

(a)

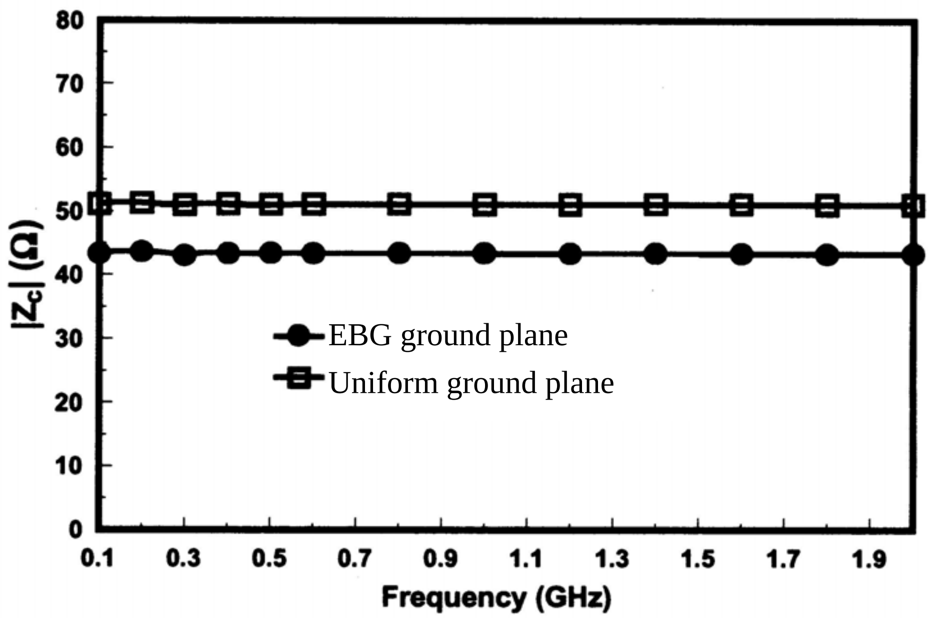

(b)

Fig. 4.2 Characteristics of the microstrip line on the uniform ground plane and EBG ground plane: (a) complex propagation constant, (b) characteristic impedance.

4.2 *Equivalent Model for the Rectangular Spiral Inductor*

The lumped inductor is an extensively used passive device in microwave radio frequency (RF) circuit designs. The properties of inductors also dominate the RF circuit's performance. For example, Leeson-Cutler's phase noise model indicates that a higher inductor Q improves the phase noise performance of the oscillator. The above considerations signify the importance of importance of inductors in most RF circuit, and further derive the modeling effort to inductors. From a physical perspective, equivalent circuit models have been developed to characterize inductors [103-105]. Figure 4.3 shows a well-known lumped circuit model of the spiral inductors.

In the lumped model, L_s represents the inductance of the spiral, which is proportional to both the total length and the characteristic impedance of the spiral. R_s is the series resistance of the spiral whose behavior at radio frequency (RF) is governed mainly by the eddy current losses and the skin effect [106-107]. The series capacitance, C_s, which is the capacitance due to the overlap between the spiral and the underpass, is considered independent of frequency. The shunt parasitic of the inductor model include the substrate capacitance and the substrate, named by C_p and R_p, respectively. C_p represents the capacitance between the spiral and the conducting media. R_p represents energy dissipation in the supporting dielectric and conducting media around the spiral. The qualify factor (Q-factor) of the spiral inductor can be defined by

$$Q = 2\pi \cdot \frac{\text{Energy stored in the inductances}}{\text{Energy loss in one oscillation cycle}} \tag{1}$$

Based on the equivalent circuit model showed in Fig. 4.3, the Q-factor can be expressed by [103].

$$Q = \frac{\omega L_s}{R_s} \cdot \frac{R_P}{R_P + [(\omega L_s / R_s)^2 + 1]R_s} \cdot \left[1 - \frac{R_s^2 (C_s + C_p)}{L_s} - \omega^2 L_s (C_s + C_p) \right] \tag{2}$$

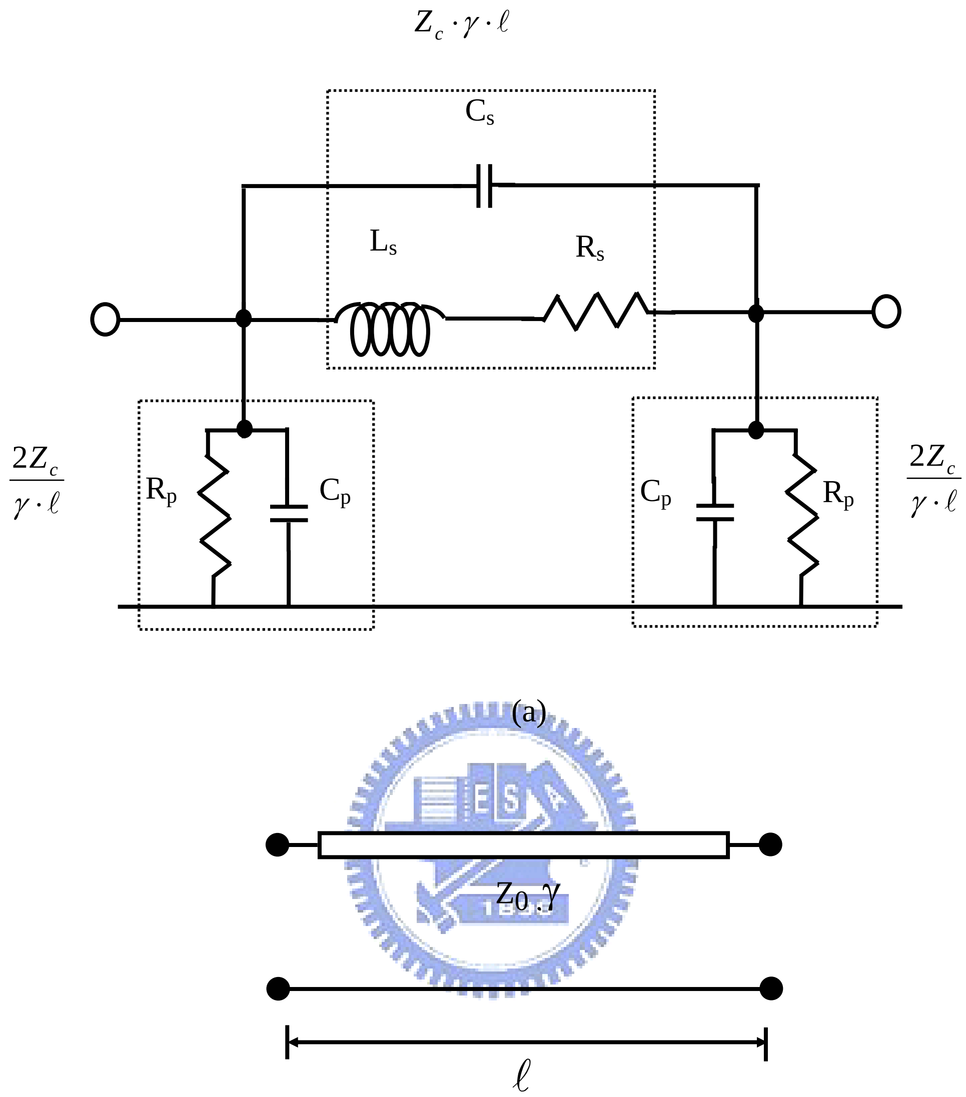

(b)

Fig. 4.3 The equivalent models for the rectangular spiral inductor: (a) lumped model, (b) transmission line model.

Factors that contribute to the Q-factor of the spiral inductor are 1) the energy stored in the inductance and the ohmic loss of series resistance; 2) the substrate loss factor, and 3) the self-resonance factor. Moreover, the elements in the lump circuit model can also be represented by equivalent transmission line parameters [104-107]. Where Z_c, γ, and ℓ represent the characteristic impedance, propagation constant, and overall length of the spiral, respectively. The propagation constant is denoted by $\gamma=\alpha$ (attenuation constant, Np/m) $+j\beta$ (phase constant, rad/m). The series impedance branch in the lumped model, specified by L_s, R_s, and C_s, equals to the product of Z_c, γ, and ℓ. C_s is extracted using the low-frequency L_s value and the resonant frequency of the series branch [104]. Then, with C_s held constant, L_s, and R_s are determined. The shunt parasitic can also be extracted from the ratio of $2Z_c$ to $\gamma\ell$. However, the model in Fig. 4.3 is valid only when $|\gamma\ell|$ is substantially lower than one (refer the Appendix III for the details). Accordingly, the model in Fig. 4.3 provides a design guideline for the inductors.

Either narrowing the line width or increasing the number of turns of the inductor can increase its inductance. Such approaches correspond to increasing of Z_c and ℓ of the spiral. Other designs for a high-quality spiral inductor include using thick metal strip, high resistivity substrate, or removing the lossy substrate [108-111], but often accompany additional process requirement. One widely accepted approach is to use the patterned ground shield (PGS) beneath the inductor as an electromagnetic shield [112]. The PGS not only prevents the electric field from penetrating into the lossy substrate, but also inhibits the image eddy currents while simultaneously facilitating standard IC fabrication.

In an effort to develop a spiral inductor, which can simultaneously increases β and Z_c, and decreases α, section 4.2.2 reports a new methodology to improve the planar spiral inductor by incorporating a photonic bandgap (PBG) structure beneath the inductor as a ground plane substitute. The new spiral inductor, called the EBG inductor, is also fully compatible with standard multi-layer fabrication technologies.

4.3 *EBG Enhance-Inductor*

4.3.1 EBG Enhanced PCB Spiral Inductor

This section compares the performance of two identical spirals above a uniformly conducting ground plane and an electromagnetic bandgap (EBG) magnetic surface. Figure 4.4 illustrates the inductor designs. The foregoing observations presented in Section 4.1 conclude that the microstrip line on the PBG ground plane increases SWF and decreases the attenuation constant, thereby a high performance spiral inductor is readily achievable. Figure 4.4 shows two inductor configurations in multi-layered PCB process for verifying the concept of the PBG inductor. Notably the two inductors appeared in Fig 4.4 (a) and Fig 4.4 (b) are identical except in ground.

The design parameters, including substrate information, thickness and conductivity of the metal strip, and dimensions of the EBG cell are corresponding to Fig. 4.1 (b). The substrate, which together with the metallization patterns on both side of the substrate in Fig. 4.4 (b), is lifted here just for illustration. The spiral inductor, which has 1.5 turns and another via-through-hole connecting an underpass for external circuitry, has the following dimensions. The main body of the spiral is 3 mm (L_x) by 3 mm (L_y) with total spiral length (ℓ) of 13.1 mm. Total inductor size is 5 mm (G_x) by 5 mm (G_y). The metal width (w_2) and spacing (S_2) are both 0.25 mm wide. Two short-metal strips of 0.62 mm long and 0.25 mm wide are added at both input and output ports to facilitate the S-parameters measurement. However, the substrate thicknesses of the two kinds of inductor are different. The substrate thickness of the conventional spiral inductor is 0.45 mm (h_1+h_2+h_3), 0.25 mm higher than that of EBG inductor.

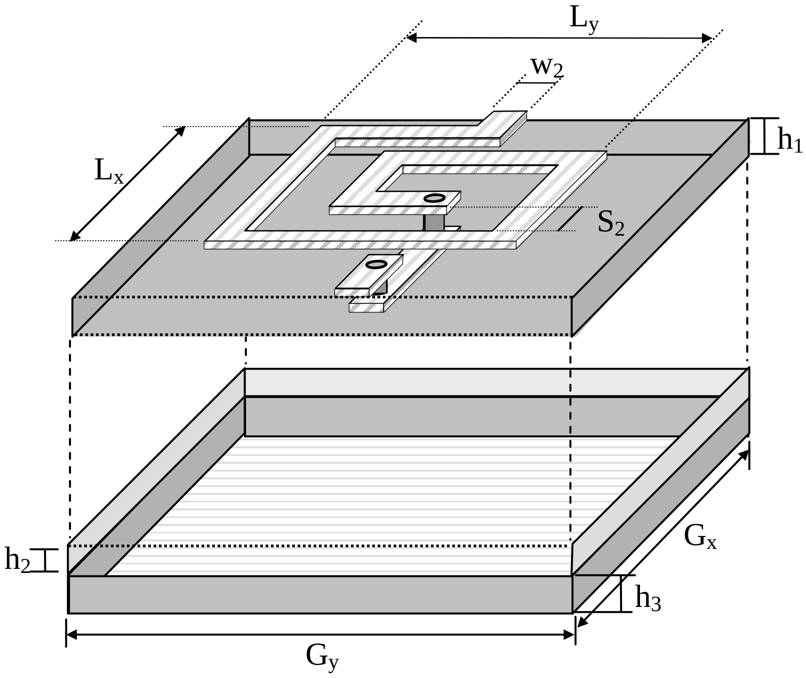

(a)

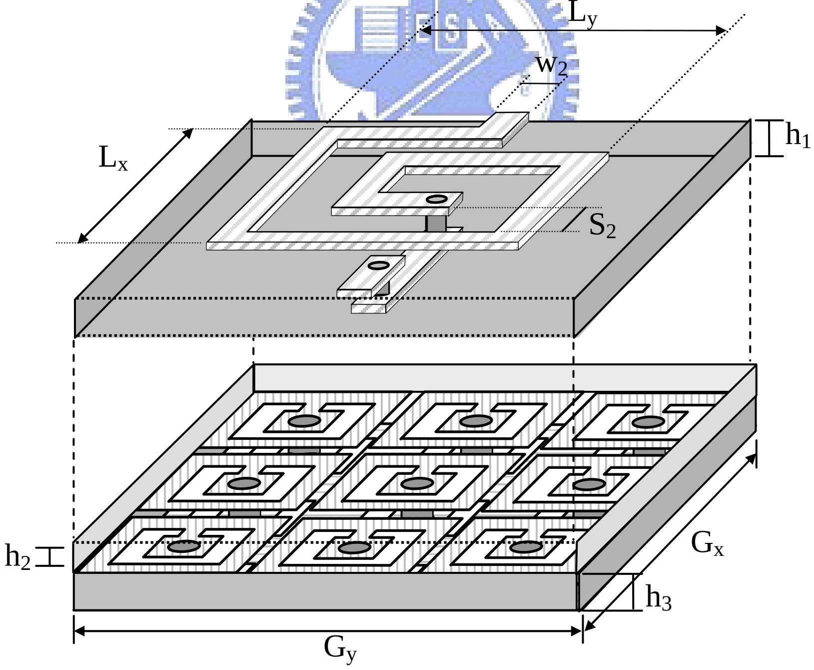

(b)

Fig. 4.4 Spiral inductors on different ground planes; h_1=h_3=0.2 mm, h_2=0.05 mm, G_x=G_y=5.0 mm, L_x=L_y=3.0 mm, S_2=0.2 mm, w_2=0.2 mm. (a) spiral inductor on the uniform ground plane, (b) spiral on the EBG ground plane.

The spiral inductors are fabricated and tested. The precise experiment procedure is carried out as follows. 1), two-port scattering-parameters of the spiral inductors are obtained using the same measurement procedure as described in Section 4.1), input and output pad parasitic are de-embedded using the open dummy pad structure through Y-parameters subtraction. Then the Y-parameters without pads' parasitic are converted to ABCD matrix, representing an equivalent transmission line circuit of the two-port spiral inductor [103]. The $|\gamma \ell|$ here is much less than unity for the frequencies of interests, and hence the spiral inductor model of Fig. 4.3 is applicable. Following the same extraction techniques described in [103], the measured de-embedded Y-parameters lead to the following results. The slow-wave factor (SWF) of EBG inductor as shown in Fig. 4.5 (a) is increased by 14% and α approximately reduced by 20% from 0.1 GHz to 2 GHz. Figure 4.5 (b) shows the characteristic impedance (Z_c) of the EBG inductor is increased by 5% even thought the effective substrate thickness of the EBG inductor is 44% less than the conventional spiral inductor.

The observations mentioned above imply that the geometry of inductor in the case study has strong influence on the characteristics impedance of metal strip above various ground planes. Based on the electric properties of the spiral inductor model shown in Fig. 4.3, EBG inductor property should be significantly improved.

In Fig 4.6, the extracted lumped model elements of inductors are plotted. The series inductance L_s in Fig. 4.6(a) is increased by 7.4% from 0.1 GHz to 2 GHz. The series resistance R_s in Fig. 4.6(b), which is one of the dominant factors determining Q-factor of the spiral inductor, is reduced by 10.2% below 1.4GHz. The series resistance R_s is related to the compound effects of ohmic losses, skin-effect losses and eddy-current losses.

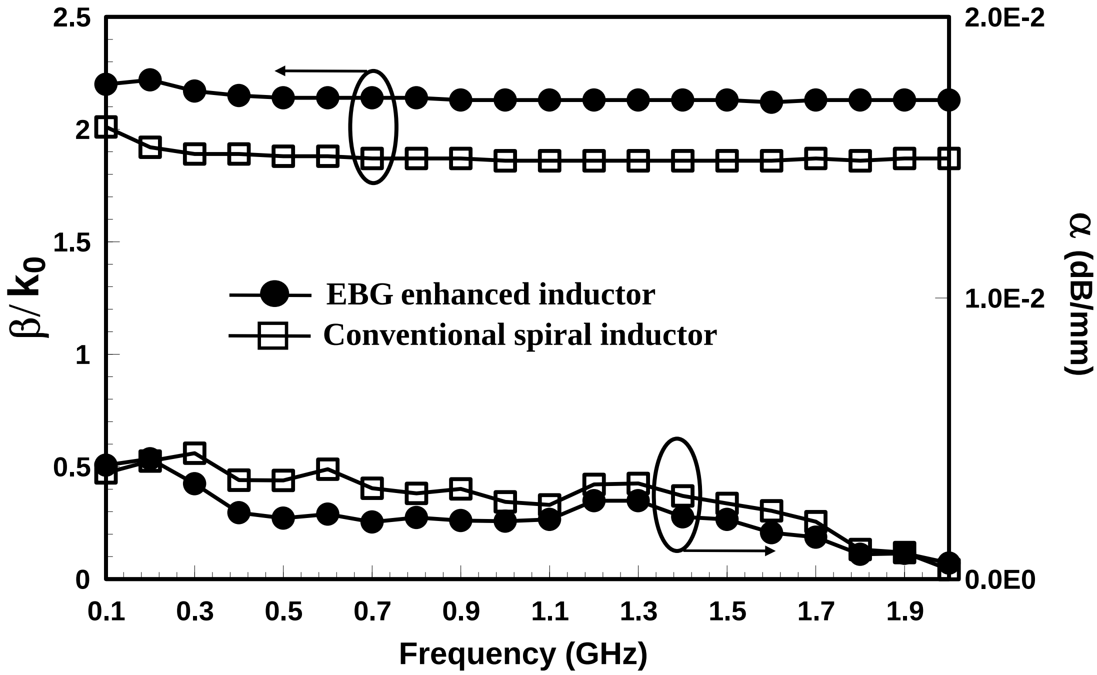

(a)

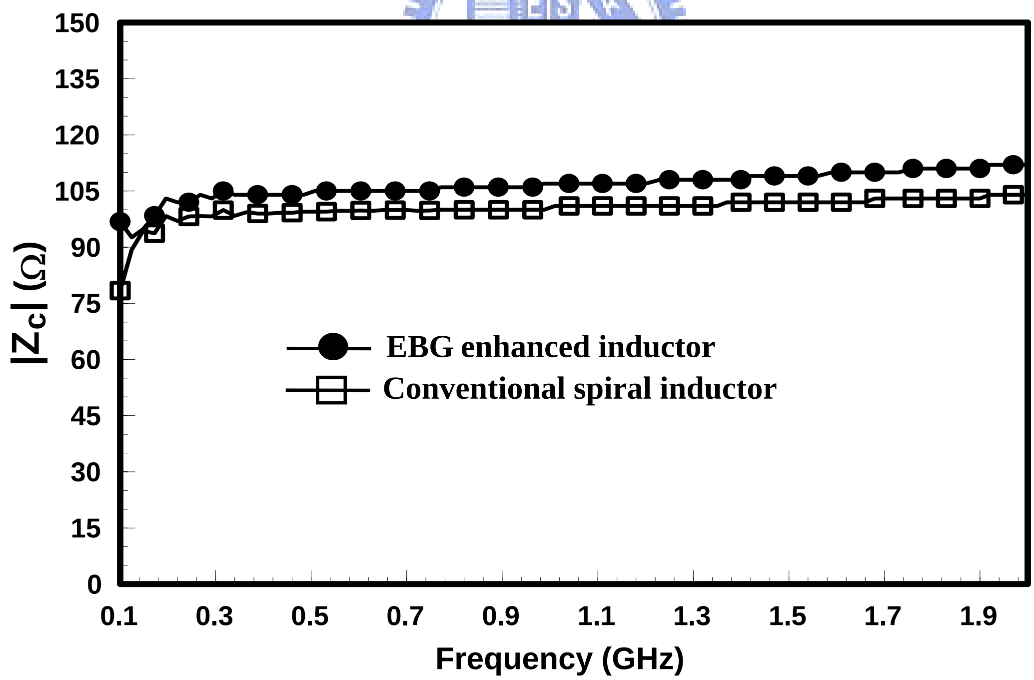

(b)

Fig. 4.5 Equivalent transmission line parameters of the PCB spiral inductor on the uniform ground plane and EBG ground plane: (a) complex propagation constant, (b) characteristic impedance.

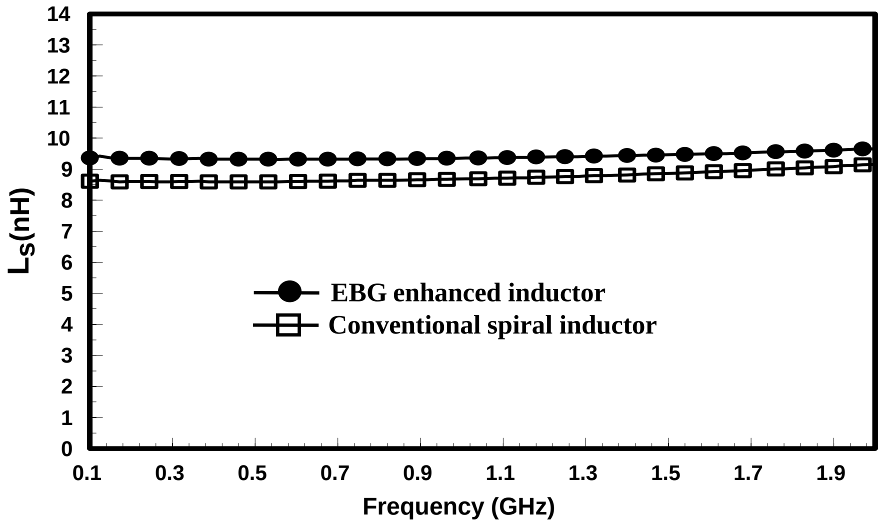
EBG enhanced inductor
Conventional spiral inductor
Ls(nH)
Frequency (GHz)

(a)

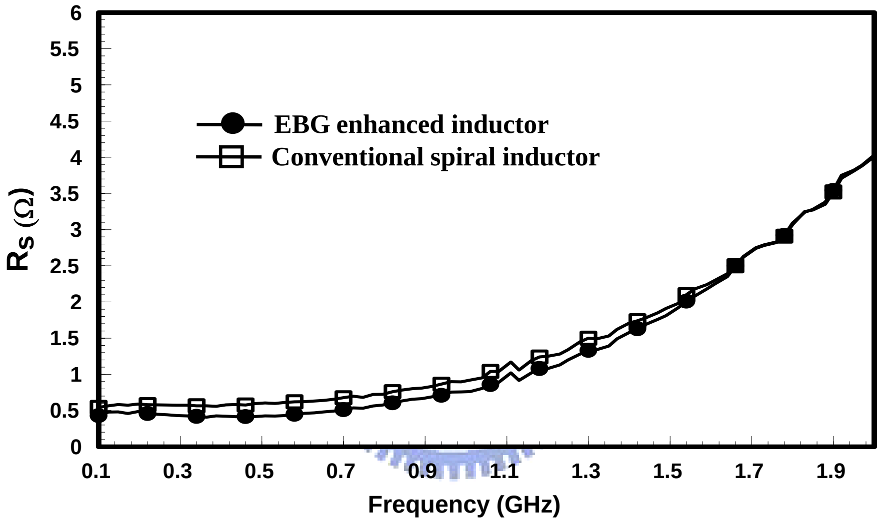
EBG enhanced inductor
Conventional spiral inductor
Rs (Ω)
Frequency (GHz)

(b)

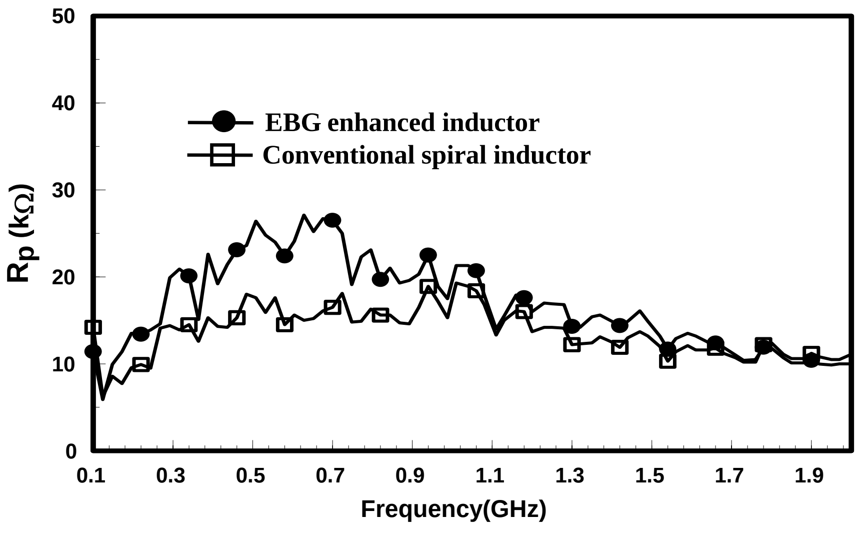
EBG enhanced inductor
Conventional spiral inductor
Rp (kΩ)
Frequency(GHz)

(c)

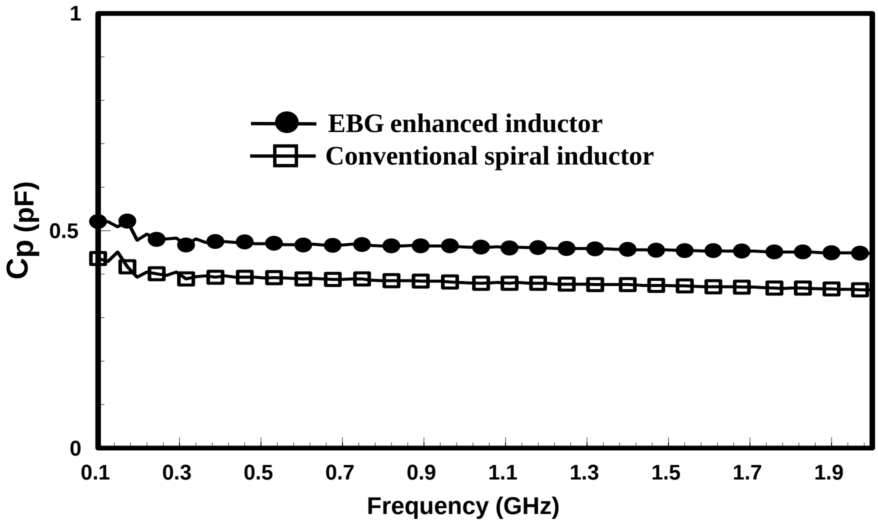

(d)

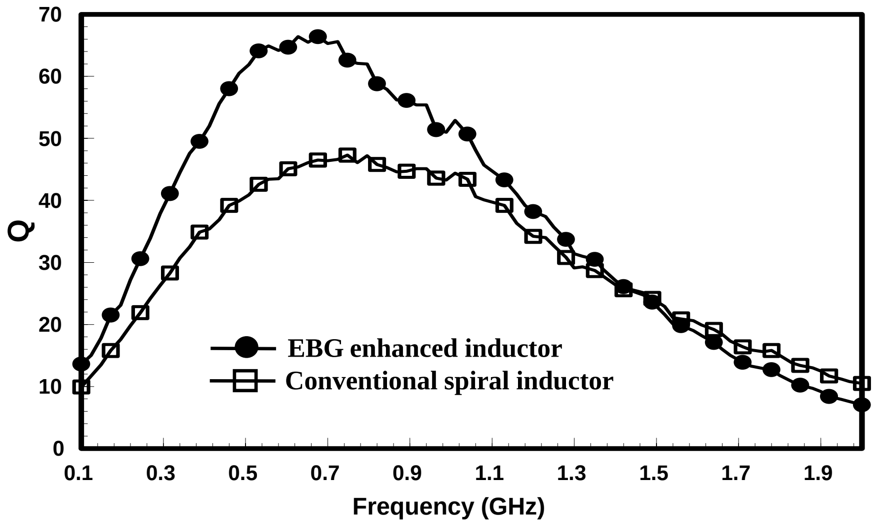

(e)

Fig. 4.6 Measured results for comparing EBG inductor with conventional spiral inductor applying the multi-layer PCB fabrication: (a) series inductances (L_s), (b) series resistance (R_s), (c) parasitic resistance (R_p), (d) parasitic capacitance (C_p), (e) quality factor (Q).

The results implied that the electromagnetic bandgap (EBG) ground plane reduce the eddy-current losses below 1.4 GHz for our particular case study. Since the effective substrate thickness of the EBG inductor is 44% smaller than the conventional one, therefore the shunt capacitance C_p of the EBG inductor plotted in Fig. 4.6(d) is increased by 19.8%. Additionally, the shunt resistance R_p of the EBG inductor is increased by 34.26%, 54.48%, 26.26% at 0.4, 0.6, 0.8 GHz, respectively, implying the substrate ground shield is improved. Fig. 4.6(e) compares the Q-factors between the EBG inductor and conventional one. The conventional spiral inductor has a maximum Q-factor of approximately 45.8 at 0.8GHz, whereas the EBG inductor is peaked at 0.7 GHz at a Q-factor of 65.3, corresponds to 42.5% improvement in the peak Q-factor. The measured results confirm that the overall performance of the spiral inductor has been significantly improved in almost aspects of planar spiral inductor.

4.3.2 EBG Enhanced Monolithic Spiral Inductor

Section 4.3.1 has demonstrated the improvements of inductors using the electromagnetic bandgap (EBG) ground plane based on print-circuit-board (PCB) technology. A desire for similar benefits leads the application of EBG structure in standard CMOS technology. When the inductor design is migrated to such an extent, different design issues must be considered. In a typical PCB fabrication process, the conducting strips are made of copper with a conductivity of 5.8X10^7 S/m, and a thickness of 17um. Most CMOS technology, however, uses 2 um thick aluminum as the conducting metal, whose conductivity is only 3.8X10^7 S/m, implying a significant increase in the inductor's series resistance, R_s. And hence a lower Q-factor for a monolithic CMOS inductor. Moreover, silicon bulk substrate used in CMOS technology typically serves as a lossy material and causes CMOS inductors to incur substate losses and noise coupling [113]. Ground shield techniques can overcome the substrate issue while avoiding additional processes. Nevertheless, the solid ground shield in CMOS is much closer to the inductor strips than that of PCB designs, and the induced eddy current will flow willingly and thus seriously degrade inductor. Therefore, solid ground shield is not suitable to the CMOS RFIC applications. Instead, a ground shield with patterned slots orthogonal to the inductor's metal loop is commonly used to disturb the eddy current and alleviate the degradation of the inductor due to substrate and eddy current losses. This section elucidates a new approach to designing CMOS inductors incorporating a EBG structure as the ground-shielding scheme. The proposed EBG inductor represents an improvement in all aspects of interests, without modifying the fabrication.

The newly designed electromagnetic bandgap (EBG) inductor is fabricated using standard 0.25um mixed signal one polysilicon and five-level metals CMOS technology. Figure 4.7 shows a simplified cross-section view of the 0.25um CMOS foundry. All metals are aluminum, and a thickness of 0.57 um, embedded in the inter-metal dielectric (IMD) layers, except where the metal 5 (M5) has a thickness of 1.5um. The dielectric constant is about 4.1 for the IMD1-IMD4. In this study, the disconnected and connected rectangular coils of the PBG ground plane are built using a polysilicon layer and a M1 layer. The top coils of the PBG cell have a perimeter of 20um and a width of 0.5um. The bottom coils have a perimeter of 20.5 um and a width of 0.5 um. The contacts with dimensions of 0.3um by 0.3um connect the top coil to the bottom coil.

Figure 4.8 shows the electromagnetic bandgap (EBG) inductor prototype for testing: the spiral is fabricated with M5 for the metal strip, and M4 is the underpass to contact the center of the inductors. The EBG ground plane, incorporating M1 as the top coils and polysilicon as the bottom coils, is sandwiched between the spiral and silicon bulk substrate, and connected to ground defined by the GSG probe ground pad thus forming as electromagnetic shield. The space between the spiral metal strip and the top coil of the PBG ground plane is filled with a 6.28um thick dielectric layer. The resistivity of the silicon bulk substrate is 15-25Ω·cm and the thickness is 250um±50um. As shown in Fig. 4.8, the spiral inductor, which has 2.5 turns, a metal wide of 10um, an edge to edge spacing of 2um and a total length of 1578um, is fabricated, denoted by EBG-GS (EBG ground shield) inductor. Another identical inductor, without ground shielding is also fabricated for comparison, and is denote as the NGS (no ground shield) inductor.

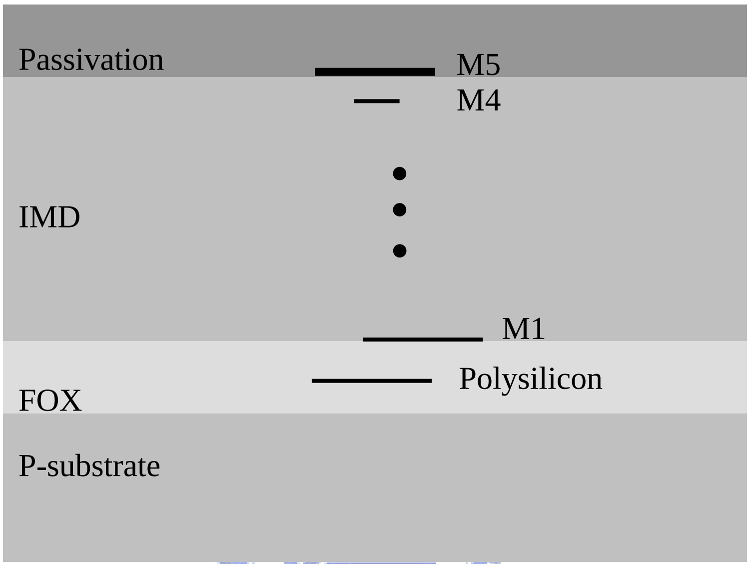

Fig. 4.7 Simplified cross-section view of the 0.25um 1P5M CMOS process.

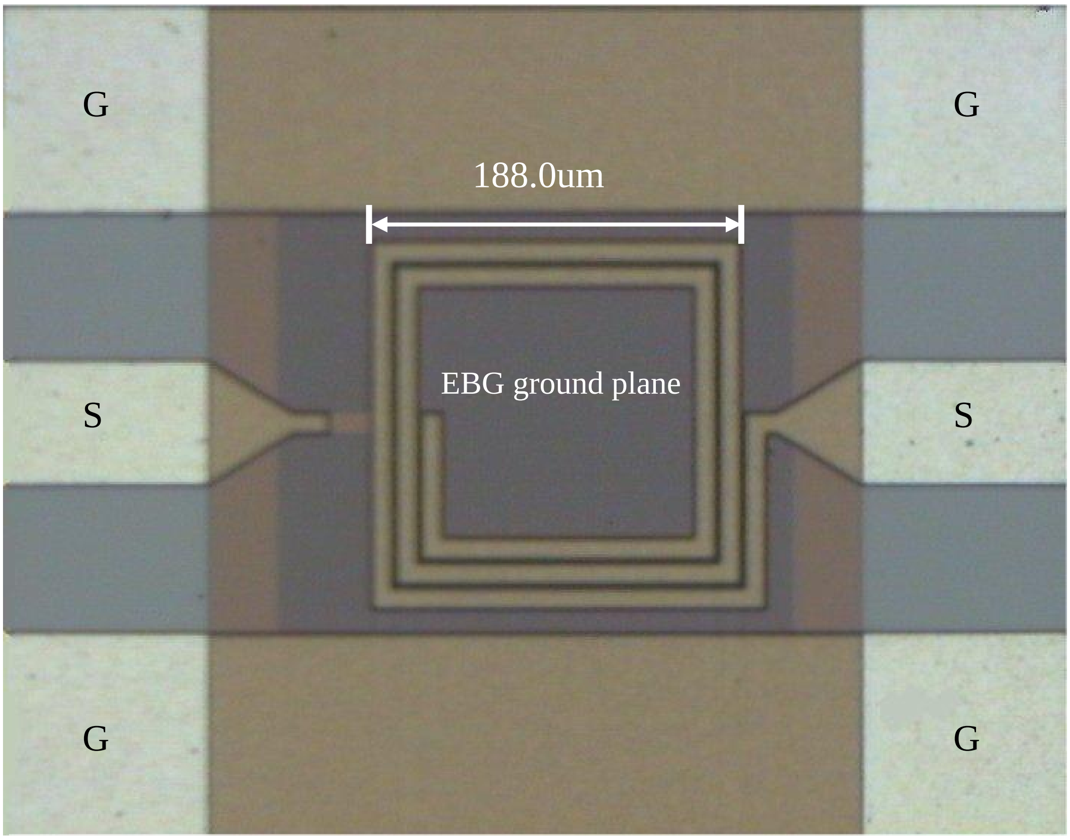

Fig. 4.8 Photograph of the EBG enhance monolithic spiral inductor fabricated using CMOS 0.25um process.

On-Wafer two-port S-parameter measurement was taken using HP8510C Vector Network Analyzer and Picoprobe™ ground-signal-ground (GSG) air-coplanar probe with a 150um pitch. The Picoprobe™ calibration substrate, CS-5, was used to perform a full two-port SOLT (Short-Open-Through-Load) calibration to move the reference plane up to the probe tips. During measurement, the substrate was grounded from wafer backside through the testing chuck. The shunt parasitics associated with the testing pad and the ground reference were de-embedded using open dummy structure. The probes must be replaced once the contact resistance exceeds 0.3Ω to guarantee validity since the constact resistance between the probe tips and the testing pads may change due to wearing in both surfaces caused by repeated measurement. Notably, the contact resistance should be subtracted during the open dummy pad de-embedding procedure. An appropriate number of testing samples is required to obtain consistent and accurate results. Figures 4.9(a) and (b) present the measurement histograms for the NGS and EBG-GS inductors and show that the samples with maximum probability can be regarded as candidates for subsequent parameter extraction.

The equivalent parameters in Fig. 4.3 are extracted to elucidate the effects of the electromagnetic (EBG) ground plane on the CMOS spiral inductor using the same parameter extraction techniques as described in [103]. Figures 4.10 (a) and (b) present the three equivalent transmission line parameters of both EBG-GS and NGS inductors. The EBG-GS inductor shows the parameters improvement over the NGS inductor in all aspects across the entire frequency band of interests. Figure 4.10(a) plots the slow-wave factor (SWF) and α, which correspond to the left-hand and right-hand sides of the vertical axis, respectively. The SWF of the EBG-GS inductor is slightly higher than that of the conventional NGS inductor by 5.12% at 5 GHz. The attenuation constant, α, of the EBG-GS inductor is 46% less than that of the NGS inductor at 5 GHz since the eddy current that flows in the EBG ground plane was disturbed and the lossy substrate was further separated by the EBG ground plane. Furthermore, Fig. 4.10(b) shows that Zc of the EBG-GS inductor also increased by 18.26% at 5 GHz, even though the EBG ground shield is closer to the spiral than that of NGS.

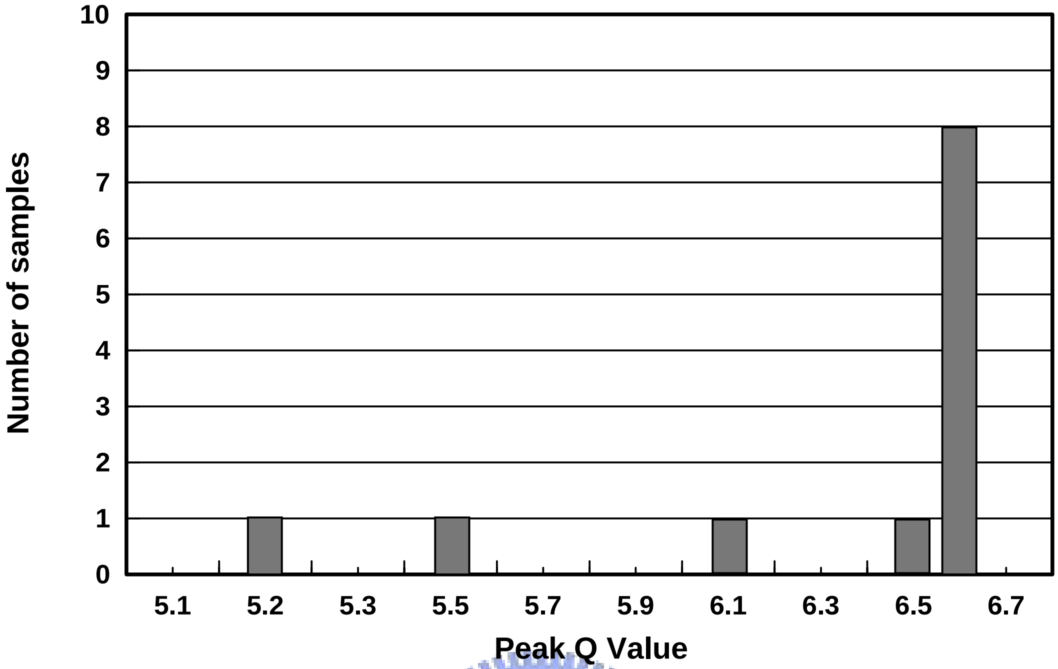

(a)

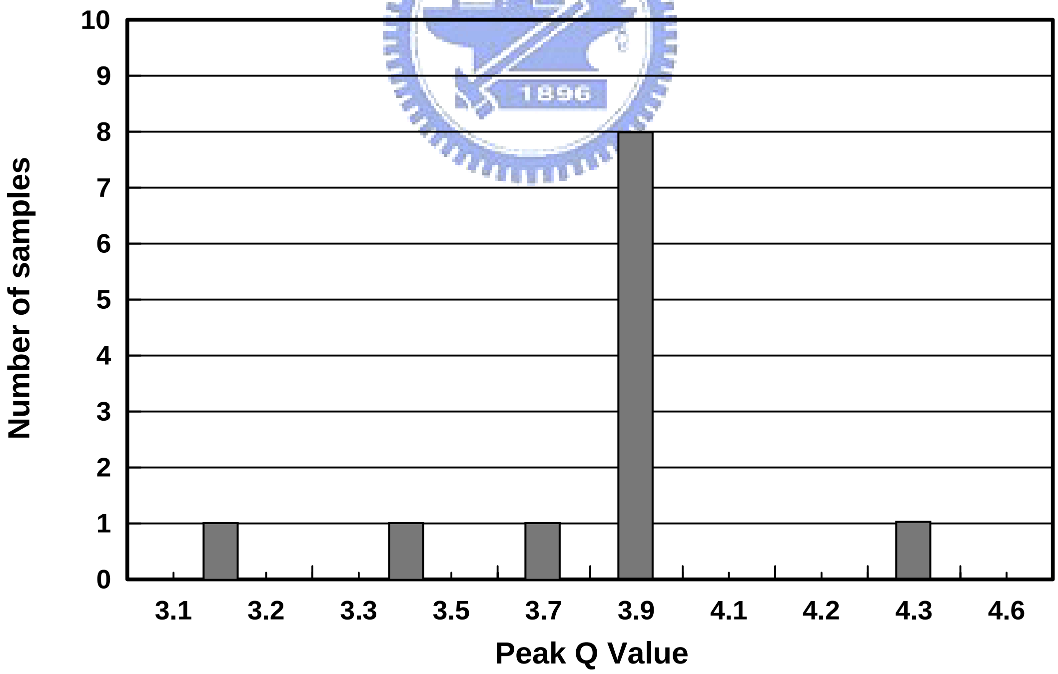

(b)

Fig. 4.9 Histograms of the inductor Q-factors over 12 samples: (a) EBG ground shield inductor (EBG-GS), (b) conventional inductor with no ground shield (NGS).

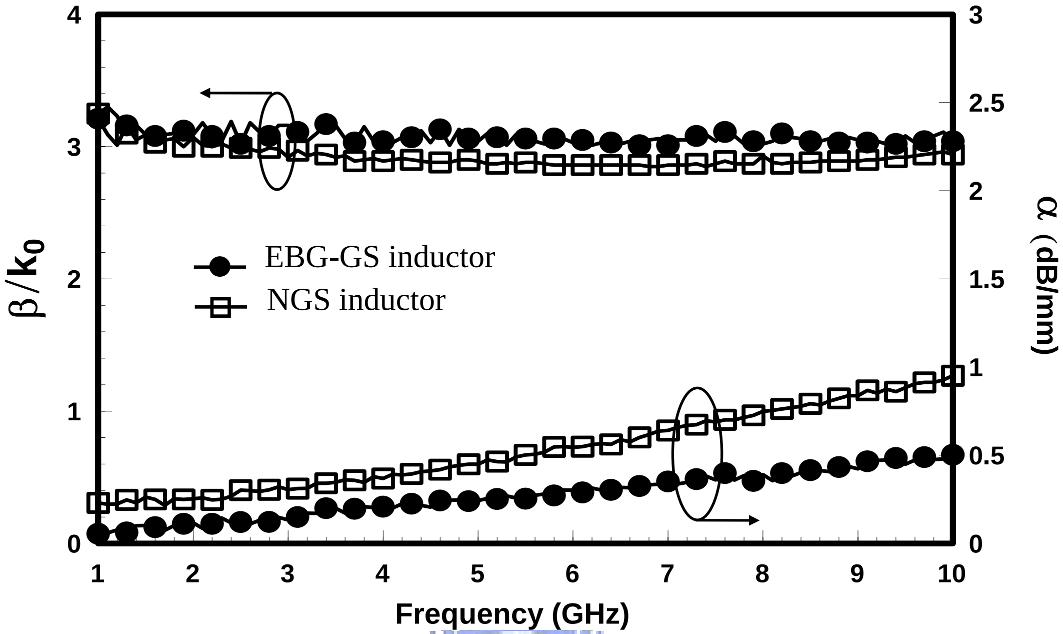

(a)

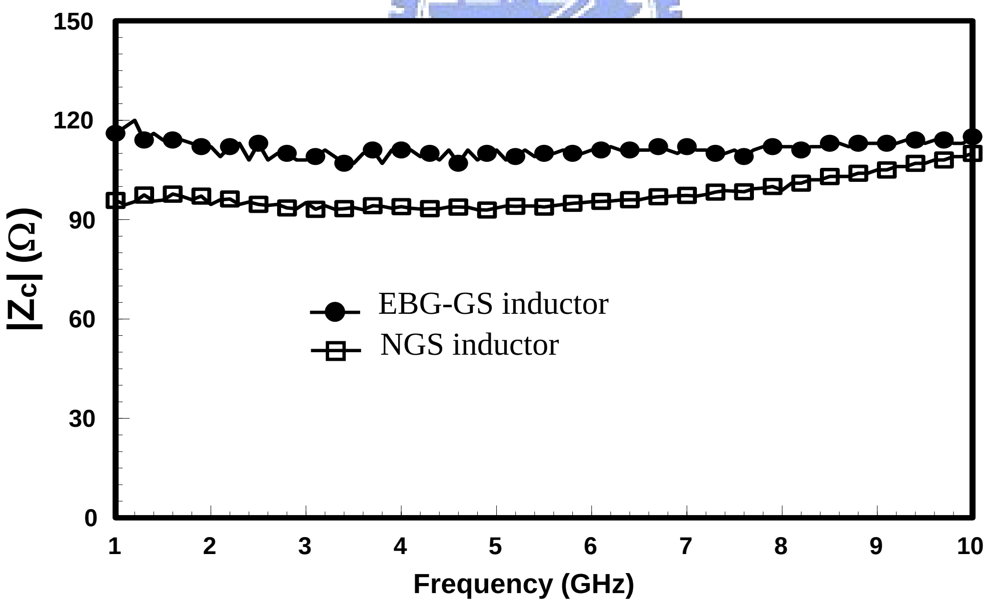

(b)

Fig. 4.10 Equivalent transmission line parameters of the monolithic spiral inductor on the uniform ground plane and EBG ground plane: (a) complex propagation constant, (b) characteristic impedance.

The EBG-GS inductor, therefore, simultaneously achieves increasing Z_c, slow-wave factor (SWF), and decreasing α. Consequently, the lumped model parameters, L_s, R_s, C_p, and R_p are improved. In Fig. 4.11(a), Ls of the PBG-GS inductor was increased by 26.7% over that of the NGS inductor. Notably, the extraction of L_s assumes that C_s is invariant with the inclusion of the EBG ground shield, and is only related to the layout and process parameters. In this work, C_s equals 9fF, the series resistance, R_s, for both EBG-GS and NGS inductors is proportional to the frequency due to the skin effect. Nevertheless, R_s of the EBG-GS inductor is 32% less than that of the NGS inductor due to the disturbance of the eddy current in the former case. The shunt parasitics represent compound effect of oxide capacitance (C_{ox}), substrate capacitance (C_{sub}), and substrate resistance (R_{sub}) that varies markedly with frequency. The shunt resistance, R_p, representing substrate losses, is also increased especially in the lower frequency rang, as depicted in Fig. 4.11 (c). Figure 4.11 (d) shows that the shunt capacitance, C_p, of the EBG-GS inductor is 10% less than that of the NGS inductor at 5GHz. Signifying that the EBG ground shield can prevent energy from penetration into substrates and thus free from coupling between inductor and adjacent circuitry. The overall effect on the inductor's Q-factor is an improvement by 70% at the 5 GHz peak-Q frequency, as shown in Fig. 4.11(e). Thanks to the lower C_p value in the EBG-GS inductor, the roll-off in Q-factor above peak-Q frequency is dramatically alleviated than that in related works on the ground shield. The self-resonant frequency is increased as well.

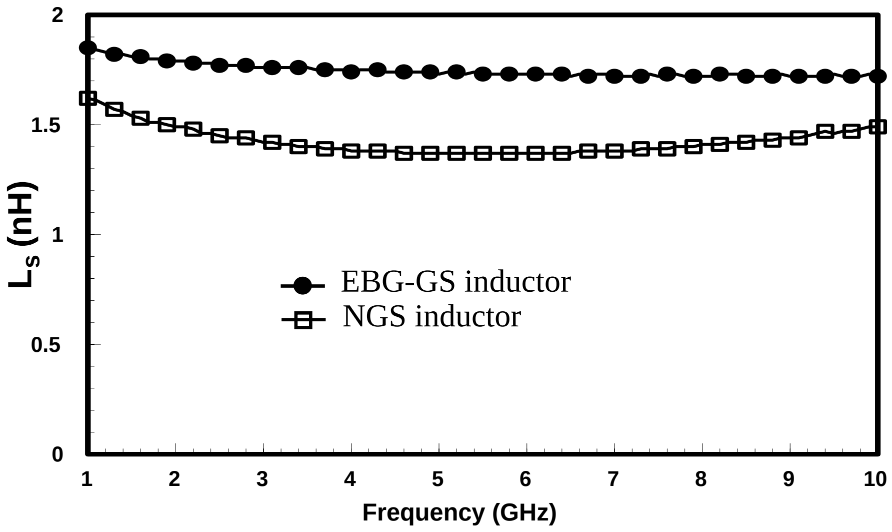

2
1.5
1
0.5
0
L_S (nH)
EBG-GS inductor
NGS inductor
1
2
3
4
5
6
7
8
9
10
Frequency (GHz)

(a)

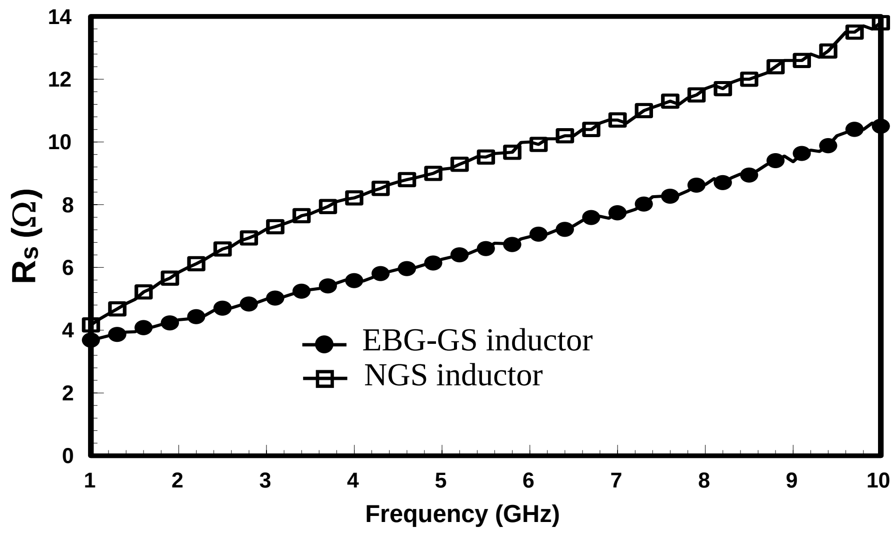

14
12
10
8
6
4
2
0
R_S (Ω)
EBG-GS inductor
NGS inductor
1
2
3
4
5
6
7
8
9
10
Frequency (GHz)

(b)

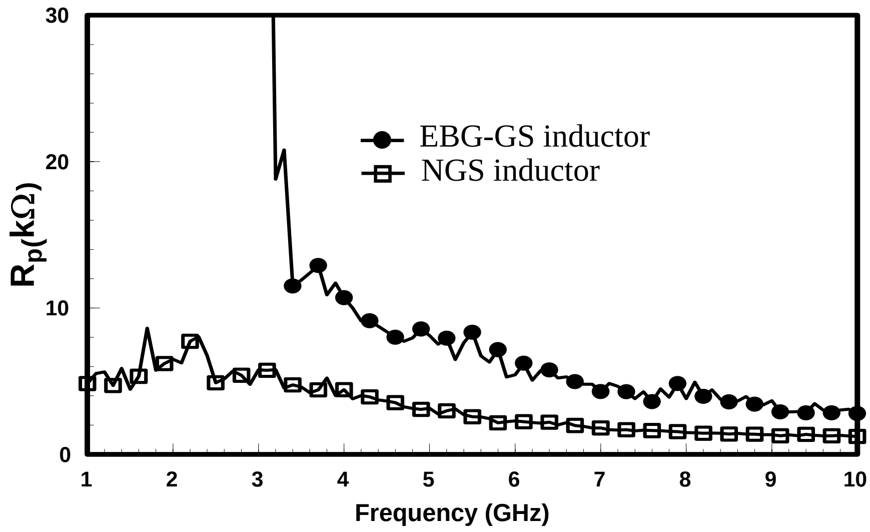

30
20
10
0
R_p(kΩ)
EBG-GS inductor
NGS inductor
1
2
3
4
5
6
7
8
9
10
Frequency (GHz)

(c)

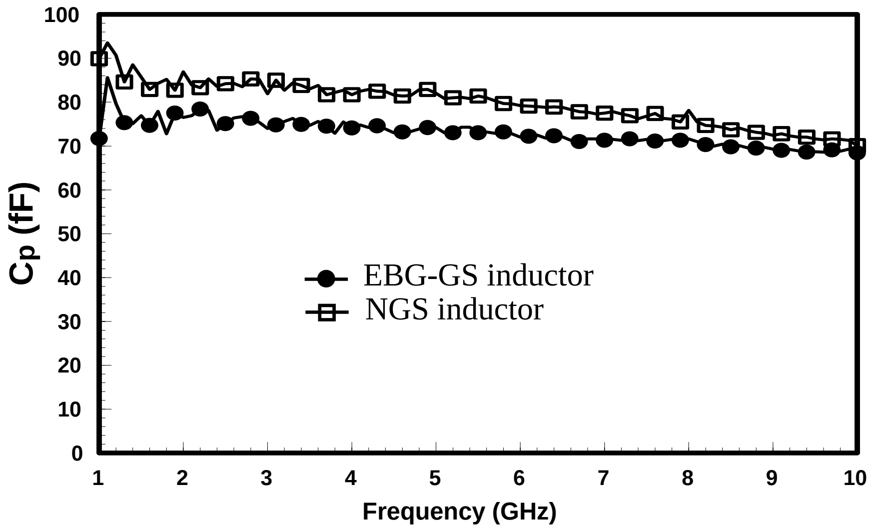

(d)

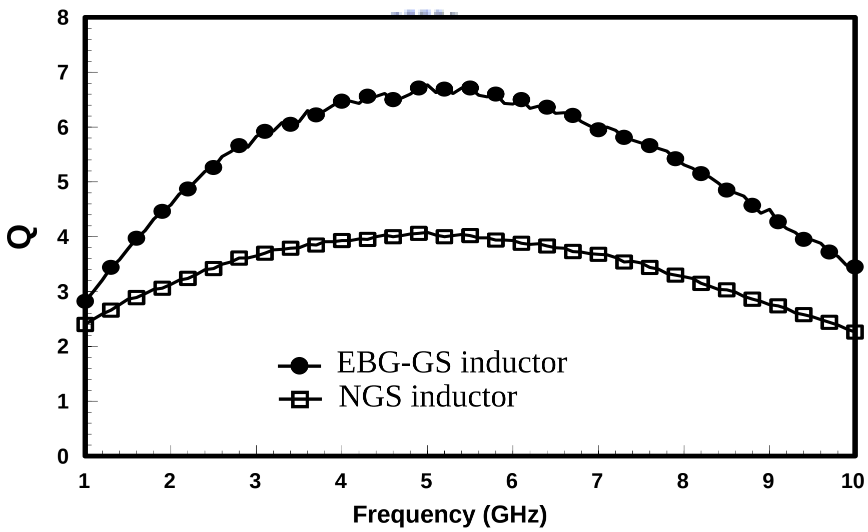

(e)

Fig. 4.11 Measured results for comparing EBG inductor with conventional spiral inductor applying the 0.25um CMOS process: (a) series inductances (L_s), (b) series resistance (R_s), (c) parasitic resistance (R_p), (d) parasitic capacitance (C_p), (e) quality factor (Q).

In summary, this chapter presented and verified a new design methodology to improve the planar spiral inductors incorporating modern fabrication process. Both characteristics and physical insights of inductors on electromagnetic bandgap (EBG) ground plane are analyzed through physically based equivalent circuit model. The experiments are carried out on both print-circuit-board (PCB) and standard CMOS technology without additional process complexity. Measured results show the improvements are in all aspect as excepted, demonstrating the great potential for EBG structure in hybrid or monolithic CMOS RFIC inductor designs. Further optimization in EBG inductor is possible and may lead to better performance in the near future.

CHAPTER 5

Conclusion

This dissertation has investigated the designs and applications of synthetic waveguides. Three kinds of synthetic waveguides are classified and studies individually. This chapter summarizes the major contributions of this work and identifies the future study.

5.1 *Contributions*

- A generalized view of the synthetic waveguides is presented and introduced for the first time in the connection of the global trend on the development of artificial guiding structures.

- Two simplified waveguide models, which associate with two distinct regions of propagation of the EBG surfaces, is presented to illustrate the unique characteristics of synthetic rectangular waveguide (SRW). The slow-wave factor of TE_{10} mode SRW significantly exceeds the theoretical limit of $\sqrt{\varepsilon_r}$ for the conventional metallic rectangular waveguide.

- The propagations of the TM_{00} and TM_{10} modes, which can not exist in the metallic rectangular waveguide, have been theoretically investigated, revealing low-loss, slow-wave guiding characteristics.

- Three waveguide transitions, including the tapered microstrip, the finline, and tapered coplanar waveguide (CPW), are proposed to demonstrate the high level of integration to interface to the corresponding SRW using the same polymer substrates supporting TE_{10}, TM_{00}, and TM_{10} modes.

- A multi-layer guiding system, which is constructed by the stacked complementary conducting strip (CCS) transmission line (TL), is presented. A typical function block, which include a lowpass filter (LPF) and a bandpass filter (BPF), is realized by the proposed guiding architecture, revealing the advantages of high isolation with negligible effects, and compact layout for the system integration.

- A 2.4 GHz transmission-line based BPF is realized by the stacked CCS TL, showing that the filter volume approaches to that of state-of-the-art devices using low temperature cofired ceramic (LTCC) technology.

- A design equation, which illustrates the core technique of incorporating stack CCS TL, is presented. The proposed guiding system can systematically reducing the size of filter based on multi-layer substrate technology, resulting nearly the same volume as the number of substrates is increased.

- An inductor configuration, which incorporates the electromagnetic bandgap (EBG) ground shielding for improving the inductor's characteristics, is presented. A transmission line-based inductor model is presented for illustrating the physical meanings of the proposed configuration.

- The measured results show that the spiral inductors with EBG-shielded can be improved in almost aspects, including higher inductances, higher Q-factor, and lower substrate coupling.

5.2 *Future Works*

This dissertation reports new methodologies of making the synthetic waveguide. The proposed synthetic waveguides have two distinct features. First, well-controlled guiding properties can be easily established and applied to the design of microwave circuits. Second, high level of integration can be achieved for the circuit or system implementations. Such high level of integration using the proposed synthetic waveguides leads to the development of the high performance system-on-chip (SOC) and system-in-package (SIP) as illustrated in Fig. 5.1, which shows that compacted, high-performance RF module and system can be systematically realized by the synthetic waveguide.

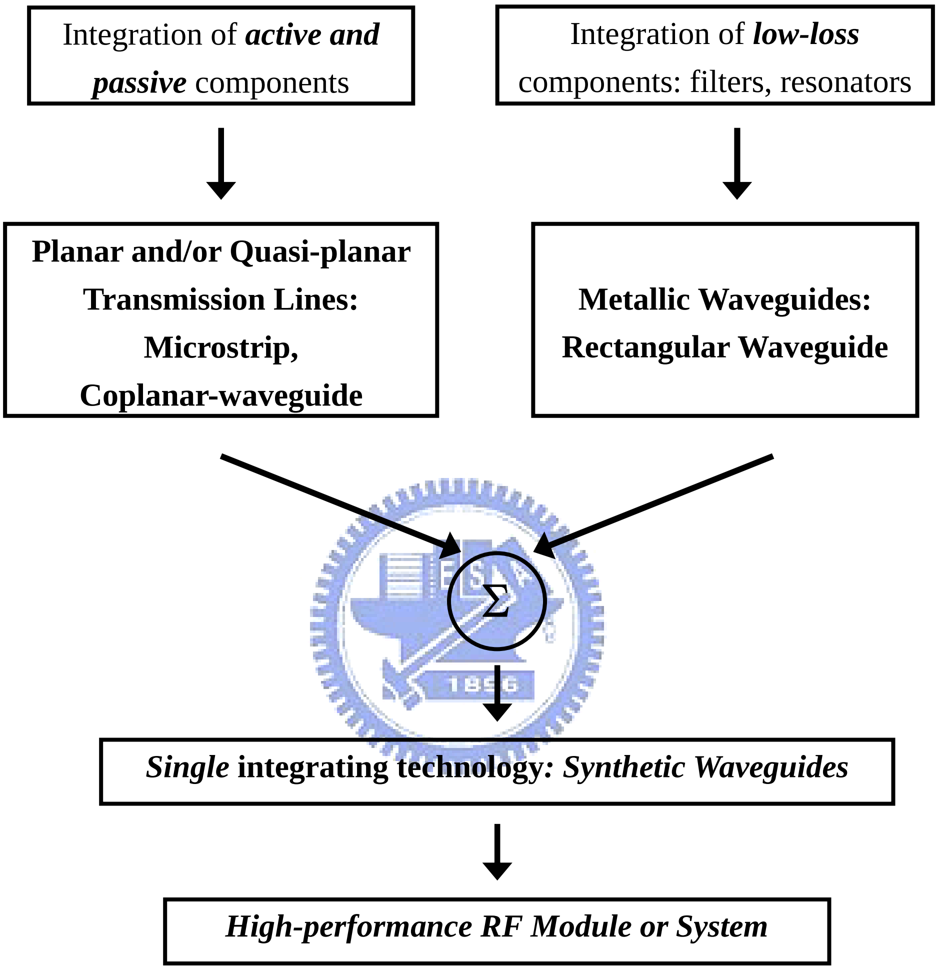

Fig. 5.1 High-performance RF system incorporating synthetic waveguide.

Appendix I
Simplified Waveguide Models for Synthetic Rectangular Waveguide (SRW)

The Cartesian system is applied through the Appendix I. The guide wave is represented using time-harmonic waves, $e^{(j\omega t-\gamma z)}$, with time and distance variations. The propagation constant (γ) is defined by α-$j\beta$. We will assume that there is no net charge density in the dielectric and that any conduction currents are included by allowing permittivity and therefore $k^2=\omega^2\mu\varepsilon$ to be complex. The μ (ε) is the product between μ_0(ε_0) and μ_r(ε_r). The wave equations, which reduce to the Helmholtz equations for phasor fields, are

$$\begin{cases}\nabla^2\mathrm{E} = -k^2\mathrm{E}\\ \nabla^2\mathrm{H} = -k^2\mathrm{H}\end{cases}$$

The three-dimensional ∇^2 may be broken into two parts:

$$\nabla^2 = \nabla_t^2\mathrm{E} + \frac{\partial^2\mathrm{E}}{\partial z^2}$$

With the assumed propagation function $e^{-\gamma z}$ in the axial direction,

$$\frac{\partial^2\mathrm{E}}{\partial z^2} = \gamma^2\mathrm{E}$$

The foregoing wave equations may then be written

$$\begin{cases}\nabla_t^2\mathrm{E} = -(\gamma^2+k^2)\mathrm{E}\\ \nabla_t^2\mathrm{H} = -(\gamma^2+k^2)\mathrm{H}\end{cases}$$

The curl equations with the assumed functions $e^{(j\omega t-\gamma z)}$ are written below for fields in the dielectric system, assumed here to be linear, homogeneous, and isotropic:

$$\begin{cases} \nabla \times \mathrm{E} = -j\omega\mu\,\mathrm{H} \\ \nabla \times \mathrm{H} = j\omega\varepsilon\,\mathrm{E} \end{cases}$$

From the foregoing equations, the E_x, E_y, H_x, H_y can be solved in terms of E_z and H_z.

$$E_x = -\frac{1}{\gamma^2 + k^2}\left(\gamma\frac{\partial E_z}{\partial x} + j\omega\mu\frac{\partial H_z}{\partial y}\right)$$
$$E_y = \frac{1}{\gamma^2 + k^2}\left(-\gamma\frac{\partial E_z}{\partial y} + j\omega\mu\frac{\partial H_z}{\partial x}\right)$$
$$H_x = \frac{1}{\gamma^2 + k^2}\left(j\omega\varepsilon\frac{\partial E_z}{\partial y} - \gamma\frac{\partial H_z}{\partial x}\right)$$
$$H_y = -\frac{1}{\gamma^2 + k^2}\left(j\omega\varepsilon\frac{\partial E_z}{\partial x} + \gamma\frac{\partial H_z}{\partial y}\right)$$

For propagating waves, it is convenient to use the substitution $\gamma = j\beta$ where β is real if there is no attenuation. Rewriting the above with this substitution,

$$E_x = -\frac{j}{k_c^2}\left(\beta\frac{\partial E_z}{\partial x} + \omega\mu\frac{\partial H_z}{\partial y}\right)$$
$$E_y = \frac{j}{k_c^2}\left(-\beta\frac{\partial E_z}{\partial y} + \omega\mu\frac{\partial H_z}{\partial x}\right)$$
$$H_x = \frac{j}{k_c^2}\left(\omega\varepsilon\frac{\partial E_z}{\partial y} - \beta\frac{\partial H_z}{\partial x}\right)$$
$$H_y = -\frac{j}{k_c^2}\left(\omega\varepsilon\frac{\partial E_z}{\partial x} + \beta\frac{\partial H_z}{\partial y}\right)$$
$$\nabla_t^2 E_z = -k_c^2 E_z$$
$$\nabla_t^2 H_z = -k_c^2 H_z$$

where

$$k_c^2 = \gamma^2 + k^2 = k^2 - \beta^2$$

TE$_{np}$ mode:

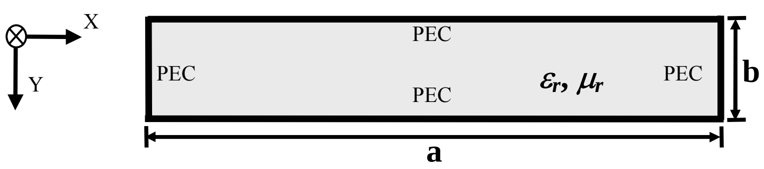

Boundary Conditions:

$$E_y(x=0)=0, E_y(x=a)=0$$
$$E_x(y=0)=0, E_x(y=b)=0$$

The transverse electric waves have zero E_z and nonzero H_z. The wave equations are expressed in Cartesian coordinates:

$$\nabla_t^2 H_z = \frac{\partial^2 H_z}{\partial x^2} + \frac{\partial^2 H_z}{\partial y^2} = -k_c^2 H_z$$

Solution by the separation of variables techniques gives

$$H_z = B' \cos k_x x \cos k_y y$$

where

$$\begin{cases} k_x = n\pi \\ k_y = p\pi \\ B' = B \cdot n\pi \\ k_c^2 = k_x^2 + k_y^2 \end{cases}$$

The forms of transverse electric field in TE$_{np}$ mode are

$$E_x = \frac{j\omega\mu k_y}{k_c^2} B' \cos k_x x \sin k_y y$$
$$E_y = -\frac{j\omega\mu k_x}{k_c^2} B' \sin k_x x \cos k_y y$$

Corresponding transverse magnetic field components are

$$H_x = \frac{j\beta k_x}{k_c^2} B' \sin k_x x \cos k_y y$$
$$H_y = \frac{j\beta k_y}{k_c^2} B' \cos k_x x \sin k_y y$$

Since the proposed SRW is realizable by multi-layered integrated circuit processes, the lateral dimensions (along x-axis) of the SRW are typically much larger than the thickness of the substrate along the y-axis. Consequently, the lowest order TE modes are TE_{10}, and TE_{20}, etc. On the other words, the k_y is assumed to be zero. Therefore, the field components in the transverse and longitudinal directions for the TE_{n0} modes in SRW are

$$E_y = -\frac{j\omega\mu}{k_x} B'\sin k_x x = -\frac{j\omega\mu a}{n\pi} B'\sin\frac{n\pi}{a}x$$
$$H_x = \frac{j\beta}{k_x} B'\sin k_x x = \frac{j\beta a}{n\pi} B'\sin\frac{n\pi}{a}x$$
$$H_z = B'\cos k_x x = B'\cos\frac{n\pi}{a}x$$

By using the substitution $B' = B \cdot n\pi$, the filed components of the TE_{n0} modes in SRW are

$$E_y = -j\omega\mu a B\sin\frac{n\pi}{a}x$$
$$H_x = j\beta a B\sin\frac{n\pi}{a}x$$
$$H_z = B \cdot n\pi \cdot \cos\frac{n\pi}{a}x$$

TM_{mq} mode:

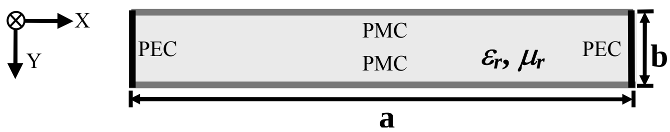

Boundary Conditions:

$$E_z(x=0)=0, E_z(x=a)=0$$
$$E_y(x=0)=0, E_y(x=a)=0$$
$$H_x(y=0)=0, H_x(y=b)=0$$

The transverse magnetic waves have zero H_z and nonzero E_z. The wave equations are expressed in rectangular coordinates:

$$\nabla_t^2 E_z = \frac{\partial^2 E_z}{\partial x^2} + \frac{\partial^2 E_z}{\partial y^2} = -k_c^2 E_z$$

Solution by the separation of variables techniques gives

$$E_z = D' \sin k_x x \cos k_y y$$

where

$$\begin{cases} k_x = m\pi \\ k_y = q\pi \\ D' = D \cdot m\pi \\ k_c^2 = k_x^2 + k_y^2 \end{cases}$$

The forms of transverse electric field in TE_{np} mode are

$$E_x = -\frac{j\beta k_x}{k_c^2} D' \cos k_x x \cos k_y y$$
$$E_y = \frac{j\beta k_y}{k_c^2} D' \sin k_x x \sin k_y y$$

Corresponding transverse magnetic field components are

$$H_x = -\frac{j\omega\varepsilon k_y}{k_c^2} D' \sin k_x x \sin k_y y$$
$$H_y = -\frac{j\omega\varepsilon k_x}{k_c^2} D' \cos k_x x \cos k_y y$$

Since the proposed SRW is realizable by multi-layered integrated circuit processes, the lateral dimensions (along x-axis) of the SRW are typically much larger than the thickness of the substrate along the y-axis. Consequently, the lowest order TM modes are TM_{00}, and TM_{10}, etc. On the other words, the k_y is assumed to be zero. Therefore, the field components in the transverse and longitudinal directions for the TM_{m0} modes in SRW are

$$E_x = -\frac{j\beta}{k_x} D' \cos k_x x = -\frac{j\beta a}{m\pi} D' \cos \frac{m\pi}{a} x$$

$$H_y = -\frac{j\omega\varepsilon}{k_x} D' \cos k_x x = \frac{j\omega\varepsilon a}{m\pi} D' \cos \frac{m\pi}{a} x$$

$$E_z = D' \sin k_x x = D' \sin \frac{m\pi}{a} x$$

By using the substitution $D' = D \cdot m\pi$, the filed components of the TM_{m0} modes in SRW are

$$E_x = -j\beta a D \cos \frac{m\pi}{a} x$$

$$H_y = j\omega\varepsilon a D \cos \frac{m\pi}{a} x$$

$$E_z = D \cdot m\pi \cdot \sin \frac{m\pi}{a} x$$

Appendix II

Volume Estimation for Transmission-Line Based Bandpass Filter incorporating Multi-layer Complementary Conducting Strip Transmission Line (CCS TL)

As shown in the Figure 3.11, the complete bandpass filter (BPF) including the parallel resonators and *J*-inverters can be realized using complementary conducting strip transmission line (CCS TL). Moreover, the placement of the CCS TL is mainly controlled by the period (P) of the unit cell and its connection with the adjacent cells. Following the design procedure reported in the Section 3.2.2, the required electrical parameters including the characteristic impedances and electrical lengths for the TL-based BPF are given. Since the CCS TL can provide much more design solutions to meet the specified guiding characteristics of the TLs in BPF. For simplicity, the period of all the unit cells is identical. Therefore, the volume estimation of TL-based BPF using CCS TL is initially given by

$$\mathrm{V}_{\mathrm{total}} = L_t \cdot P \cdot (2N - 1) \cdot h \tag{II.1}$$

where $\mathrm{V}_{\mathrm{total}}$, L_t, N and h are followed by the same definitions reported in the Section 3.4. If N equals to one, on the other word, the BPF is realized by conventional double-side print-circuit-board (PCB) with one signal layer and the total area of the BPF is proportional to the product of the period of the unit cell (P) and the total lengths (L_t) required by the filter design parameters.

Furthermore, applying the multi-layer complementary conducting strip transmission line (CCS TL), which provides more than one signal layer to realize the TL-based BPF, the required volume of the TL-BPF can be expressed by the following equation:

$$\mathrm{V}_{\mathrm{total}} = \frac{L_t \cdot P}{N} \cdot (2N - 1) \cdot h \qquad \text{(II.2)}$$

Notably (II.2) reveals an intrinsic assumption that the area of each signal layer is fully occupied by the signal trace of the meandered CCS TL. After some algebraic manipulation, a estimate of volume for TL-based BPF incorporating multi-layer CCS TL is give by:

$$\mathrm{V}_{\mathrm{total}} = L_t \cdot P \cdot (2 - \frac{1}{N}) \cdot h \qquad \text{(II.3)}$$

Appendix III

Equivalent Transmission-Line Model for Spiral Inductor

In this appendix, the mathematic derivations for representing the lumped inductor model using equivalent transmission line parameters are illustrated. What follows is the comparison of one-port input impedances between two models. One is the generic lumped spiral inductor model and the other one is the generalized transmission-line model. During the derivations, the definitions of voltage-drop and current-flow in two models are identical.

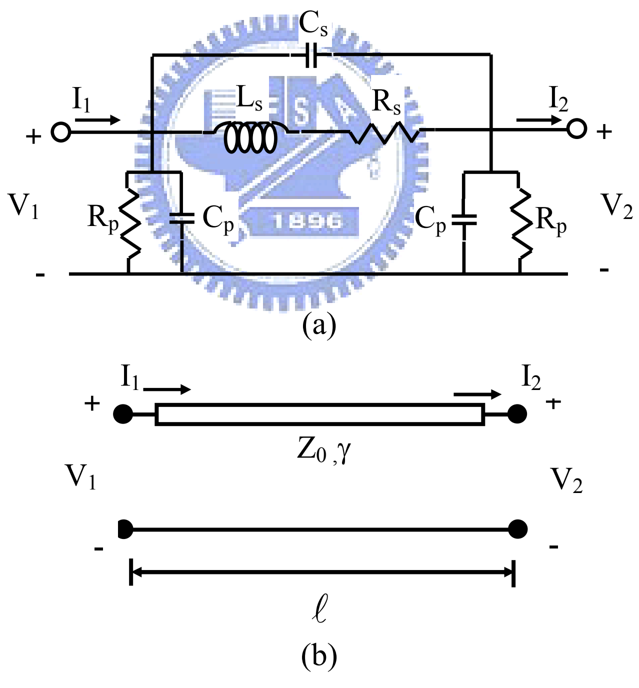

Fig. III.1 Equivalent model for representing spiral inductor: (a) generic lumped model, (b) transmission-line model

The two-port transmission matrix of the transmission line can be expressed in terms of transmission line parameters.

$$\begin{bmatrix} A & B \\ C & D \end{bmatrix} = \begin{bmatrix} \cosh\gamma\ell & Z_0 \sinh\gamma\ell \\ Z_0^{-1}\sinh\gamma\ell & \cosh\gamma\ell \end{bmatrix}$$

Notably, the characteristic impedance (Z_0) and propagation constant (γ) are all complex number for representing the losses of the transmission line. Next, the input admittance of the transmission line with short termination is proportional to the ratio between D and B and can be expressed in the following equation.

$$\begin{aligned}
\left.\frac{I_1}{V_1}\right|_{V_2=0} &= \frac{D}{B} \\
&= \frac{\cosh\gamma\ell}{Z_0 \sinh\gamma\ell} \\
&= \frac{1}{Z_0}\cdot\left(\frac{e^{\gamma\ell}+e^{-\gamma\ell}}{e^{\gamma\ell}-e^{-\gamma\ell}}\right) \\
&= \frac{1}{Z_0}\cdot(1+2e^{-2\gamma\ell}+2e^{-4\gamma\ell}+2e^{-6\gamma\ell}+\ldots) \\
&= \frac{1}{Z_0}\cdot\frac{(1+\gamma\ell+\frac{(\gamma\ell)^2}{2!}+\ldots)+(1-\gamma\ell+\frac{(\gamma\ell)^2}{2!}-\ldots)}{(1+\gamma\ell+\frac{(\gamma\ell)^2}{2!}+\ldots)-(1-\gamma\ell+\frac{(\gamma\ell)^2}{2!}-\ldots)} \qquad \text{assumeing } |\gamma\ell| << 1 \\
&\approx \frac{1}{Z_0}\cdot\frac{2+(\gamma\ell)^2}{2\gamma\ell} \\
&= \frac{1}{Z_0}\cdot\left(\frac{1}{\gamma\ell}+\frac{\gamma\ell}{2}\right) \\
&= \frac{1}{\gamma\ell Z_0}+\frac{1}{\frac{2Z_0}{\gamma\ell}}
\end{aligned}$$

Then, the input admittance of transmission line with short termination can be directly mapped to those of the lumped model as shown in Fig. III.1. Therefore, the elements in the lumped model can be expressed in terms of the equivalent transmission lime parameters including the physical length, the characteristic impedance and propagation constant of the transmission line.

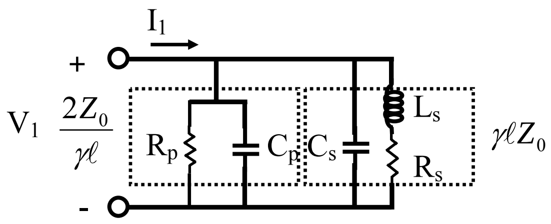

Notably, by doing the Taylor's series expansion, the product of $\gamma\ell$ is assumed to be less than one for simplifying the mathematic expressions during the derivations. This assumption also limits the usage of derivations.

REFERENCE

[1] Wim Diels, Kristof Vaesen, Piet Wambacq, Stéphane Donnay, Walter De Raedt Marc Engels, and Ivo Bolsens, “Single-package integration of RF blocks for a 5GHz WLAN application,” *IEEE Trans. Advance Packaging*, vol. 24, no. 3, pp. 384-391, Aug. 2001.

[2] Chang-Ho Lee, Albert Sutono, Sangwoo Han, Kyutae Lim, Stéphane Pinel, Emmanouil M. Tentzeris, and Joy Laskar, “A compact LTCC-based Ku-band transmitter module,” *IEEE Trans. Advance Packaging*, vol. 25, no. 3, pp. 374-384, Aug. 2002.

[3] Julien Ryckaert, Steven Brebels, Boris Come, Wim Diels, Dries Hauspie, Serguei Stoukatch, Kristof Vaesen, Walter De Raedt, and Stephane Donnay,” Single-package 5 GHz WLAN RF module with embedded patch antenna and 20 dBm power amplifier,” *2003 IEEE MTT-S International Microwave Symp. Dig.*, pp. 1037-1040, 2003.

[4] Yo-Shen Lin, Chien-Chang Liu, Ko-Mai Li, and Chun Hsiung Chen, “Design of an LTCC tri-band transceiver module for GPRS mobile applications,” *IEEE Trans. Microwave Theory and Tech.*, vol. 52, no. 12, pp. 2718-2724, Dec. 2004.

[5] Manos M. Tentzeris, Joy Laskar, John Papapolymerou, Stéphane Pinel, V. Palazzari, R. Li, G. Dejean, N. Papageorgiou, D. Thompson, R. Bairavasubramanian, S. Sarkar, and J.-H. Lee, “3-D-integrated RF and millimeter-wave functions and modules using liquid crystal polymer (LCP) system-on-package technology, “ *IEEE Trans. Advance Packaging*, vol. 27, no. 2, pp. 332-340, May 2004.

[6] Alexander Chernyakov, Konstantin Markov, Denys Orlenko, Patric Heide, and Clemens Ruppel, “Miniature fully-integrated WLAN frontend-modules based on LTCC technology,” *2004 IEEE MTT-S International Microwave Symp. Dig.*, pp. 139-142, 2004.

[7] Albert Chee W. Lu, Kai M. chua, Lai L. Wai, Stephen C. K. Wong, Jun J. Wang, and Y. P. Zhang, “Integrated antenna module for broadband wireless applications,” *2004 Electronics Packaging Tech. Conf.*, pp. 240-243, 2004.

[8] Cheng-Jung Lee, Tsai-Pi Hung, Shao-Cheng Lin, Hsien-Shun Wu, Chang-Yi Tsai, Kuo-Feng Hung, Yu-Chiao Chen, Wen-Chang Lee, and Ching-Kuang C. Tzuang, "A fully all-planar integrated Ka-band FSK transceiver module,” *2001 Asia-Pacific Microwave Conference Proceedings*, pp. 1084-1087, 2001.

[9] Hsien-Hsuen Wu, Ching-Jung Peng, Wen-Chang Lee, Chia-Min Lin, Ho-Chung Chen, Mei-Chien Chen, Shao-Cheng Lin, Tsai-Pi Hung, Cheng-Jung Lee, and Ching-Kuang C. Tzuang, “All-Planar Millimeter-Wave WLAN Transceiver,” *Technical Digest of the 2002 Topical Symposium on Millimeter-Waves*, pp. 61-64, 2002.

[10] B. Lakshminarayanan, and T. Weller, “Reconfigurable mems transmission lines with independent Z_0 -and β- tuning, “2005 *IEEE MTT-S International Microwave Symp.*

TH2F-1, Long Beach, CA, 2005.

[11] Zhang Cheng Hao, Wei Hong, JiXin Chen, XiaoPing Chen, and Ke Wu, "A novel feeding techniques for antipodal linearly tapered slot antenna array," 2005 *IEEE MTT-S International Microwave Symp.* TH2F-2, Long Beach, CA, 2005.

[12] L. Mercier, M. Thévenot, A. Crunteanu, B. Jecko, J. C. Orlienyes, C. Champeaux, A. Caterinot, and P. Blondy, "Design and measurement of a smart tunable periodic material," 2005 *IEEE MTT-S International Microwave Symp.* TH2F-3, Long Beach, CA, 2005.

[13] Sen Wang, Hsien-Shun Wu, and Ching-Kuang C. Tzuang, "Propagation characteristics of wide synthetic quasi-TEM transmission line," 2005 *IEEE MTT-S International Microwave Symp.* TH2F-4, Long Beach, CA, 2005.

[14] Kaixue Ma, Jianguo Ma, Manh Anh do, and Kiat Seng Yeo, "Experimentally investigating slow-wave transmission lines and filters based on conductor-backed CPW periodic cells, "2005 *IEEE MTT-S International Microwave Symp.* TH2F-5, Long Beach, CA, 2005.

[15] F. R. Yang, Y. Qian, R. Coccioli, and T. Itoh, "A novel low-loss slow-wave microstrip structure," *IEEE Microwave Guided Wave Lett.*, vol 8, no 11, pp. 372-374, Nov. 1998.

[16] C. K. Wu, Hsien-Shun Wu, and Ching-Kuang C. Tzuang, "Electric-magnetic-electric (EME) slow-wave microstrip line and bandpass filter of compressed size," *IEEE Transaction on Microwave Theory and Techniques*, vol 50, no 8, pp. 1996-2004, Aug. 2002.

[17] F.-R. Yang, K.-P. Ma, Y. Qian, and T. Itoh, "Uniplanar Compact Photonic-Bandgap (UC-PBG) structure and its applications for microwave circuits," *IEEE Trans. Microwave Theory Tech.*, vol. 47, no. 8, pp. 1509–1514, Aug. 1999.

[18] C. K. Wu, and Ching-Kuang C. Tzuang, "Slow-wave propagation of microstrip consisting of electric-magnetic-electric (EME) composite metal strips, "2001 *IEEE MTT-S International Microwave Symp. Dig.*, pp. 727-730, 2001.

[19] Y. C. Chen, C. K. Wu, and Ching-Kuang C. Tzuang, "Dual-frequency electric-magnetic-electric microstrip leaky-mode antenna of a single fan beam," *IEEE Trans. Microwave Theory Tech.*, vol. 50, no. 12, pp. 2713–2720, Dec. 2002.

[20] V. Veselago, "The electrodynamics of substances with simultaneously negative values of ε and μ, "Soviet Physics Uspekhi, vol. 10, no. 4, pp. 509-514, 1968.

[21] S. Ramo, L. R. Whinnery, and T. Van Duzer, *Fields and Waves in Communication Electronics*, 2nd ed. New York: Wiley, 1984.

[22] R. A. Shelby, D. R. Smith, and S. Schultz, "Experimental verification of a negative index of refraction," *Science*, vol. 292, no. 5514, pp. 77-79, 2001.

[23] J. D. Baena, R. Marqués, J. Martel, and F. Medina, "Experimental results on metamaterial simulation using SRR-loaded waveguides, "2003 *IEEE MTT-S International Antenna Propag. Symp. Dig.*, pp. 106-109, 2003.

[24] J. Bonache, F. Martin, F. Falcone, J. García, I. Gil, T. Lopetegi, M. A. G. Laso, R. Marqués, F. Medina, M. Sorolla, “Super compact split ring resonators CPW band pass filters,” 2004 *IEEE MTT-S International Microwave Symp. Dig.*, pp. 1483-1486, 2004.

[25] C. Caloz, H. Okabe, T. Iwai, and T. Itoh, “Transmission line approach of left-handed (LH) materials, “ in Proc. *USNC/USRI National Radio Science Meeting*, San Antonio, TX, June 2002, vol. 1, p39.

[26] C. Caloz, and T. Itoh, *Electromagnetic Metamaterials: Transmission Line Theory and Microwave Applications*. New York: Wiely, 2004.

[27] A. Sanada, C. Caloz and T. Itoh, “Planar distributed structures with negative refractive properties, “*IEEE Trans. Microwave Theory Tech.*, vol. 52, no. 4, pp. 1254–1263, April 2004.

[28] H. Okabe, C. Caloz, and T. Itoh, “A compact enhanced-band-width hybrid ring using an artificial lumped-element left-handed transmission-line section, “*IEEE Trans. Microwave Theory Tech.*, vol. 52, no. 3, pp. 798–804, March 2004.

[29] C. Caloz, A. Sanada, and T. Itoh, “A novel composite right/left-handed coupled-line directional coupler with arbitrary coupling level and broad bandwidth, “*IEEE Trans. Microwave Theory Tech.*, vol. 52, no. 3, pp. 980–992, March 2004.

[30] I. Lin, M. DeVincentis, C. Caloz, and T. Itoh, “Arbitrary dual-band components using composite right/left-handed transmission lines,” *IEEE Trans. Microwave Theory Tech.*, vol. 52, no. 4, pp. 1142–1149, April 2004.

[31] Lim Sungjoon, C. Caloz, and T. Itoh, “Metamaterial-based electronically controlled transmission-line structure as a novel leaky-wave antenna with tunable radiation angle and beamwidth, “*IEEE Trans. Microwave Theory Tech.*, vol. 52, no. 12, pp. 2678–2690, Dec. 2004.

[32] Y. Horii, C. Caloz, and T. Itoh, “Super-compact multilayered left-handed transmission line and diplexer application,” *IEEE Trans. Microwave Theory Tech.*, vol. 53, no. 4, pp. 1527–1534, April 2005.

[33] Ansoft corporation, *Getting Started: An Eigenmode Problem*, Jan. 2001, page 6-5, Ansoft^{TM}.

[34] Dan Sievenpiper, Lijun Zhang, Romulo F. Jimenez Broas, Nicholas G. Alexópolous, Eli Yablonovitch, “High-impedance electromagnetic surfaces with a forbidden frequency band,” *IEEE Trans. Microwave Theory and Tech.* vol. 47, no. 11, pp.2059-2074, Nov. 1999.

[35] Fei-Ran Yang, Kuang-Ping Ma, Yongxi Qian, Tatsuo Itoh, ”A novel TEM waveguide using uniplanar compact photonic-bandgap (UC-PBG) structure,” *IEEE Trans. Microwave Theory and Tech.* vol. 47, no. 11, pp.2092-2098, Nov. 1999.

[36] J M. Kim, J. B. Hacker, A. L. Sailer, S. Kim, D. Sievenpiper, J. A. Higgins, “A rectangular TEM waveguide with photonic crystal walls for excitation of quasi-optical amplifiers,” 1999 *IEEE MTT-S International Microwave Symp. Dig.*, pp. 543~546, Anaheim, CA, 1999.

[37] Malcolm Ng Mou Kehn, Per-Simon Kildal, “The N-guide: a novel miniaturized hard quasi-TEM waveguide,” *IEEE Antennas Propagat. Int. Symposium*, pp.1111-1114, 2003.

[38] Simon Ramo, John R. Whinnery, Theodore Van Duzer, *Fields and Waves in Communication Electronics*, 3rd, Canada: John Wiley &Sons Inc., pp.417-428, 1994.

[39] Yu-Chiao Chen, Ching-Kuo Wu, Ching-Kuang C. Tzuang,” Dual-frequency electric-magnetic-electric microstrip leaky-mode antenna of a single fan beam,” *IEEE Trans. Microwave Theory and Tech.* vol. 50, no. 12, pp.2713-2720, Dec. 2002.

[40] Ching-Kuang C. Tzuang, Kuo-Chent Chen, Cheng-Jung Lee, C. C. Ho, Hsien-Shun, Wu, ”H-plane mode conversion and application in printed microwave integrated circuit,” *Proc. Eur. Microwave Conf.*, pp.37-40, Oct. 2000.

[41] Cheng-Jung Lee, Hsien-Shun Wu, Ching-Kuang C. Tzuang,”A broadband microstrip-to-waveguide transition using planar technique,” *2001 Asia-Pacific Microwave Cone. Dig.*, pp.543-546, 2001.

[42] Nitin Jain, Noyan Kinayman, Eswarappa Channabasappa, “Integrated HMIC planar rectangular-waveguide,” 2003 *Progress in Electromagnetics Research Sympos.*, Singapore, p34, Jan. 2003.

[43] Ho-Chung Chen, Ching-Kuang C. Tzuang,”All-planar dual-mode asymmetric filters at Ka-band,” *IEEE Microwave and Wireless Components Lett.*, vol. 13, no. 3, pp. 111-113, March 2003.

[44] Wen-Chang Lee, Shao-Cheng Lin, Ching-Kuang C. Tzuang,” Planar realization of low phase noise 15/30 GHz oscillator/doubler using surface mount transistors,” *IEEE Microwave and Wireless Components Lett.*, vol. 13, no. 1, pp. 10-12, Jan. 2003.

[45] David M. Pozar, *Microwave Engineering*, 2nd, Canada: John Wiley &Sons Inc., 1998.

[46] Hsien-Shun Wu, Ching-Kuang C. Tzuang, “Miniaturized Synthetic Rectangular Waveguide,” *2003 IEEE MTT-S International Microwave Symp. Dig.*, pp. 1099-1102, WE2D-1, Philadelphia, Pennsylvania, 2003.

[47] Yu-Chiao Chen, Ching-Kuo Wu, Ching-Kuang C. Tzuang,” Dual-frequency electric-magnetic-electric microstrip leaky-mode antenna of a single fan beam,” *IEEE Trans. Microwave Theory and Tech.* vol. 50, no. 12, pp. 2713-2720, Dec. 2002.

[48] Ching-Kuo Wu, Hsien-Shun Wu, Ching-Kuang C. Tzuang,” Electric-magnetic-electric slow-wave microstrip line and bandpass filter of compressed size,” *IEEE Trans. Microwave Theory and Tech.* vol. 50, no. 8, pp. 1996-2004, Aug. 2002.

[49] Ching-Kuang C. Tzuang, Kuo-Chent Chen, Cheng-Jung Lee, C. C. Ho, Hsien-Shun Wu, ”H-plane mode conversion and application in printed microwave integrated circuit,” *Proc. Eur. Microwave Conf.*, pp. 37-40, Oct. 2000.

[50] Cheng-Jung Lee, Hsien-Shun Wu, Ching-Kuang C. Tzuang," A broadband microstrip-to-waveguide transition using planar technique," *Proc. Of 2001 Asia-Pacific Microwave Cone. Dig.*, pp. 543-546, 2001.

[51] A. Oliner, "The impedance properties of narrow radiating slots in the broad face of rectangular waveguide Part I – Theory," *IRE Trans. On Antennas and Propagation.* pp. 4-11, Jan. 1957.

[52] Chih-Chiang Chen and Ching Kuang C. Tzuang, "Synthetic Quasi-TEM Meandered Transmission Lines for Compacted Microwave Integrated Circuits," *IEEE Transaction on Microwave Theory and Techniques*, vol. 52, no. 6, pp. 1637-1647, June 2004.

[53] G. L. Matthaei, L. Young, E. M. T. Jones, *Microwave Filters, Impedance-Matching Networks, and Coupling Structure*s. Dedham, MA: Artech House, 1980.

[54] Cédric Quendo, Eric Rius, Christian Person, " Narrow bandpass filters using dual-behavior resonators," *IEEE Trans. Microwave Theory & Tech.*, vol. 51, no. 3, pp. 734-743, March 2003.

[55] Cédric Quendo, Eric Risu, Christian Person, "Narrow bandpass filters using dual-behavior resonators based on stepped-impedance stubs and different-length stubs," *IEEE Trans. Microwave Theory & Tech.*, vol. 52, no. 3, pp. 1034-1044, March 2004.

[56] Gaëtan Prigent, Eric Rius, François Le Pennec, Sandrick Le Maguer, Cédric Quendo, Gonzague Six, Henri Happy, " *IEEE Trans. Microwave Theory & Tech.*, vol. 52, no. 3, pp. 1045-1051, March 2004.

[57] Hsien-Shun Wu, Raymond H. Yang, Ching-Kuang C. Tzuang," Synthesis of quasi-elliptical fishbone bandpass filter," in *Proc. Asia Pacific Microwave Conf.*, India, 2004.

[58] *LFB182G45SG9A246*, Murata Manufacturing Co. Available:
http://www.murata.com/.

[59] *DEA202450BT-1213C1*, TDK Co. of America. Available:
http://www.component.tdk.com/.

[60] *LTF2012B-F2R4B*, TOKO America Inc.. Available:
http://www.tokoam.com/.

[61] *BF2012-F2R4DAA*, Advanced Ceramic X Co.. Available :
http://www.acxc.com.tw/.

[62] *2450BP15B100*, Johanson Technology Inc.. Available :
http://www.johansontechnology.com/.

[63] Tatsuya Tsujiguchi, Haruo Matsumoto, Toshio Nishikawa, "A miniaturized double-surface CPW bandpass filter improved spurious responses," *IEEE Trans. Microwave Theory and Tech.*, vol. 49, vo. 5, pp. 879-885, May 2001.

[64] *DEA252450BT-2027A1*, TDK Co. of America. Available:
http://www.component.tdk.com/.

[65] *BF3216-B2R4BAA*, Advanced Ceramic X Co. Available: http://www.acxc.com.tw/.

[66] Lap Kun Yeung, Ke-Li Wu, "A compact second-order LTCC bandpass filter with two finite transmission zeros," *IEEE Trans. Microwave Theory and Tech.*, vol. 51, no. 2, pp. 337-341, Feb. 2003.

[67] *2450BP18C100D*, Johanson Technology Inc.. Available : http://www.johansontechnology.com/.

[68] *B69812N2457C101*, EPCOS. Available: http://www.epcos.com/web/home/html/home_e.html.

[69] Ching-Wen Tang, Yin-Ching Lin, Chi-Yang Chang, "Realization of transmission zeros in combline filters using an auxiliary inductively coupled ground plane," *IEEE Trans. Microwave Theory and Tech.*, vol. 51, no. 10, pp. 2112-2118, Oct. 2003.

[70] Ching-Wen Tang, "Harmonic-suppression LTCC filter with the step-impedance quarter-wavelength open stub," *IEEE Trans. Microwave Theory and Tech.*, vol. 52, no. 2, pp. 617-624, Feb. 2004.

[71] *LFS2450-01BB-C*, NTK Technologies Inc.. Available: http://www.ntktech.com/.

[72] *LFB322G45SN1A504*, Murata Manufacturing Co. Available: http://www.murata.com/.

[73] Y. W. Kong, S. T. Chew, "EBG-based dual mode resonator filter," *IEEE Microwave and Wireless Components Lett.*, vol. 14, no.3, pp. 124-126, March 2004.

[74] Yu-Kang Kuo, Chi-Hsueh Wang, Chun Hsiung Chen, "Novel reduced-size coplanar-waveguide bandpass filters," *IEEE Microwave and Wireless Components Lett.*," vol. 14, no.3, pp. 65-67, Feb. 2001.

[75] Jen-Tsai Kuo, Ming-Jyh Maa, Ping-Han Lu, "A microstrip elliptic function filter with compact miniaturized hairpin resonators," *IEEE Microwave and Wireless Components Lett.*," vol. 10, no.3, pp. 94-95, March 2000.

[76] Kao-Cheng Huang, David Hyland, Alan Jenkins, David Edwards, David Dew-Hughes, "A miniaturized interdigital microstrip bandpass filter," *IEEE Trans. Applied Superconductivity*, vol. 9, no. 2, pp. 3889-3892, June 1999.

[77] Gilbert Siy Ching,"Design and practical implementation of a 2.4 GHz lumped element elliptic bandpass filter," in *Proc. Asia Pacific Microwave Conf.*, Taipei, 2001, pp. 523-526.

[78] Adnan Görür, "Description of coupling between degenerate modes of a dual-mode microstrip loop resonator using a novel perturbation arrangement and its dual-mode bandpass filter applications," *IEEE Trans. Microwave Theory and Tech.*, vol. 52, no. 2, pp. 671-677, Feb. 2004.

[79] Lei Zhu, Boon Chai Tan," Miniaturized dual-mode bandpass filter using inductively loaded cross-slotted patch resonator," *IEEE Microwave and Wireless Components Lett.*, vol. 15, no.1, pp. 22-24, Jan. 2005.

[80] M. G. Banciu, R. Ramer, A. Ioachim,” Compact microstrip resonators for 900MHz frequency band,” *IEEE Microwave and Wireless Components Lett.,*” vol. 13, no.5, pp. 175-177, May 2003.

[81] Jiafeng Zhou, Michael J. Lancaster, Frederick Huang,” HTS coplanar meander-line resonator filters with a suppressed slot-line mode,” *IEEE Trans. Applied Superconductivity*, vol. 14, no. 1, pp. 28-32, March 2004.

[82] Kamran Entesari, Tauno Vaha-Heikkila, Gabriel M. Rebeiz,” Miniaturized differential filters for C- and Ku-band applications,” *Proc. European Microwave Conf.*, Munich, 2003, pp. 227-230.

[83] Erwan Goron, Jean Philippe Coupez, Christian Person, Yann Toutain, Hervé Lattard, Frédéric Perrot,” Accessing to UMTS filtering specifications using new microstrip miniaturized loop-filters,” *2003 IEEE MTT-S International Microwave Symp. Dig.*, pp. 1599-1602.

[84] Norimasa Ishitobi, Eriko Ajioka, Toshiyuki Abe, Hideaki Ninomiya,” The improvement of miniaturized multilayer ceramic band-pass filter,” *1999 IEEE MTT-S International Microwave Symp. Dig.*, pp. 1343-1346.

[85] J. S. Hong, M. J. Lancaster, “Recent advances in microstrip filters for communications and other applications,” *1997 IEE Advances in Passive Microwave Comp. Dig.*, pp. 2/1-2/6.

[86] Raymond S. Kwok, S. Jerry Fiedziuszko, Félix A. Miranda, Giadira V. Leon, Melanie S. Demo, Donna Y. Bohman, “Miniaturized HTS/dielectric multilayer filters for satellite communications,” *IEEE Trans. Applied Superconductivity*, vol. 7, no. 2, pp. 3706-3709, June 1997.

[87] Hui-Kai Zeng, Anting Hsiao, Wei-Hsiu Hsu, Shao-Wei Wu, Jiunn-Yuan Lin, Kaung-Hsiung Wu, Jenh-Yih Juang, Tseng-Ming Uen, Yi-Shun Gou, Jen-Tsai Kuo,” Miniaturized 3 GHz cross-coupled planar microwave filters,” *IEEE Trans. Applied Superconductivity*, vol. 14, no. 1, pp. 107-111, March 2004.

[88] Chul-Soo Kim, Jong-Sik Lim, Jong-Hwa Kim, Dal Ahn, “A design of a miniaturized 2-pole bandpass filter by using a slot and a hair-pin line,” *2004 IEEE MTT-S International Microwave Symp. Dig.*, pp. 1983-1986, 2004.

[89] Yann Toutain, Jean-Philippe Coupez, Christian Person,” Microstrip miniaturized loop-filters with high out-of-band rejection for future 3G mobile terminals,” *2001 IEEE MTT-S International Microwave Symp. Dig.*, pp. 1589-1592, 2001.

[90] Sheng-Yuan Lee, Chih-Ming Tsai,” New cross-coupled filter design using improved hairpin resonators,” *IEEE Trans. Microwave Theory & Tech.*, vol. 48, no. 12, pp. 2482-2490, Dec. 2000.

[91] Tatsuya Tsujiguchi, Haruo Matsumoto, Toshio Nishikawa, “A miniaturized end-coupled bandpass filter using λ/4 hair-pin couplanar resonators,” *1998 IEEE MTT-S International Microwave Symp. Dig.*, pp. 829-832, 1998.

[92] Wim Diels, Kristof Vaesen, Piet Wambacq, Stéphane Donnay, Walter De Raedt Marc Engels, Ivo Bolsens, “Single-package integration of RF blocks for a 5GHz WLAN application,” *IEEE Trans. Advance Packaging*, vol. 24, no. 3, pp. 384-391, Aug. 2001.

[93] Chang-Ho Lee, Albert Sutono, Sangwoo Han, Kyutae Lim, Stéphane Pinel, Emmanouil M. Tentzeris, Joy Laskar, “A compact LTCC-based Ku-band transmitter module,” *IEEE Trans. Advance Packaging*, vol. 25, no. 3, pp. 374-384, Aug. 2002.

[94] Julien Ryckaert, Steven Brebels, Boris Come, Wim Diels, Dries Hauspie, Serguei Stoukatch, Kristof Vaesen, Walter De Raedt, Stephane Donnay,” Single-package 5 GHz WLAN RF module with embedded patch antenna and 20 dBm power amplifier,” *2003 IEEE MTT-S International Microwave Symp. Dig.*, pp. 1037-1040, 2003.

[95] Yo-Shen Lin, Chien-Chang Liu, Ko-Mai Li, Chun Hsiung Chen, “Design of an LTCC tri-band transceiver module for GPRS mobile applications,” *IEEE Trans. Microwave Theory and Tech.*, vol. 52, no. 12, pp. 2718-2724, Dec. 2004.

[96] Manos M. Tentzeris, Joy Laskar, John Papapolymerou, Stéphane Pinel, V. Palazzari, R. Li, G. Dejean, N. Papageorgiou, D. Thompson, R. Bairavasubramanian, s. Sarkar, J.-H. Lee, “3-D-integrated RF and millimeter-wave functions and modules using liquid crystal polymer (LCP) system-on-package technology, “ *IEEE Trans. Advance Packaging*, vol. 27, no. 2, pp. 332-340, May 2004.

[97] Alexander Chernyakov, Konstantin Markov, Denys Orlenko, Patric Heide, Clemens Ruppel, “Miniature fully-integrated WLAN frontend-modules based on LTCC technology,” *2004 IEEE MTT-S International Microwave Symp. Dig.*, pp. 139-142, 2004.

[98] Fei-Ran Yang, Kuang-Ping Ma, Yongxi Qian, and Tatsuo Itoh,” A novel-low-loss slow-wave microstrip structure,” *IEEE Microwave Guided Wave Letters*, vol. 8, no. 11, pp. 372-374, Nov. 1998.

[99] Fei-Ran Yang, Kuang-Ping Ma, Yongxi Qian, and Tatsuo Itoh,” A uniplanar compact photonic-bandgap structure and its applications for microwave circuits,” *IEEE Trans. Microwave Theory, and Tech.*, vol. 47, no. 8, pp.1509-1514, Aug. 1999.

[100] Yongxi Qian, Vesna Radisic, and Tastsuo Itoh,” Simulation and experiment of photonic band-gap structures for microstrip circuits,” *Asia Pacific Microwave Conference*, pp. 585-588, 1997.

[101] Vesna Radisic, Yongxi Qian, Roberto Coccioli, and Tatsuo Itoh, “Novel 2-D photonic bandpag structure for microstrip lines,” *IEEE Microwave and Guided Wave Letters*, vol. 8, no. 2, pp.69-71, Feb. 1998.

[102] K. P. Ma, K. Hirose, F. R. Yang, Y. Qian, and Tatsuo Itoh, “Realizatoin of magnetic conducting surface using novel photonic bandgap structure,” *Electron. Lett.*, vol. 34, pp. 2041-2042, Nov. 1998.

[103] C. Patrick. Yue, and S. Simon Wong,” Physical modeling of spiral inductors on silicon,” IEEE Trans. Electron Devices, vol. 47, no. 3, pp. 560-568, March 2000.

[104] Sunderarajan S. Mohan, Maria del Mar Hershenson, Stephen P. Boyd, and Thomas H. Lee, “Simple accurate expressions for planar spiral inductances,” *IEEE J. Solid-State Circuits*, vol. 34, no. 10, pp. 1419-1424, Oct. 1999.

[105] Y. C. Shih, C. K. Pao, and T. Itoh, “A broadband parameter extraction technique for

the equivalent circuit of planar inductors," *IEEE MTT-S Symp. Dig.*, pp. 1345-1348, 1992.

[106] H. A. Wheeler, "Formulas for the skin effect," *Proc. IRE*, vol. 30, pp. 412-424, Sep. 1942.

[107] Ali M. Niknejad, Robert G. Meyer, "Analysis of eddy-current losses over conductive substrates with applications to monolithic inductors and transformers," *IEEE Trans. Microwave Theory, and Tech.*, vol. 49, no. 1, pp.166-176, Jan. 2001.

[108] Inder J. Bahl, "High-performance inductors," *IEEE Trans. Microwave Theory, and Tech.*, vol. 49, no. 4, pp.654-664, April 2001.

[109] Ya-Hong Xie, Michel R. Frei, Andrew J. Becker, Clifford A. King, D. Kossives, L. T. Gomez, and S. K. Theiss," An approach for fabricating high-performance inductors on low-resistivity substrates," *IEEE J. Solid-State Circuits*, vol. 33, no. 9, pp. 1433-1438, Sep. 1998.

[110] Han Su Kim, Dawei Zheng, A. J. Becker, and Ta-Hong Xie," Spiral inductors on Si p/p+ substrates with resonant frequency of 20 GHz," *IEEE Electron Device Letters*, vol. 22, no. 6, pp. 275-277, June 2001.

[111] Hongrui Jiang, Ye Wang, Jer-Liang Andrew Yeh, and Norman C. Tien, "On-chip spiral inductors suspended over deep copper-line cavitites," *IEEE Trans. Microwave Theory, and Tech.*, vol. 48, no. 12, pp.2415-2423, Dec. 2000.

[112] C. Patrick Yue, S. Simon Wong, "On-chip spiral inductors with patterned ground shields for Si-based RF IC's," *IEEE J. Solid-State Circuits*, vol. 33, no. 5, pp. 743-752, May 1998.

[113] C. Patrick Yue, and S. Simon Wong, "A study on substrate effects of silicon-based RF passive components." *2004 IEEE MTT-S International Microwave Symp. Dig.*, pp. 1625-1628, 1999.

博士候選人資料

姓　　　名 ： 吳憲順

性　　　別 ： 男

出生年月日 ： 民國 66 年 3 月 20 日

籍　　　貫 ： 江西省萍鄉縣

學　歷 ：

81 年 9 月 至 86 年 6 月 國立台北工專五專部電子科
(現國立台北科技大學)
86 年 9 月 至 88 年 6 月 國立台北科技大學二技部電子系
88 年 9 月 至 90 年 6 月 國立交通大學電信所電波組碩士班

論文題目 ：

合成波導之設計與應用

Design and Applications of Synthetic Waveguides

Publication List

(2002 ~ 2005)

1. Hsien-Hsuen Wu, Ching-Jung Peng, Wen-Chang Lee, Chia-Min Lin, Ho-Chung Chen, Mei-Chien Chen, Shao-Cheng Lin, Tsai-Pi Hung, Cheng-Jung Lee, and Ching-Kuang C. Tzuang, “All-Planar Millimeter-Wave WLAN Transceiver,” *Technical Digest of the TSMMW2002 - 2002 Topical Symposium on Millimeter-Waves*, pp. 61-64, Yokosuka Research Park, Japan, March 14-15 2002.

2. Ching-Kuo Wu, Hsien-Shun Wu and Ching-Kuang C. Tzuang, “Electric-magnetic-electric (EME) Slow-wave Microstrip Line and Bandpass Filter of Compressed Size,” *IEEE Trans. On Microwave Theory and Techniques*, vol.50, no.8, pp.1996-2004, August 2002.

3. Hsien-Shun Wu and Ching-Kuang C. Tzuang, "PBG-enhanced Inductor," *Proc. of the IMS2002 - 2002 IEEE MTT-S International Microwave Symposium (IMS2002),* pp1087-1089, we4c, Seattle, Washington, June 2-7, 2002.

4. Ching-Kuang C. Tzuang and Hsien-Shun Wu, “Properties and Designs of Electromagnetic Guiding and Radiating Devices with Mixed Electric and Magnetic Surfaces,” *Proc. of the PIERS2003 - 2003 Progress in Electromagnetics Research Symposium*, pp. 35, Singapore, Jan. 7~10, 2003.

5. Hsien-Hsuen Wu, Ching-Kuang C. Tzuang, “Miniaturized Synthetic Rectangular Waveguide,” *Proc. of the IMS2003 - 2003 IEEE MTT-S International Microwave Symposium*, pp. 1099~1102, WE2D-1, Philadelphia, Pennsylvania, June 8-13, 2003.

6. Chi-Ho Chang, Hsien-Shun Wu, Houng Jay Yang, and Ching-Kuang C. Tzuang, “Coalesced Single-Input Single-Output Dual-Band Filter,” *Proc. of the IMS2003 - 2003 IEEE MTT-S International Microwave Symposium*, pp. 511~514, Philadelphia, Pennsylvania, June 8-13, 2003.

7. Hsien-Shun Wu and Ching-Kuang C. Tzuang, "TM_{10} Mode Synthesized Rectangular Waveguide,” *Proc. of the APMC2003 - 2003 Asia-Pacific Microwave Conferences*, pp. 533~536,WEP-54, Seoul, Korea, November 4~7, 2003.

8. Hsien-Shun Wu and Ching-Kuang C. Tzuang, “Integrated Millimeter-Wave Rectangular Waveguide Antenna Array,” *Technical Digest of the TSMMW2004 - International Joint*

Conference of the 6th Topical Symposium on Millimeter Waves, pp.102~105, Yokosuka, Japan, February 26~27, 2004.

9. Hsien-Shun Wu, Hsien-Hung Wu, Ching-Kuang C. Tzuang and Ta-Sung Lee, “Transmission-line-based CMOS RF SOC from Microwave to Millimeter-Wave,” *Proc. of the CDC2004 - 2004 Communications Design Conference*, San Francisco, CA, March 29~April 1, 2004.

10. Hsien-Hung Wu, Hsien-Shun Wu and Ching-Kuang C. Tzuang,“Synthesized High-Impedance CMOS Thin-Film Transmission Line,” *The 5th Topical Meeting on Silicon Monolithic Integrated Circuits in RF Systems*, Atlanta, September 8~10 2004.

11. Hsien-Shun Wu and Ching-Kuang C. Tzuang, “Miniaturized High-Gain Synthetic Rectangular Waveguide Antenna of Near-Omnidirectional Radiation Pattern” *Technical Digest of the EuMC2004 - 34th European Microwave Conference*, Amsterdam, Holland, October 11~15, 2004.

12. Hsien-Shun Wu, Raymond H.Yang and Ching-Kuang C. Tzuang, “Synthesis of Quasi-Elliptical Fishbone Bandpass Filter”, *Proc. of the APMC2004 - Asia-Pacific Microwave Conferences*, India, December 15~18, 2004.

13. Hsien-Shun Wu and Ching-Kuang C. Tzuang, “CMOS Integrated Antenna for 60 GHz WPAN Applications” *Proc. of the PIERS 2004 - Progress in Electromagnetics Research Symposium*, Nanjing China, August 28~31, 2004.

14. Sam Kuo, Hsien-Shun Wu and Ching-Kuang C. Tzuang, “A Miniaturized 60GHz GaAs PHEMT Sub-Harmonic Mixer” *Proc. of the PIERS 2004 - Progress in Electromagnetics Research Symposium*, Nanjing China, August 28~31, 2004.

15. Hsien-Shun Wu and Ching-Kuang C. Tzuang, “Artificially Integrated Synthetic Rectangular Waveguide,” to be appeared on the Sept. issue of *IEEE Trans. On Antenna and Propagation* 2005.

16. Hsien-Shun Wu Houng-Jay Yang and Ching-Kuang C. Tzuang, “Miniaturized Microwave Passive Filter Incorporating Multi-layer Synthetic Quasi-TEM Transmsiision Line,” to be appeared on the Sept. issue of *IEEE Trans. On Microwave Theory and Techniques* 2005.

17. 莊晴光,吳憲順, *具有人工磁性金屬層之電感結構*,中華民國專利 第 230382 號.

18. 莊晴光,吳憲順, *使用週期性結構的矩形波導及其設計方法*,中華民國專利 第 231386 號.